CHEMO-MECHANICS OF LI-ION BATTERIES: IN-SITU AND OPERANDO STUDIES

A Dissertation

Submitted to the Faculty

of

Purdue University

by

Luize Scalco de Vasconcelos

In Partial Fulfillment of the

Requirements for the Degree

of

Doctor of Philosophy

December 2020

Purdue University

West Lafayette, Indiana

THE PURDUE UNIVERSITY GRADUATE SCHOOL
STATEMENT OF DISSERTATION APPROVAL

Dr. Kejie Zhao, Chair

School of Mechanical Engineering

Dr. Thomas Siegmund

School of Mechanical Engineering

Dr. Partha P. Mukherjee

School of Mechanical Engineering

Dr. Haiyan Wang

School of Materials Engineering

Approved by:

Eckhard A. Groll

Head of the Departmental Graduate Program

To my family, for their love and encouragement.

ACKNOWLEDGMENTS

I'm grateful to Prof. Kejie Zhao for going above and beyond as a mentor. Prof. Zhao spent countless hours helping me develop the skills to succeed in my professional endeavors. With him, I not only learned how to be a strong researcher but also how to be an effective mentor. He always gave me the freedom to pursue my own ideas and take charge of my research. At the same time, he nudged me in the right direction and gave me the necessary support to accomplish my goals.

I'm also thankful for my committee members, Prof. Partha P. Mukherjee, Prof. Thomas Siegmund, and Prof. Haiyan Wang. Their input helped shape my work to its best form. They have also been supportive of my studies and career.

I also need to thank each student and alumni from Zhao's research group. They have been my daily dose of inspiration and fun. A special thanks to my closest friends and confidants, Dr. Rong Xu, Hong Sun, Xiaokang Wang, Nikhil Sharma, Shan Hu, Sameep Shah, Yue Guo, Jiaxiu Han, and Xianyang Wu. I will carry the memories we made together at Purdue fondly. Among them, failures and successes in the lab, teamwork in difficult courses, and comforting and uplifting conversations in the office. Dr. Rong Xu welcomed me to the group and ever since has been my closest collaborator and a big supporter of my research. We made a great team.

Lastly, I would like to thank my loved ones, Vinicius Nascimento, Daniele Vasconcelos, Mary Scalco, and Amilton Vasconcelos, for their unwavering support.

TABLE OF CONTENTS

Page

LIST OF FIGURES

Figure Page

Figure Page

Figure Page

Figure Page

ABSTRACT

Vasconcelos, Luize S. Ph.D., Purdue University, December 2020. Chemo-mechanics of Li-ion batteries: In-situ and Operando studies. Major Professor: Kejie Zhao, School of Mechanical Engineering.

Electrochemical energy storage devices play an integral role in the energy transition from fossil fuels to renewable. Still, technological breakthroughs are warranted to expand this progress and enable their use where hydrocarbons are still the dominant option. The requirements restricting further adoption of electrochemical devices are related to energy density, hampering costs of raw materials with the increased global demand, and safety in large scale operations. Furthermore, new applications in flexible electronics add new requisites to this list. Pushing these limits involves multidisciplinary efforts where the mechanics are a crucial part.

This thesis explores the mechanical and kinetic behaviors of batteries at the nano to micro-meter scale through operando mechanical and optical characterization during ongoing electrochemical reactions. A unique experimental platform that enables simultaneous nanoindentation and electrochemical testing of active materials is developed. The validity of mechanical testing during operation in the customized liquid cell is systematically addressed. The evolution of the mechanical properties of electrodes as a function of lithium concentration is probed in real-time. This functional dependence between mechanical properties and composition is then used to introduce the concept of mechanics-informed chemical profiling. This new capability enables characterizing transport kinetics in a detailed and quantitative way, including the role of pressure gradients on diffusion. Pairing these experiments with multi-physics modeling led to a new understanding of the mechanisms regulating charging-rate capability and capacity loss in Li-ion batteries. Experiments on composite electrodes showed that liquid electrolytes change the mechanical properties of both conductive

matrix and secondary particles. These observations help understand the interactions between the different components of a battery and demonstrate the need for in-situ mechanical characterization capabilities.

1. INTRODUCTION

1.1 Background and significance

The widespread adoption of electric transportation and the integration of renewable energy are crucial steps towards the reduction of the earth's carbon dioxide emissions. According to World Bank Sustainable Energy for All database, only 18% of the total electricity production worldwide originated from renewable sources in 2015 (11% in the United States). Part of the transition towards clean energy depends on lowering the cost and increasing the power and energy densities of energy storage, including electrochemical devices.

The electrochemical reactions between the host material and guest species induce deformation and mechanical stress. Figure 1.1 (a) illustrates an example of diffusion-regulated stress fields upon Li insertion in batteries. Likewise, mechanical stresses regulate mass transport, charge transfer, interfacial reactions, and consequently the potential and capacity of electrochemical systems [183]. Figure 1.1 (b) illustrates this reverse effect of stress-regulated diffusion where a hydrostatic stress gradient drives Li flux. Moreover, new theories suggest that the flow stress at chemical equilibrium may differ from that under chemical loads [68, 14]. Figure 1.2 illustrates the fundamental coupling between mechanics and chemistry in red.

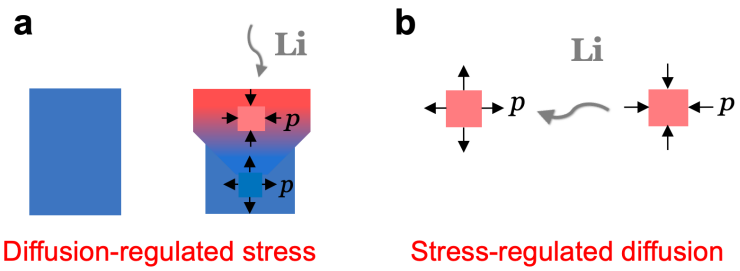

Figure 1.1. : Illustration of the two way coupling between stress and diffusion. (a) The volumetric change inherent from the Li insertion paired with slow Li diffusion leads to mismatched strain and stresses. (b) Stress gradients induce Li flux.

In Li-ion batteries, mechanical degradation from the chemical reactions leads to loss of performance over cycles of commercial systems [118, 115], and it limits the implementation of new, higher energy density materials [111]. In solid oxide fuel cells, cracks occur due to the thermal stresses and non-stoichiometry of oxygen in the electrodes and electrolyte [1, 143]. In capacitors using ferroelectric thin films, the mismatch strain caused by the electric polarization leads to the presence of a disruptive dead layer at the metal-dielectric interface and a capacitance drop [139, 107]. In photovoltaics, the low resistance to cohesive fracture of perovskite films inhibits the success of perovskite solar cells as a viable technology [131]. In hydrogen storage, the interplay between hydrogen and localized plasticity of the fuel containers causes embrittlement [91]. Thus, knowledge about the mechanical behavior upon electrochemical reactions is crucial in understanding degradation mechanisms in these systems and enables the design of materials of enhanced mechanical reliability. Figure 1.2 illustrates this higher level causal relationship between structural stability and electrochemical performance.

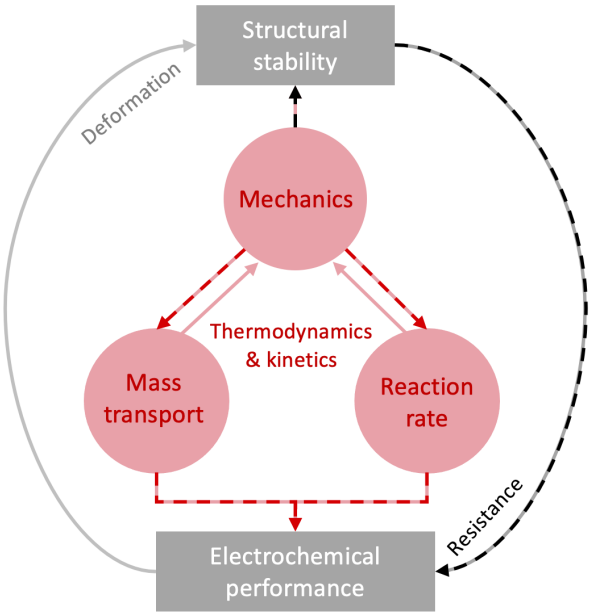

Figure 1.2. : Interplay between mechanics and electrochemistry from the fundamental to the application level.

Despite the considerable volume of existing studies in this field, the intimate coupling between mechanics and electrochemistry is far from complete understanding. A major reason is the lack of experimental and methods for probing the dynamics of the interplay between mechanical behaviors and chemical reactions in real-time. The operation of batteries is extremely sensitive to the work environment - a trace of oxygen and moisture can cause numerous side reactions. In contrast, most mechanical test equipment is an open system with limited capability of environment control. As such, the mechanics and electrochemistry of batteries are often characterized separately. Advances in characterization capabilities and their application to exploring material behaviors upon reactions will promote a deeper understanding of the underlying multiphysics.

The goal of this dissertation is to expand the current understanding of the interplay between mechanics and electrochemistry in energy devices. It focuses on Li-ion

batteries; however, the theoretical framework and experimental tools developed here are well applicable to other electrochemical systems.

1.2 Thesis outline

The outline of this thesis is summarized below:

Chapter 2 presents a new experimental platform for operando nanoindentation that enables probing the mechanical behaviors of electrodes during real-time electrochemical reactions. The setup consists of a nanoindenter, an electrochemical station, and a custom fluid cell integrated into an inert environment. The work included the evaluation of the influence of the argon atmosphere, electrolyte solution, structural degradation, and volumetric change of electrodes upon Li reactions, as well as the surface layer and substrate effects by control experiments. Results inform on the system's limitations and capabilities, besides providing guidelines on the best experimental practices. Furthermore, it presents a thorough investigation of the elastic-viscoplastic properties of amorphous Si electrodes, during cell operation at different C-rates and open-circuited. This new tool provides a reliable platform to understand the fundamental coupling between mechanics and electrochemistry in energy materials.

Chapter 3 sets forth a nanoindentation approach to probe the spatiotemporal Li profile using the functional dependence of the mechanical properties on Li concentration. These mechanics-informed material dynamics allows the measurement of the composition-dependent diffusivity, evaluation of the rate-limiting processes, and assessment of the stress regulation on Li transport. The experiments show that Li diffusivity in amorphous Si varies exponentially by three orders of magnitude from the pristine to the fully lithiated state. Lithiation in amorphous Si is limited by diffusion at the micron scale. The numerical simulations showed that the composition dependence of the Li diffusivity creates an asymmetry on the rate capability during lithiation versus delithiation. In Si, the aforementioned exponential diffusivity lithi-

ation dependency results in a fast lithiation that proceeds via a steep concentration gradient compared to a slow and relatively smooth delithiation. This asymmetric behavior appears to be the root cause of Li trapping and loss of the deliverable capacity in Si.

Chapter 4 presents in-situ nanoindentation measurements of the mechanical behavior of individual phases of an NMC composite electrode. It focuses on the understanding of the mechanical properties of the constituents in dry and wet (in the electrolyte) conditions. The influence of electrolyte soaking on the elastic modulus, hardness, and volume change of the conductive matrix with different degrees of porosity is quantified. The elastic modulus, hardness, and fracture strength of the agglomerated active particles and sintered pellets are compared in the dry against the liquid environment. The electrolyte enhances the fracture strength of the particle agglomerate, which may be caused by the additional capillary force between primary particles.

Chapter 5 presents an operando optical microscopy study of the Li compositional spatiodynamics of NMC electrodes. The experiments reveal a new kinetic behavior of NMC electrodes. The first delithiation of pristine NMC happens through localized, sudden changes in concentration and propagates as a wavefront through the connected regions of the active particles. Individual particles are "activated" seemingly randomly and asynchronously throughout the electrode. The following (dis)charge sequences, at the same C-rate, proceed through a gradual and simultaneous (de)lithiation of all viable particles. This appears to be the first report of such behavior to date. Our tests show that this effect is not conditional on the composition of the electrolyte, the matrix, or the transition metal ratio. This unusual kinetic behavior persists regardless. This chapter discusses possible mechanisms behind this phenomenon. A better understanding of this particle activation phenomenon could have implications on the design of the ideal formation protocol, and have consequences on long-term performance.

2. OPERANDO NANOINDENTATION OF ELECTRODES UNDERGOING ELECTROCHEMICAL REACTIONS

This chapter is adapted from [34].

2.1 Introduction

Existing experimental tools have been able to provide valuable insight on the mechanical behaviors of electrode materials. Due to the generally small characteristic size and heterogeneous feature of electrodes, large-scale mechanical tests find limited applications in energy materials. The wafer-curvature method is a convenient and reliable tool to measure the stress evolution in thin-film electrodes during electrochemical cycles. This technique has been used to monitor the stress development in Ge [113], Si [120], metal oxides [70, 125], and composite thin films [80] at a specific states-of-charge. Nevertheless, it is not convenient to map the continuous evolution of mechanical properties (elastic modulus, hardness, viscous property) of electrodes upon Li reactions, or to probe the local variations in a composite configuration by wafer-curvature measurements. Another method to determine the mechanical properties in a controlled environment is tensile tests of nanowires. Kushima et al., for instance, performed delicate tensile experiments of fully lithiated Si nanowires inside a transmission electron microscope (TEM). In this test, an atomic force microscopy (AFM) cantilever connected to a Li rod was used to conduct lithiation and subsequently apply tension to the nanowire [73]. While the TEM experiment can provide desirable information such as fracture strength and Young's modulus of nanowires, the electrochemical conditions are not well controlled, which results in divergent results in literature [9].

Ex-situ nanoindentation and AFM experiments have been employed in the characterization of battery materials, owing to the simplicity of the test, the resolution being suitable to the size of the electrode constituents, and the ability to access a range of material behaviors [56, 33, 126, 180]. In-situ AFM is an effective technique to examine the solid electrolyte interface (SEI) layer and the morphological evolution of electrodes during electrochemical cycles [29]. One study tracked the volumetric expansion and the thickness of SEI of Si thin-film electrodes, and explained the capacity hysteresis due to the coupling between the electrochemical potential and mechanical stresses [177]. Another study used in-situ AFM to investigate the distribution of elastic modulus of the SEI across the sample surface; close inspection of the load-displacement curves indicated that the SEI structure is highly heterogeneous, composed of a combination of multiple layers, hard particles, and bubbles [187]. Application of in-situ AFM to study the mechanics of electrode materials is, nonetheless, scarce. One report characterized Si nanopillars in an electrochemical cell in a dry room [99]. Although results provide qualitative information on the influence of lithiation on the mechanical properties, the data exhibited excessive noise which makes the data interpretation elusive. Thus, while AFM is an outstanding tool for probing the morphology of relatively soft materials, nanoindentation is better suited for studying the mechanical response of active materials in batteries, which are in general of high mechanical strength.

Nanoindentation is a well-established technique to probe a variety of mechanical properties of materials. It is an ideal system for in situ characterization of electrode materials because it does not require a specific sample geometry or a large volume of material. These advantages come at a cost of it requiring meticulous control of the stability of the surrounding environment, high surface quality of the sample and a well defined tip-material contact. Satisfying these requirements is even more difficult in the context of a functioning cell undergoing electrochemical reactions, where problems such as lithiation induced volume change of the sample, enhanced substrate effect, structural degradation, and the interference of SEI must be addressed.

This chapter introduces indentation tests performed on an operating fluid cell in inert atmosphere. The experimental setup combines a nanoindenter, a home-developed cell, and an electrochemical station into an argon-filled glovebox. The first part of the work, Sections 2.2 and 2.4, discusses limitations and capabilities of the system, and provide guidelines on the best experimental practices. The second part, Section 2.5, presents measurements of the dynamic evolution of the elastic modulus, hardness, and creep stress exponent of lithiated Si as a continuous function of Li concentration under open circuit and at various charging rates. In addition, the inert atmosphere is used to probe the mechanical properties of pure lithium metal, which would rapidly form a lithium hydroxide coating if exposed to air. The hardness at different C-rates and the creep exponent relate to the research questions RQ1 and RQ2, respectively. Lastly, major contributions and open questions are summarized in Section 2.6.

2.2 Experimental methods

The experimental platform integrates a Keysight G200 nanoindenter equipped with continuous stiffness measurement (CSM), a Princeton VersaSTAT3 electrochemical station, and a home-developed fluid cell into an argon-filled glovebox (O_2 and H_20 < 1 ppm), Figure 2.1. The fluid cell is made of Teflon, which is chemically inert to the liquid electrolyte. The height of the fluid cell is carefully designed in order to maintain sufficient liquid electrolyte to fully cover the electrodes, and also to avoid the interference with the motion of the indenter tip, allowing the stage to travel freely from the indenter to the microscope for surface inspection. The sample under investigation is fixed to the center of the fluid cell and serves as the working electrode (WE), while Li metal ribbons are used as the reference (RE) and counter (CE) electrodes fitting inside the slots surrounding the cell. The selected electrolyte, 1M $LiPF_6$ in propylene carbonate (PC) is nonvolatile, enabling a constant fluid level and salt concentration

during long tests; preliminary tests using relatively volatile solvent diethyl carbonate (DEC) show more noise and variation in the experimental results.

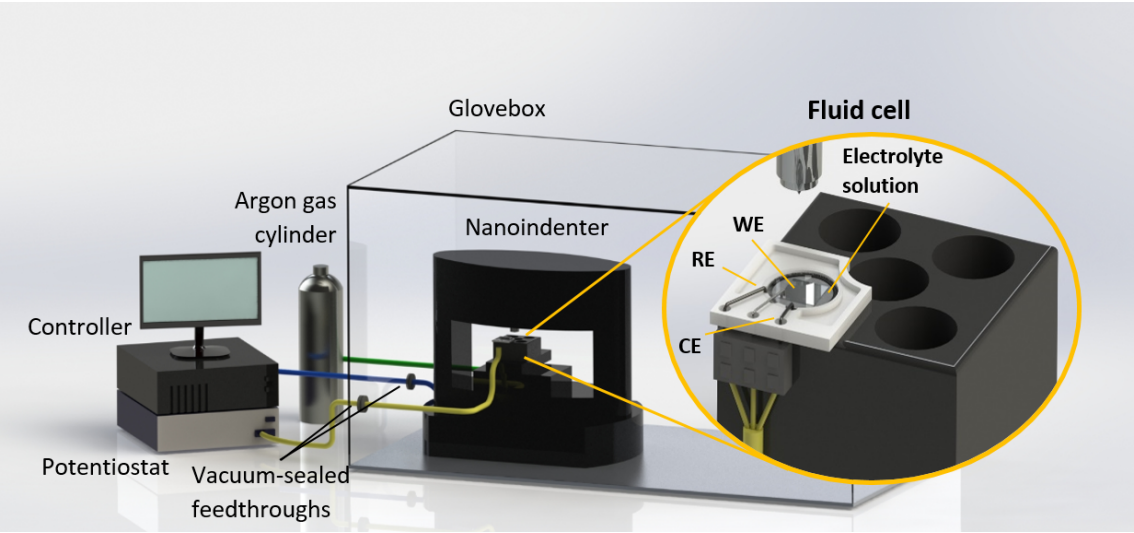

Figure 2.1. : The experimental platform of operando indentation including a nanoindenter residing in an argon-filled glovebox, a home-developed liquid cell, and an electrochemical station. The dynamic evolution of the mechanical properties of the working electrode (WE) is probed by nanoindentation during real-time electrochemical reactions.

2.3 Control experiments

Control experiments are performed to validate the custom work condition of in situ nanoindentation. Figure 2.2 shows the comparisons of the elastic modulus of fused silica and amorphous silicon measured in the air versus argon environment, in the standard holder versus the dry fluid cell, and on dry material versus wet sample submerged in the electrolyte-filled fluid cell. The different measurements show close values in the different configurations. This consistency confirms that effects of the dielectric constant of Ar on the capacitance gauge of nanoindentation, the non-standard sample holder, and the buoyancy and surface tension of the liquid electrolyte on the indenter column are negligible. For best practice, the glovebox should be solely

dedicated to the indentation experiments during tests since gas flow in the enclosure will lead to noisy data.

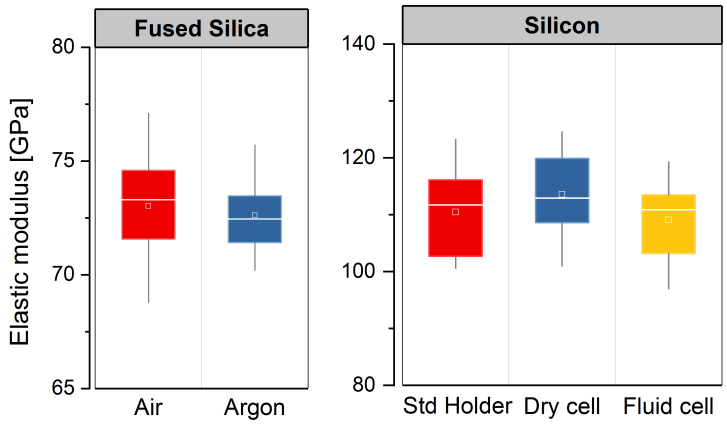

Figure 2.2. : Control experiments performed on fused silica and Si thin film show that the measurements are not affected by the argon atmosphere, customized holder (dry cell) or the liquid electrolyte environment (fluid cell).

2.3.1 Sample preparation

Both amorphous Si and Li metal are the samples to be characterized in this study. High-purity Li metal ribbons (99.9%, 0.75 mm thick, Sigma-Aldrich) are used, whereas a-Si thin films are prepared using the Leybold E-beam Evaporator. The fabrication starts with the deposition of a 50 nm Ti thin film onto a 1 mm thick silica substrate, followed by the deposition of a 300 nm copper film, both at a rate of 0.5 Å/s. The Cu film serves as the current collector, and the Ti underlayer is used to improve the adhesion between the Cu film and the glass substrate. Finally, a 500 nm Si film is deposited at the same rate of 0.5 Å/s. In addition, a second silicon film, 1.4 μm thick, is fabricated for the evaluation of the substrate effect in indentation measurements. The fabrication followed the same procedure, except that the deposition rate of the thick Si film is 1.5 Å/s . The amorphous structure has been

verified in many previous studies for e-beam evaporation of Si films under similar conditions [104, 72].

2.3.2 Operando nanoindentation

Nanoindentation is performed on a silicon electrode undergoing electrochemical reactions. Tests are conducted uninterruptedly with a grid spacing of 40 μm between indents. Separately, ex-situ measurements (33 indents) are performed on Li metal ribbons on a standard holder. The CSM method is used for hardness and elastic modulus measurements (2 nm harmonic displacement, 45 Hz frequency). Tests followed a typical chronology: Indenter approaches material until surface is detected (detection criteria: contact stiffness $S > 200$ N/m), loads at a constant strain rate ($0.05\ s^{-1}$), holds at the maximum load for a dwell time (10 s), partially withdraws and holds the constant load for a second dwell time (60 s) to measure the drift-rate, and finally completely withdraws from the sample. The hardness H and elastic modulus E are given by:

$$H = \frac{P}{A_c} \tag{2.1}$$

and

$$\frac{1}{E_r} = \frac{1 - v^2}{E} + \frac{1 - v_i^2}{E_i} \tag{2.2}$$

where P is the load, ν and ν_i are the Poisson ratio of the sample and the indenter, respectively, E_i is the elastic modulus of the indenter, and $E_r = 0.5S\sqrt{\pi/A_c}$. The Poisson ratios of 0.22 and 0.3 are specified for Si and Li, respectively [8]. The area of contact A_c as a function of indentation depth is calibrated empirically in order to account for the deviation from the ideal indenter geometry (bluntness of the tip) at small indentation depths [52]. It has the form:

$$A_c = C_0 h_c^2 + \sum_{i=1}^{n} C_i h_c^{1/(2i)}. \tag{2.3}$$

The coefficients are determined for $n = 4$ from indentation measurements on a standard fused silica sample of known modulus. The contact depth h_c is calculated from

the absolute tip displacement h, where $h_c = h - 0.75P/S$ [117]. In quasi-static indentation tests, the stiffness S is given by the slope of the load-displacement curve during tip removal, while in the continuous stiffness measurement (also known as dynamic instrumented indentation), the stiffness is derived from the in-phase material response to the superimposed oscillating signal [85].

The constant-load hold method (CLH) is used for creep measurements, for which both the dynamic (CSM) and quasi-static (QS) instrumented nanoindentation are employed [140]. The QS test is preferred over CSM for tests of relatively short hold period to avoid the additional noise from CSM [8]. CSM experiments are conducted for a relatively longer hold period; the results are used to cross-validate the output of the QS measurements. For both tests, the tip is loaded until the maximum indentation depth is reached (100 nm for Si electrode and 3 μm for Li metal), the load is maintained constant for a period of hold time while the tip displacement is measured. Figures 2.3(a) and (b) summarize the procedure used for the determination of the creep stress exponent. The tip displacement measured during the peak load is fitted with a Belehradek function [8], Figure 2.3(a). The data from QS measurements is fitted up to 20 s for Si thin film and 300 s for Li metal, where the creep rate is larger compared to the typical thermal drifts. The time derivative of the fitted curve, $\dot{h}$, divided by the tip displacement h, gives the indentation strain rate, $\dot{\varepsilon} = \dot{h}/h$ [93]. The stress exponent n in the creep power-law is obtained by the slope of the logarithmic plot of hardness, H, versus the indentation strain rate $\dot{\varepsilon}$:

$$\dot{\varepsilon}_i = C_1 H^n. \tag{2.4}$$

An example of the fitting is shown on Figure 2.3(b) for pristine, partially lithiated and fully lithiated Si. This relationship is analogous to the dependence of strain rate $\dot{\varepsilon}$ on the flow stress σ in uniaxial creep tests ($\dot{\varepsilon} = C_2\sigma^N$), where C_1 and C_2 are both constants and N is the stress exponent. Despite the large difference in the test methodology, it has been shown that, under steady state conditions (hardness is constant for a constant strain rate), the exponents N and n are close for the same materials [140, 93, 145, 96]. Note that Equation 2.4 requires the hardness to be

measured throughout the hold period. This is not practical in QS nanoindentation because the unloading stiffness is undetermined during the hold period. Prior research has shown that the nominal pressure p_{nom}, which is determined directly from the total indentation depth h, $p_{nom} \approx P/24.5h^2$, can be used to estimate the stress exponent [140, 12]; once the elastic transient deformation dissipates, the hardness is a linear function of the nominal pressure, $H = C_3 p_{nom}$, where C_3 is a constant. This relationship yields the strain rate: $\dot{\varepsilon}_i = C_1 C_3 p_{nom}^n$. After a long hold time, however, the creep rate is comparable to the thermal drift and any fluctuation in the thermal drift rate invalidates the thermal drift correction of indentation depth. The CSM method offers the advantage of the continuous measurement of the stiffness, which allows the area of contact during the hold time to be extracted from the Sneddon's equation: $A_c = (S\sqrt{\pi}/2E_r)^2$. Once the contact area is obtained, the hardness can be computed ($H = P/A_c$). The tip contact displacement h_c is numerically solved from the area function to determine the strain-rate $\dot{h_c}/h_c$. Here the nominal contact pressure is employed in QS tests for the creep characterizations and the CSM system along with the Maier method [97] is used in longer hold-period tests to cross-validate the results. The holding times of 300 s and 600 s are set for partially lithiated Si and Li metal, respectively. The stress exponents obtained using the CSM with long hold periods are close to those of QS measurements with short hold periods as presented later in the Section 2.5.

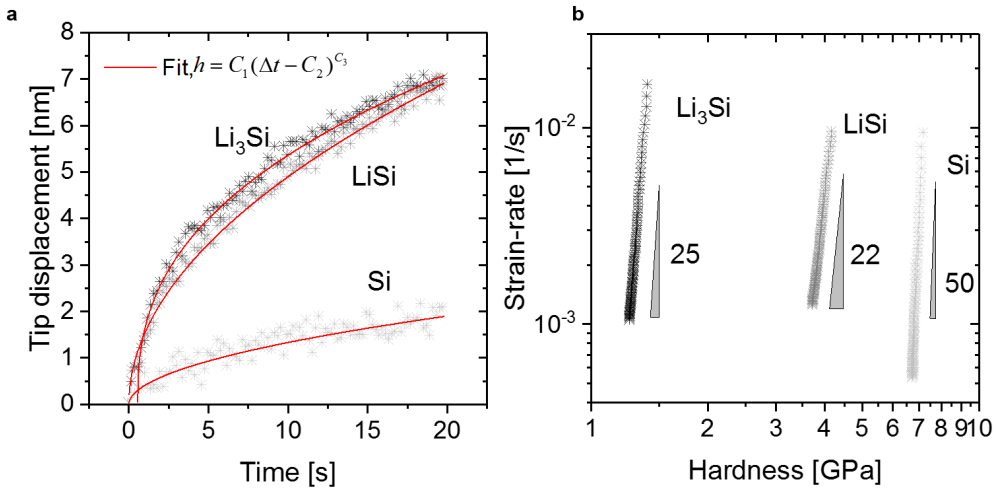

Figure 2.3. : (a) The evolution of indentation depth during the hold period at peak load. (b) The stress exponents of lithiated Si obtained from the slope of the stress vs strain rate responses.

Galvanostatic lithiation is employed for operando indentation. Continuous measurements of elastic modulus, hardness, and creep stress-exponents are performed during the first galvanostatic discharge (cut-off voltage of 0.01 V vs Li/Li+) of Si. Elastic modulus and hardness are measured at intermediate lithiation rates (C/10.6 and C/2.9) while creep stress-exponent experiments are conducted at slow discharge rates (C/30 and C/20). Titration experiments in which the galvanostatic discharge and open circuit are alternated are also performed. In addition, electrochemical cycling is employed to evaluate the relation between the drift-rate and the applied current at high C-rates (C/1.5 and C/3.3). Li concentration is calculated from the state of charge of lithiated Si (assuming a lithiation capacity of 3579 mAh/g for Si). This estimation assumes a homogeneous distribution of Li throughout the sample. Note that the local Li concentration near the indenter tip may deviate from the nominal concentration as the stress field may alter the chemical potential of Li. The inhomogeneity of Li distribution near the tip depends on the Li diffusion rate, the indentation time, and creep properties of lithiated silicon.

2.4 Challenges of operando measurements

2.4.1 Structural degradation of electrodes

In instrumented nanoindentation, the area of contact is derived from the displacement of the tip into the surface as opposed to directly imaging the residual impression. The accuracy of the result depends on the sample surface being approximately flat and continuous. For instance, indenting on top of a discontinuity such as a crack would lead to uninterpretable results. Since Si is known to undergo significant volumetric expansion and structural degradation during lithiation reactions, the integrity of the surface is monitored via optical microscope before and after tests. Figure 2.4 shows the representative optical images of the surface of the Si film during the first electrochemical cycle. During Li insertion, the in-plane expansion of Si thin film is constrained by the substrate, leading to high compressive stresses which suppress crack nucleation and growth, Figures 2.4(a), (b) and (c). Pre-existing local imperfections are amplified during lithiation. However, most of the regimes are maintained in good conditions, allowing grid indentation to be performed over a large area. A small percentage of compromised tests (<4% of all tests) falling nearby the local imperfections are easily identifiable and are removed from the results. Delithiation starts once the voltage cut-off for lithiation is reached. During Li extraction, Si shrinks and the stresses switch the sign from compressive to tensile which drive cracks formation and propagation, Figure 2.4(d). It is observed that the first set of cracks generally develop between 25-65% of delithiation and grow and widen as delithiation proceeds, Figure 3e. Most damages occur at the final 15% of delithiation, resulting in massive delamination of the thin film from the substrate (appears as dark regions in optical images due to light deflection) and/or extensive formation of micron-sized islands. In this work, we limit the mechanical measurements to the first lithiation to avoid excessive cracking and SEI growth. For the interest of investigating mechanical behaviors of Si in the course of charge and discharge cycles, the structural integrity of the sample could be preserved by providing relatively narrow electrochemical windows.

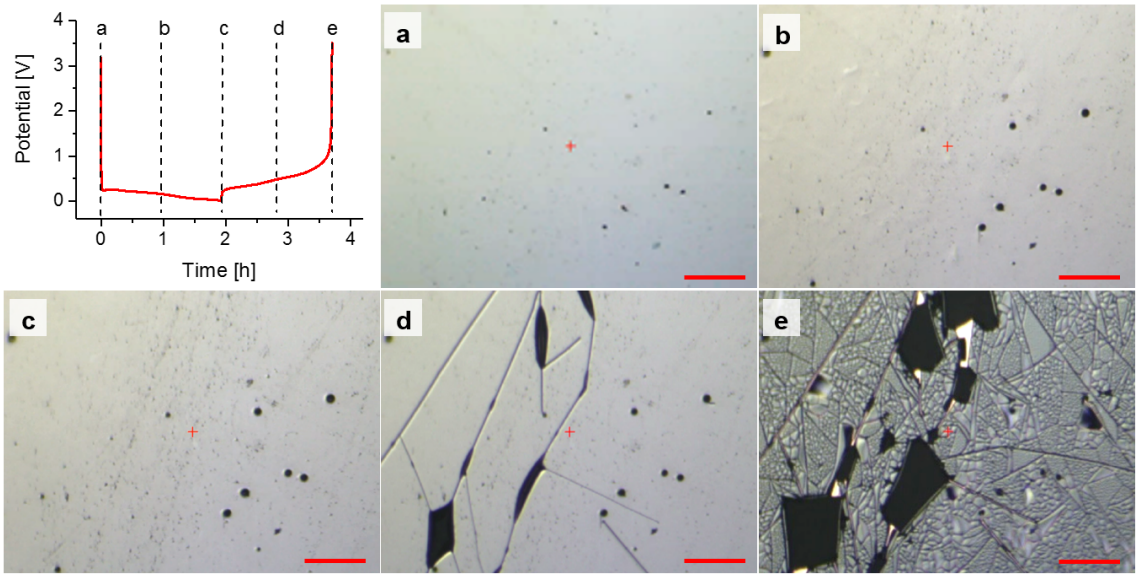

Figure 2.4. : Optical images of the surface condition of a silicon thin film electrode during the first cycle at the charging rate C/2 (scale bars correspond to 100 μm). During lithiation (a, b, c), there is no evidence of mechanical failure and the surface is adequate for indentation tests. During delithiation (d, e), the thin film is cracked and delaminated.

2.4.2 Volume expansion of electrodes during indentation

During Li insertion, the Si thin expands which may compromise the accuracy of the contact depth measurement for operando indentation. The indenter displacement into the surface of the sample is determined by subtracting the tip displacement before contact from its entire moving distance. If the sample changes in size during the test, the estimated contact depth, and consequently the area of contact, is inaccurate. Thus, it is necessary to evaluate (1) the drift caused by the volumetric change of electrodes during Li reactions, herein called electrochemical drift as an analogy to the thermal drift, and (2) the effectiveness of the conventional thermal drift correction to treat the electrochemical drift.

First the electrochemical drift is estimated for different charging rates. For the sake of estimation, let's assume $h_c \approx h$ and $A_c \approx 24.5h^2$, therefore,

$$H^{Error} = \frac{H_M - H_T}{H_T} = \frac{\frac{P}{A_M} - \frac{P}{A_T}}{\frac{P}{A_T}} \approx \frac{\frac{1}{h_M^2} - \frac{1}{h_T^2}}{\frac{1}{h_T^2}}. \tag{2.5}$$

The subscripts "M" and "T" stand for the measured and true values, respectively. The relationship between the measured and the true indentation depth - illustrated on the inset of Figure 2.5(a) - is $h_T = h_M + \dot{d}\Delta t$, where h is the indentation depth, $\dot{d}$ is the rate of change of the sample thickness, and Δt is the elapsed time from the time that the tip contacts the sample surface. Simplifying Equation 2.5 and putting it in terms of measured tip displacement h_M, the error in the hardness H due to the volume expansion of Si is:

$$H^{Error} \approx \frac{h_M - \dot{d}\Delta t^{\,2}}{h_M} - 1. \tag{2.6}$$

Similarly, the error in the elastic modulus E can also be estimated:

$$E^{Error} \approx \frac{h_M - \dot{d}\Delta t}{h_M} - 1. \tag{2.7}$$

The relationship between the volume expansion of Si and the degree of lithiation is approximately linear [177]. Assuming the film only expands out-of-plane, the present thickness d is given by $d = d_o(1 + \alpha z)$, where d_o is the initial thickness and z defines the state of charge with 0 representing the pristine Si and 1 being the fully lithiated state. Yoon et. al measured this relationship for a-Si film in the $LiPF_6$-PC electrolyte and found the expansion coefficient of $\alpha = 2.81$ [177]. For galvanostatic charging, the state of charge is given by $z = \frac{i}{Q}t$, where i is current, Q is the charge capacity of the Si electrode, and t is the charging time. Taking the time derivative of the film thickness d, it gives the rate-of-change in film thickness with respect to the charging rate:

$$\dot{d} = \alpha\, d_0 \frac{i}{Q}. \tag{2.8}$$

As i/Q dictates the charging rate, the combination of Equations 2.6, 2.7 and 2.8 offers an estimate of the error in indentation introduced by sample expansion/shrinkage as a function of the charging rate. Figure 2.5(a) shows the estimated error in hardness and elastic modulus for d_0=500 nm, Δt=70 s, and h_M=100 nm, which are typical values in the nanoindentation experiments. The results show that the error can be expressive if the electrochemical drift is not corrected, especially for the measurements of the charging rate over C/4. For intercalation-type electrodes, the volumetric expansion is small and has negligible effects on hardness and modulus measurements. However, for the insertion- and conversion-type high capacity electrodes such as Si, the electrochemical drift, in particular during fast charging, is significant. Thus, it is necessary to establish a procedure to account for the electrochemical drift in order to investigate the mechanical behaviors of materials at non-equilibrium chemical states.

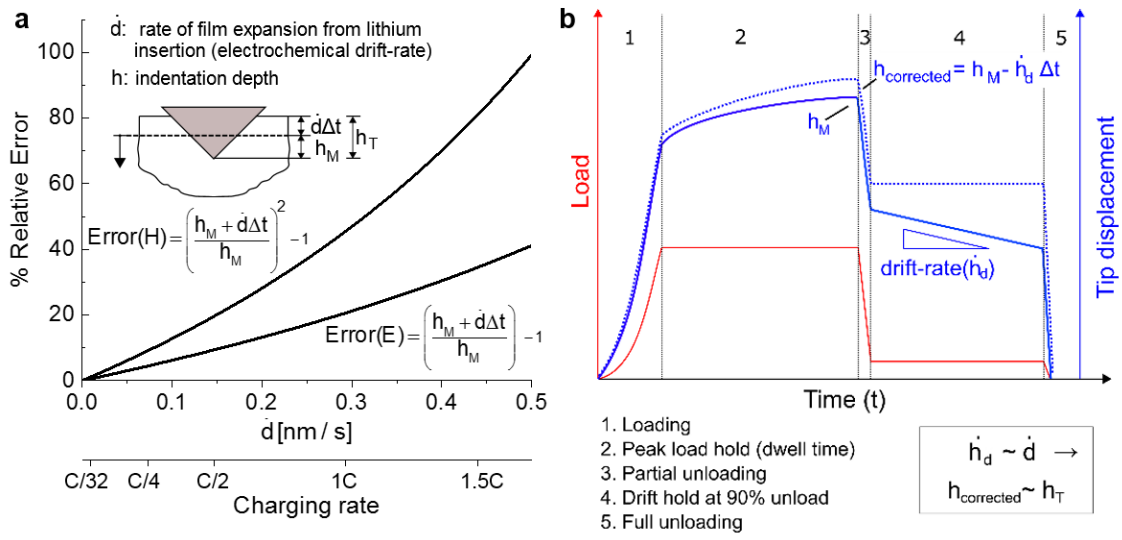

Figure 2.5. : (a) The relative errors in the elastic modulus and hardness induced by the volumetric change of Si during operando indentation. (b) The correction of the electrochemical drift in analogy to the thermal drift. Control experiments are performed to minimize the effects of the environment such as vibration and temperature fluctuation. Sufficient dwell time is allowed for the material to creep to a negligible rate before unloading. The measured drift is attributed to the volumetric change of the thin film electrode during electrochemical reactions.

Thermal drift correction is a conventional method to correct for the tip displacement when the sample is undergoing thermal expansion during indentation [52]. For example, in high-temperature measurements, the temperature difference between the tip and the sample may lead the material around the tip to expand or shrink [159]. The schematic in Figure 2.5(b) illustrates the correction procedure (the drift-rate is exaggerated in the illustration). During the thermal drift period, step 4 in a typical test chronology, the load (red line) is maintained constant while the tip displacement (continuous blue line) is measured. The rate of change in tip displacement with time gives the thermal drift-rate, $\dot{h}_d$. This value, multiplied by the elapsed time, is subtracted from the indentation depth h_M which gives the corrected tip displacement

$h_{corrected}$ (dotted blue line). Notice that the correction is only effective if the drift is approximately linear during the entire time of the test. A negative drift in the tip displacement (negative slope in step 4) means that the tip is withdrawing from the sample, that is, the sample is expanding towards the tip making the tip retreat in order to maintain the contact area constant and thus the constant load. Likewise, a positive drift (positive slope in the tip displacement) indicates that the sample is shrinking. The drift can be attributed to the electrochemical expansion upon Li insertion or extraction if the residual creep, thermal fluctuations, and the change of mechanical properties of the sample during the indentation test are negligible. Here we investigate the electrochemical drift by designing the experiments of minimized environmental fluctuations (long stabilization time, no air flow, vibration isolation, and temperature controlled environment) and sufficient dwell time. In this case, the measured drift-rate $\dot{h}_d$ is mostly attributed to the electrochemical drift-rate $\dot{d}$ by Li insertion, Figure 2.5(b).

Figures 2.6(a) and 2.6 show the drift rates of Si (red dotted lines) during the titration experiments (blue solid lines) under a relatively slow cycle (C/3.3) and a relatively fast charging case (C/1.5), respectively. Results show that the drift-rate (volume change) is approximately zero under the open circuit condition when zero current is provided, negative for a negative current (lithiation), and positive for a positive current (delithiation). It is also noteworthy that at the moment immediately after that the current is applied, an electrochemical shock of excessive tip motion is persistent. The electrochemical drift gradually reaches steady values following the initial "shock". The effect is not well understood at this writing, possibly due to the drastic structural rearrangements of the host material upon the application of the current. For this section's purpose, the indentations performed coincidentally at time of the transition between open circuit and constant current (i.e. during the electrochemical shock) are discarded from the analysis. Figure 2.6(c) depicts the average electrochemical drift rate $\dot{h}_d$ (red dots) (excluding the peaks resulted from the electrochemical shocks) as a function of the C-rate. The experimental output is in good

agreement with the theoretical prediction of d in Equation 2.8. The electrochemical drift rate is on the same magnitude of the typical thermal drift in high-temperature tests ($\sim$ 0.2 nm/s) [159] that the thermal drift correction can be an effective way to account for the volumetric change of electrodes during electrochemical reactions. Although the electrochemical drift and the thermal drift can be separately measured as shown in Figures 2.6 (a) and (b), it is not necessary to separate these two origins of drift and the standard correction procedure outlined in Figure 2.5 is sufficient to account for both effects.

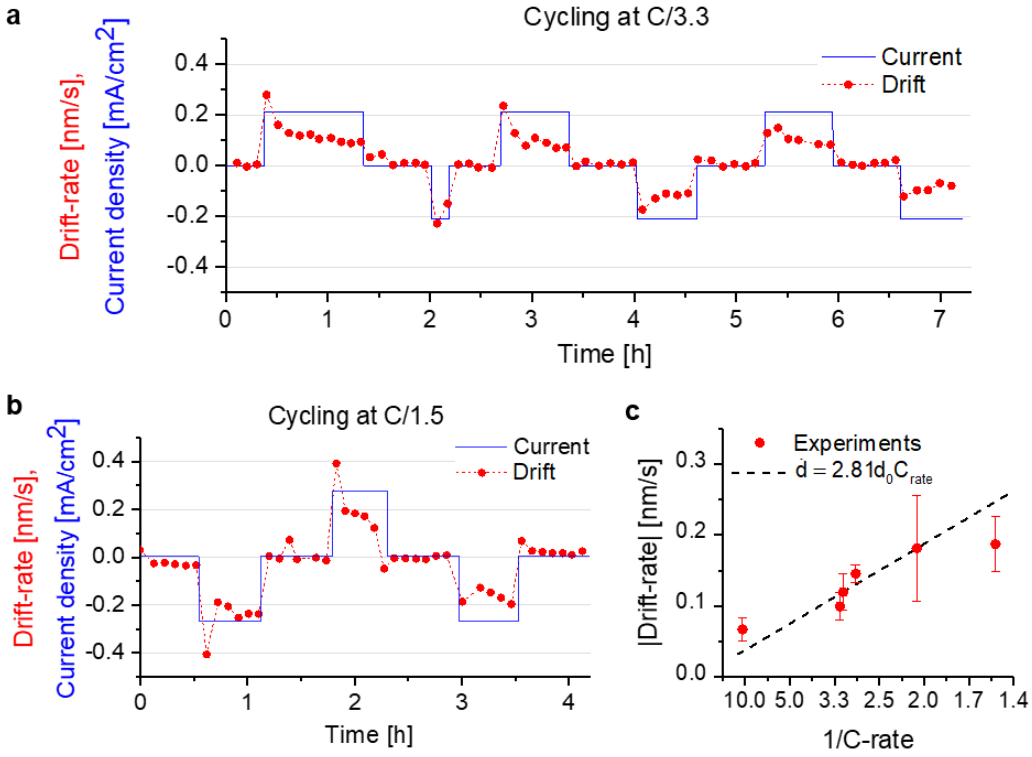

Figure 2.6. : (a) Electrochemical drift (red dots) measured during titration galvanostatic (de)lithiation (blue lines). (a) Cyclic test at C/3.3 charging rate, (b) cyclic test at C/1.5, and (c) the comparison of the drift rates with the theoretical prediction.

2.4.3 Interference of surface layer and substrate effect

One of the challenges of operando measurements is the presence of the SEI layer on top of the Si sample. For this reason, it is necessary to investigate the possibility of the SEI layer interfering with measurements. The substrate effect is not a particular problem of operando indentation, nevertheless, it is a common issue in the characterization of thin films and its assessment is important for the interpretation of the results. For deep enough indentations in thin films, the probed mechanical properties correspond to the mixed response of substrate and sample. The same can be said for a sample with a thin coating, for example. For this reason, the continuous stiffness measurement, which measures the elastic modulus and hardness continuously as a function of the indentation depth, is helpful in identifying effects of SEI (a surface layer) and the substrate (copper, titanium and fused silica).

First, let's consider what would be the effect of the SEI layer. In indentation tests, the criteria for the identification of the surface is a sudden increase in load with the tip displacement, more precisely, once the continuously measured stiffness exceeds 200 N/m. The SEI is considerably more compliant than the lithiated Si. In this scenario, if the SEI layer is sufficiently soft and thin such that the surface identification criteria is not satisfied before the indenter reaches the surface of the lithiated Si, the indentation results should be unaffected. The thickness of the SEI of Si, ranging from a few to several tens of nanometers, largely depends on the choice of the liquid electrolyte. Yoon et al. determined the SEI thickness of Si in the half-cell composed of amorphous Si/$LiPF_6$-PC electrolyte/Li metal using in-situ AFM measurements [177]. They found that the SEI thickness by the end of the first lithiation is less than 5 nm and is $\sim$ 10 nm after the first cycle. Another report by Zheng et al. found that the SEI structure formed on Si is significantly inhomogeneous across the electrode surface [187]. The elastic moduli of the constituents of SEI are typically below 1 GPa with peak values around 4 GPa. With this information, it is possible to evaluate whether

the presence of SEI can lead to the incorrect estimation of the contact area between the tip and the Si film.

Plugging the reduced stiffness E_r into Equation 2.2 and taking $A_c \approx 25.4h^2$ gives the contact stiffness as a function of indentation depth in a material of a given elastic modulus, as follows:

$$S \approx 2\sqrt{\frac{\pi}{24.5h^2}}\left(\frac{1-v^2}{E}+\frac{1-v_i^2}{E_i}\right)^{-1}. \tag{2.9}$$

For a SEI layer of thickness 10 nm and modulus 1 GPa, the contact stiffness of approximately 60 N/m is obtained which is considerably lower than the surface detection criteria S>200 N/m. Thus, the measured indenter displacement should be insensitive to the compliant SEI layer and the influence of SEI in our experiments can be neglected. It is worth reiterating that SEI is a complex issue and its thickness can be substantially different under different cyclic conditions. One study reported that the SEI thickness is ranging from 7 to 20 nm depending on the electrochemical window, temperature, and electrolyte additives [187]. In operando indentation, a few approaches can be used to mitigate the effect of SEI such as increasing the indentation depth, using larger contact stiffness for surface detection, and narrowing the electrochemical window. The capability of CSM measurements to acquire mechanical properties as a function of the indentation depth is useful in detecting the SEI effect. A plot of the elastic modulus and hardness versus indentation depth would display a large change in slope as the indenter crosses from a softer SEI layer into a much stiffer electrode.

Now let's consider the effect of the substrate. The magnitude of substrate effects in indentations tests mainly depends on the ratios between (1) the indentation depth and the film thickness, and (2) the mechanical properties of the film and the substrate. A general rule is that the indentation depth of less than 10 % of the film thickness is sufficient to avoid excessive substrate effect [55, 54]. For the experimental setup used in this work, calibration tests on standard materials showed that 80 nm is about the shallowest indentation depth below which excessive noise compromises the

precision of the tests. Figure 2.7 compares the modulus and hardness of a thin Si film of 0.5 μm initial thickness (1.6 μm after full lithiation) and a thicker film of 1.4 μm thickness. The thick film was not suitable for operando tests as it experiences enormous structural degradation upon lithiation and is only used to evaluate the substrate effect. Figure 2.7 shows the modulus and hardness measured at different indentation depths by CSM for the two Si samples. The thin film is initially much more sensitive to the substrate. When the thin film is lithiated and expands in its thickness, the substrate effect is mitigated. The slope of elastic modulus with respect to the indentation depth changes its sign from negative to positive when Si is fully lithiated, which is a result of the film being initially stiffer than the silica substrate, but more compliant by the end of the lithiation (elastic moduli for pure Si, fully lithiated Si, and silica substrate are about 110 GPa, 50 GPa, and 70 GPa, respectively). At the indentation depth of 80 nm, the hardness of the thick and thin samples is about to converge while the elastic modulus differs by around 10 %. The comparison suggests that the deviation of the elastic modulus measurements for the thin Si film upon lithiation is bounded at approximately 10 %, which agrees with the models of substrate correction [54, 58, 40]. The application of substrate correction using the established models would require simplifying the underneath Cu, Ti, and silica multilayers to a single layer. In this work, the raw measurements (no substrate correction) are presented while acknowledging the bounded uncertainty resulted from the substrate effect.

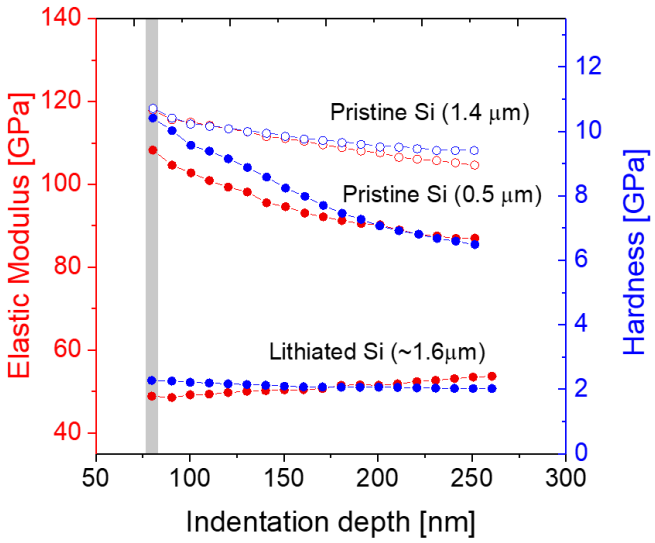

Figure 2.7. : Elastic modulus and hardness as a function of the indentation depth for the Si films of 0.5 μm (≈1.6 μm after lithiation) and 1.4 μm thickness. The slopes indicate the dependence of the measurements on the film thickness and properties of the substrate. The indentation depth 80 nm (grey area) is selected as a balance between the experimental accuracy and minimization of the substrate effect.

2.5 Results

Li metal ribbons are tested in a standard holder. The load-displacement curve of tests on lithium metal showed little elastic recovery, which indicates that pile-up could occur leading to an underestimation of the contact area, Figure 2.8(a). The report by [154] shows that Li exhibits work hardening which suppress pile-up. Inspections of the optical images of the residual impressions did not show obvious signs of pile-up, inset in Figure 2.8(a). The elastic modulus and hardness as a function of indentation depth is presented in Figure 2.8(b). The elastic modulus is close to the uniaxial tensile test measurement which is 7.8 GPa [146]. Creep results are discussed next along with the lithiated the Si data.

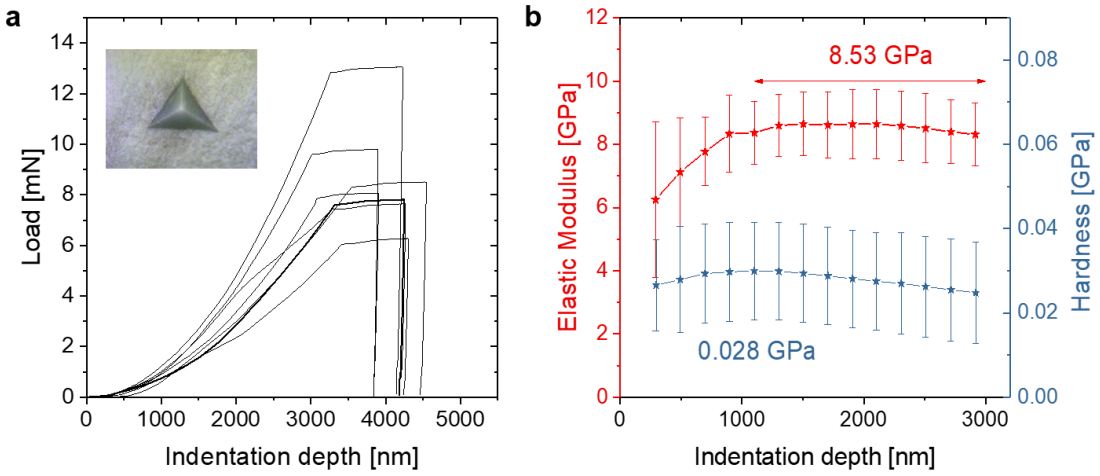

Figure 2.8. : The load-displacement curves for indentation of Li metal at different depths. (b) Elastic modulus and hardness of Li metal. The large variation in the results is possibly due to the surface roughness. The inset optical image shows a representative residual impression.

The continuous evolution of the mechanical properties of Si in the course of Li reactions is measured using operando indentation. The anasylis focus on the effects of (1) the Li composition and (2) the charging rate on the mechanical behaviors of lithiated Si. The test procedure is summarized in Figure 2.9, showing a complete set of electrochemical (voltage and current profiles) and indentation data (drift-rate, elastic modulus, and hardness) as a function of the discharge time. The electrical current alternates between zero and galvanostatic discharge at the specified C-rate until the cut-off voltage is reached. The drift-rate peaks at the initial application of the current and rapidly converges to a nearly constant value. The elastic modulus and hardness are approximately constant at open circuit (black circle) and decrease during discharge (blue circle). Notice that random drift introduced by the environment (circled in orange) and electrochemical drift (data points on grey background) can be corrected for simultaneously, not compromising the accuracy of modulus and hardness measurements. Obvious outliers resulting from indentation over surface defects and

data within a 20 min range from the opening and closing the circuit are rejected (black cross).

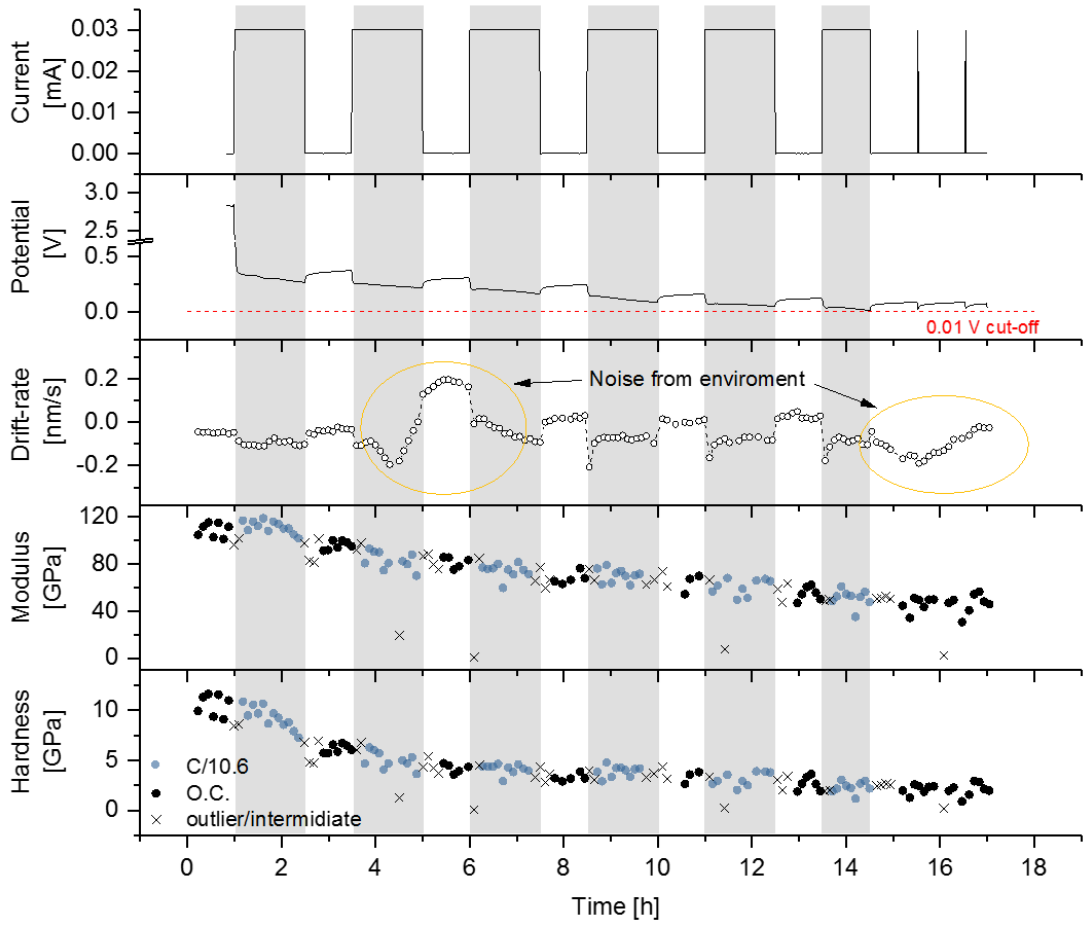

Figure 2.9. : Current and voltage profiles during the first lithiation of Si at C/10.6 and the corresponding indentation measurements.

The evolution of the mechanical response of the Si electrode during lithiation is evident in Figure showing the load-displacement curves of lithiated Si of different Li compositions. The tip displacement at peak load hold is increased with lithiation as results of creep. Also, the load at each given the indentation depth and the slope of the unloading curve decrease significantly from pristine to fully lithiated states.

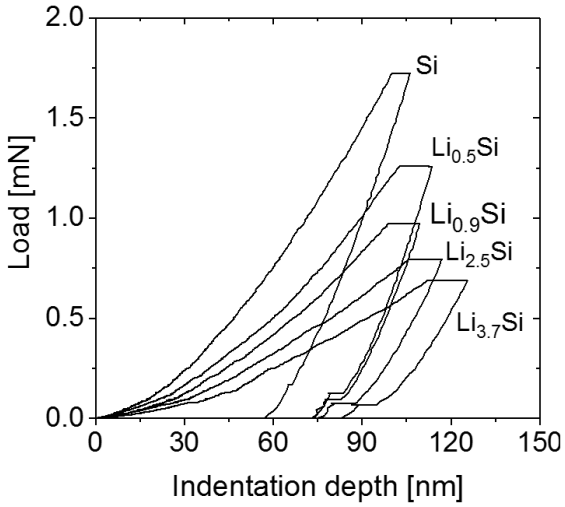

Figure 2.10. : The load-displacement curves of lithiated Si of different Li compositions.

The elastic modulus, hardness, and creep stress exponent as a function of Li concentration are summarized in Figures 2.11 (a), (b) and (c), respectively. Tests performed under the open circuit (O.C.) condition are presented with averages and standard deviations, while the single data points for different charging rates during cell operation represent individual indentations. The elastic modulus drops from approximately 110 GPa for pristine Si to 47 GPa for $Li_{3.2}Si$ (52% reduction), while the hardness decreases from 10.6 GPa to 2.2 GPa (78% reduction). Comparison with literature results (orange symbols) are presented in Figure 2.12 against slow charging rate data (blue and purple symbols for C/10.6 and C/30, respectively). The results are well within the range reported by ex situ measurements [56, 8, 153], confirming that the SEI layer has a negligible effect on the operando measurements and that the surface quality is sufficient for indentation tests. The comparisons with literature also highlights the advantage of the uninterrupted tests. In ex situ experiments, multiple samples are charged up to a specific state-of-charge, removed from the cell, and tested using different means to suppress oxidation such as covering the sample with inert oil and providing a continuous flow of inert gas. It appears that the variation of the experimental procedures may introduce some unnatural transitions

in the mechanical properties such as the up-and-down behavior of elastic modulus as a function of concentration by Hertzberg et al. [56]. The operando indentation results show the steady decrease of the modulus and hardness of lithiated Si, and the rule of mixture provides a reasonable approximation to capture this evolution of the mechanical properties.

Figure 2.11(c) shows the stress exponent of lithiated Si as a function of the Li composition under different charging rates. The results are obtained from the constant-load hold quasi-static measurements. The stress exponent for pure Si is approximately 50, or equivalently, the strain rate sensitivity is 0.02, with 0 meaning that the stress response is insensitive to the strain rate, and 1 representing Newtonian viscous flow. The comparison between the 0.5 μm (solid black circle) and the 1.4 μm (open red circle) thick pristine films indicates that the stress exponent is not significantly influenced by the substrate. The creep of lithiated Si behaves like a step function – the stress exponent dramatically decreases upon the start of lithiation and drops to 22 for $Li_{0.5}Si$. Afterwards, the stress exponent remains nearly constant for the Li composition over $Li_{0.5}Si$. A prior first-principles modeling demonstrated that the brittle-to-ductile transition occurred in $Li_{0.25}Si$ where a small fraction of Li mediated the flow of lithiated Si [186]. This transition is corroborated by our measurements of the stress exponents. The constant strain-sensitivity of lithiated Si over a wide range of compositions is intriguing and its mechanistic understanding remains to be explored in a future study. The stress exponent of approximately 22 for lithiated Si is in close agreement with ex situ nanoindentation measurements reported by Berla et al.[8] Other studies [146, 15, 154] on the viscoplastic properties of Li metal and lithiated Si adopted power-law type constitutive equations using the overstress ($\dot{\varepsilon} = A(\sigma - \sigma_0)^{\delta}$) instead of the absolute stress ($\dot{\varepsilon} = B\sigma^n$), where A and B are constants, σ is the flow stress, σ_0 is a reference stress, δ is the overstress exponent, and n is the conventional stress exponent. We want to point out this detail because the stress exponent and the overstress exponent are not equivalent. Normalizing the stress and strain rate, nevertheless, does not change the value of the exponent. The reported values of δ

for Li metal from uniaxial tensile experiments at various strain rates and indentation tests at constant loading rate are 1.75 [146] and 1.85 [154], corresponding to the stress exponents n of 11.9 and 9.0, respectively. These values are consistent with the result obtained in this work which is 8.1. We compare the QS creep results with the CSM output using the Maier method [97]. The stress exponent of partially lithiated Si is 20.4 for the holding time of 300 s, while the stress exponent of Li metal obtained from the 600 s holding is 8.8.

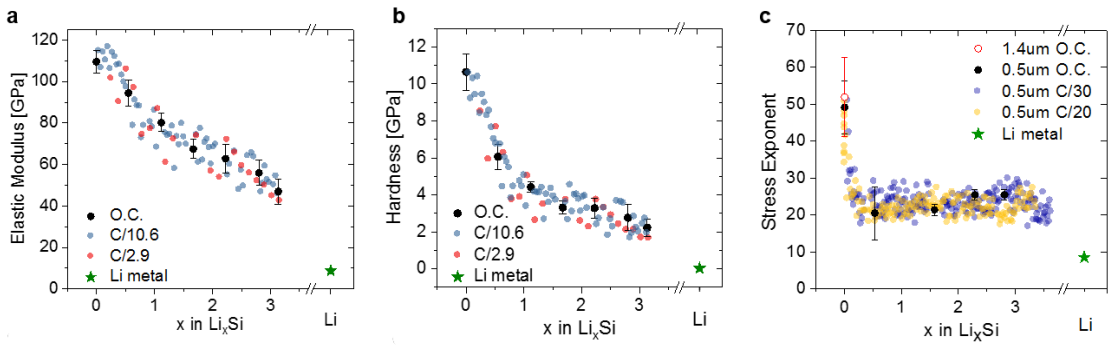

Figure 2.11. : (a) Elastic modulus, (b) hardness, and (c) stress exponent of Si (solid dots) measured as a function of Li concentration in open circuit (O.C.) and under various charging rates. Separate measurements performed on pure Li metal are included (green star).

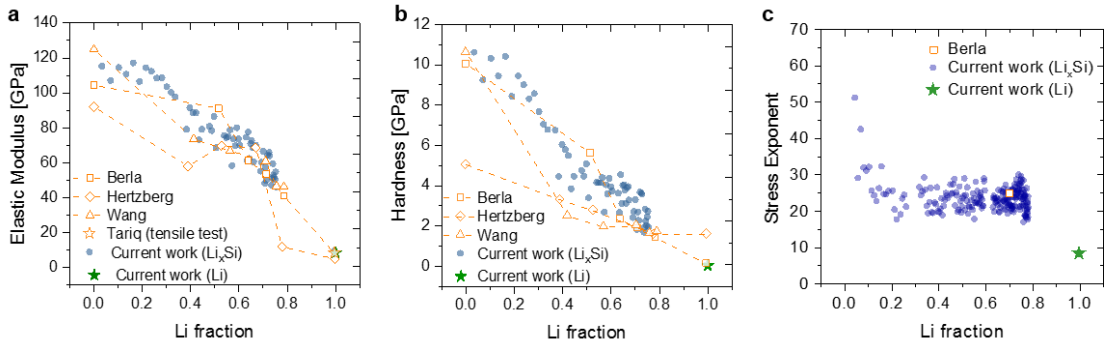

Figure 2.12. : (a) Elastic modulus and (b) hardness at C/10.6, and (c) stress exponent of Si at C/30 as a function of Li concentration (blue and purple symbols). Comparison with literature results (orange symbols) by Wang et al. [153], Hertzberg et al. [56], Berla et al. [8], and Tariq et al. [146].

The elastic modulus and hardness of lithiated Si for a given composition measured at different charging rates and under open circuit condition are nearly identical, Figures 2.11 (a) and (b). A few earlier studies proposed the dependence of the mechanical properties of electrodes on the charging rate. Brassart and Suo [14] postulated that under the non-equilibrium chemical state, the chemical driving force for reactions in a solid perturbs the valence states of the reactants and enables a material to flow under a lower level of stress than that at the chemical equilibrium state. Zhao et al.[186] found that the wafer curvature measurement of the biaxial stress in Si thin films cycled at 1C was lower than the yield strength obtained from first-principles modeling, and attributed such difference to this coupling between reaction and plastic flow (reactive flow). The coupling of chemical reactions and plasticity has also been studied by recent theories of anisotropic compositional expansion and glassy relaxation [79, 68]. The coupling between the mechanical properties and the chemical reaction rate is not evidenced by the operando indentation tests. For instance, the hardness, which is typically in a linear relationship with the flow stress, is about the same for the measurements at galvanostatic charging rates of C/2.9 and C/10.6 as well as at open circuit condition. This finding does not necessarily disproves the coupling

between the mechanical behaviors and the reaction rate in electrodes, because the coupling effects may be convoluted with the variation of the experimental output, or the timescales for the chemical reaction and plastic flow of lithiated Si may be vastly different which makes it difficult to capture by nanoindentation. Further investigation considering a wider span of charging rates and different materials is necessary to make more conclusive assessments of reactive flow and remains one of the research questions of this thesis. It is also worth noting that wafer curvature experiments on Si found that the flow stress increased by 0.1 GPa when the charging rate increased from C/128 to C/2 [121]. The authors attributed this effect to the strain-rate sensitivity. In wafer curvature experiments, the substrate bends proportionally to the stress developed in the film electrode, which depends on the rate of Li insertion as well as the viscoplastic properties of the electrodes. In nanoindentation, however, the strain rate and the electrochemical charging rate are separate – the strain rate $0.5\dot{P}/P = \dot{h}/h = \dot{\varepsilon}$ is provided by the load cell while the charging rate is controlled by the electrochemical station. Thus, differently than in curvature bending experiments, operando indentation allows the measurement of modulus and hardness of electrodes at a fixed strain rate independently of the charging rate.

2.6 Conclusion

This chapter introduced a platform for the local mechanical characterization of electrode materials in inert environment. The experimental setup enables the measurement of the dynamic chemomechanical response of electrodes during electrochemical reactions. The work addressed technical challenges associated with the custom testing environment, the structural degradation and the volumetric expansion of the electrodes, and the effects of the surface layer and the substrate. Results inform on the evolution of the elastic modulus, hardness, and creep stress exponent of lithiated Si with Li concentration. A couple interesting phenomena were observed which are not well understood at this time, and should be noted:

- The electrochemical drift-rate (that is, the rate of expansion rate due to lithium insertion) during the tritation experiment exhibits a peak upon the application of the current. This peak could have a significant impact in the structural degradation of electrodes due to the strain-rate sensitivity.

- The time-dependent deformation of Si films and its relationship with Li concentration. The creep exponent of pure Si in the order of 50 drops dramatically during the initial Li insertion and rapidly reaches a roughly constant value around 22, behaving similarly to a step function. In addition, at the composition of roughly Li_3Si, there is a slight increase in the stress exponent (from 22 to 25).

- Within the resolution of the experiment, the mechanical response of silicon electrode was shown to be insensitive to the chemical load up to $\sim$C/3 discharge rate.

In conclusion, the operando indentation technique is a promising tool that can help create knowledge on the intimate interactions between mechanics and electrochemistry such as stress-regulated ion diffusion [69], concurrent processes of plasticity and reaction [186, 14], corrosive fracture [59], and mechanical stability of electrodes in the long-term performance of batteries.

3. MECHANICS-INFORMED CHEMICAL PROFILING

This chapter is adapted from [35].

3.1 Introduction

The kinetics of Li reactions plays a decisive role in the rate capability and cyclic life of Li-ion batteries. Charge heterogeneity is a prevalent feature in the composite electrodes [170, 176]. The inhomogeneous distribution of Li is associated with issues such as underused and abused regions in the redox active materials and heterogeneous mechanical failure due to the localized strains and damage [101, 168]. The spatiotemporal distribution of Li provides essential information needed to identify the underlying rate-limiting mechanisms and to determine the material properties. The combination of chemical, temporal and spatial measurements on battery materials is a vast challenge because the instrument must be able to probe the sample without exposure to the atmosphere while still accommodating all necessary components to control the reactions and maintaining experimental accuracy.

Advanced techniques with the capability of probing the Li element are under fast development; nonetheless, current solutions still hold many practical limitations and are not easily accessible [57, 161]. Because of the low atomic number, Li detection is challenging and requires ultra-sensitive spectroscopy techniques such as electron loss spectroscopy (EELS) [151], secondary-ion mass spectrometry (SIMS) [11], and Auger electron spectroscopy (AES) [128]. Hence, most studies rely on indirect measurements to infer the local Li content. For instance, X-ray diffraction (XRD) tomography and atomic force microscopy (AFM) can be used to estimate the composition through local changes in density and volume [3, 7]. Optical microscopy and colorimetry are able to estimate the approximate Li content based on the changes in the optical

spectrum [20, 46, 50]. One of the most popular approaches is the measurement of lithiation state from the lattice parameters and crystal structures through transmission electron microscopy (TEM) and XRD tomography [44, 88]. A combination of different techniques is also often used to complement the capabilities and correlate different processes taking place at different scales [123, 163]. In this work, we use nanoindentation to probe the spatial distribution of Li over time by making use of the functional dependence of the mechanical properties of elastic modulus and hardness on Li composition [34]. We choose an amorphous Si (a-Si) thin film as a model system.

The incorporation of Si nanoparticles to graphite electrodes in recent years has enabled a 6% improvement in the specific capacity of commercial Li-ion batteries [106]. The research aimed at improving the reliability of Si anodes continues to grow worldwide, and pure Si electrodes represent an untapped potential for increasing the cell capacity by 40% [106]. A major challenge in Si-dominant anodes [84, 179] and other high-energy-density electrodes as well [6, 74, 167, 182] is the suppression of the mechanical degradation resulting from the inherently large strains associated with lithiation. Information on the kinetic processes associated with Li reactions is crucial to understand and manage mechanical stability as they dictate the buildup of mechanical stresses [171].

Despite the commercial interest in Si anodes, the kinetics of Li reactions in a-Si remains unclear. In 2013, two in-situ TEM studies under a large bias voltage [100, 152] and later a potentiostatic study [103] found that the first lithiation of a-Si took place via the propagation of a sharp interface between lithiated and pristine Si. Still, the following delithiation and cycling proceeded with an evolving, smooth concentration gradient. The sharp interface is a common phenomenon in reactions involving phase transformation; however, Si remains amorphous in these experiments. This observation sparked a debate concerning the underlying rate-limiting process, whether reaction-limited [100, 152] or diffusion-limited [103, 153], and on the structural changes of amorphous Si upon lithiation [30]. Another group compared the rate

performance of Si films during lithiation versus delithiation and found that amorphous Si exhibited better rate performance during delithiation, which was attributed to the cut-off voltage being more sensitive to the ohmic polarization during lithiation [82]. In contrast, a few recent studies proposed that the incomplete delithiation by Li trapping is one of the causes of fade in the cyclic efficiency of Si [89, 129, 189].

The complexity of the Li kinetics in Si and the limitation of existing experimental methods are underscored by another discrepancy in the literature about the Li diffusion coefficient in Si which spans over eight orders of magnitude [60, 136, 165, 178]. It is worth mentioning that electroanalytical techniques such as galvanostatic and potentiostatic intermittent titration (GITT and PITT) are amidst the most popular characterization tools. At the same time, many assumptions of the classical models for GITT and PITT may not uphold in Li-ion applications due to uncertainties arising from parasitic charge injections, varying or not well-defined active surface area (expanding and fracturing surfaces), additional rate-limiting effects (e.g., interfacial reactions), and stress effects on diffusion [63, 83, 147].

This work sets forth a nanoindentation approach to probe the spatiotemporal Li profile in the electrodes of LIBs. Figure 3.1 outlines the structure of the work. The nanoindentation experiments are performed on an a-Si thin film in contact with a Li metal and undergoing chemical lithiation in an argon-filled glovebox (step 1). The outcome of the experiments is the spatial maps of the hardness and elastic modulus of the sample at various lithiation times spanning over several days. The central circle in the sketch represents previous operando nanoindentation measurements of the mechanical properties and the size of lithiated Si upon controlled electrochemical lithiation [34]. The combination of the two experiments yields a spatiotemporal Li concentration map (step 2) that enables the calculation of the apparent diffusivity and tracer diffusivity of Li in Si as a function of the material composition (step 3). The knowledge about the Li distribution and internal stresses in the Si thin film allows a quantitative assessment of stress regulation on Li diffusion. The experimental conditions are simulated using finite element analysis (FEA). The numerical

simulations employing a two-way coupling between stress and diffusion validate experimental findings and elaborate the implications on the battery performance (step 4).

This work introduces a new characterization method on Li chemistry using the mechanics tool and provides valuable insights into the kinetic behaviors of battery materials. We find that the diffusion coefficient of Li in a-Si electrodes varies by at least three orders of magnitude with the Li composition. The highly concentration-dependent diffusivity leads to an asymmetrical rate capability and thus an asymmetrical accessible capacity of Si during lithiation versus delithiation. More broadly, this work demonstrates the potential of operando nanoindentation in aiding the research on redox active materials beyond simple mechanical characterization. We present one such application where the local mechanical response is used to inform the local chemical composition. Such an interdisciplinary platform does not only expand the experimental toolbox to detect the Li concentration but also makes it possible to evaluate the competing factors of chemical and mechanical driving forces of Li transport in a quantitative manner.

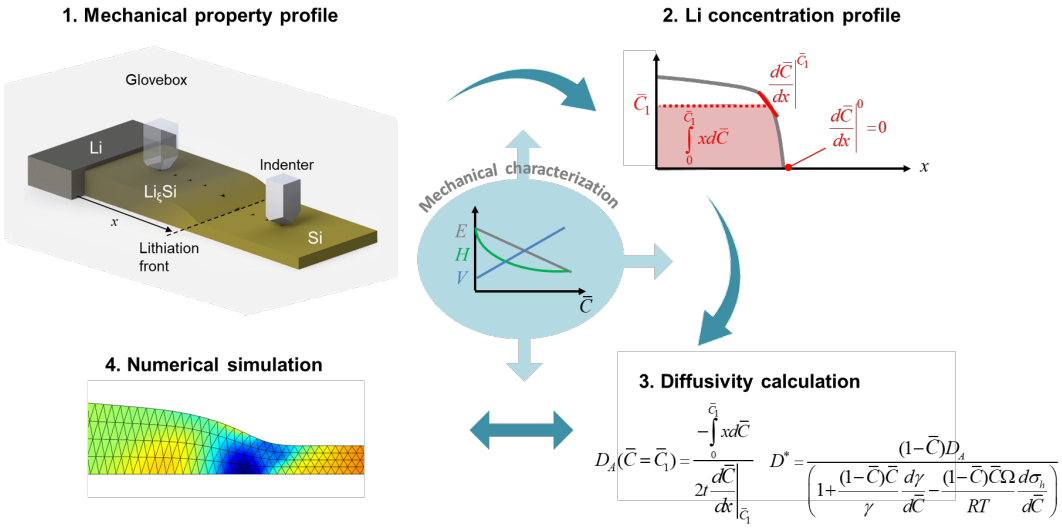

Figure 3.1. : Nanoindentation experiments for Li profiling in an a-Si thin film enable an examination of the lithiation kinetics and a quantitative study of Li diffusion under stresses. Nanoindentation probes the spatial distribution of the mechanical properties of the thin-film electrode undergoing chemical lithiation in an inert environment (step 1). Li concentration is obtained by converting the mechanical property profiles using their functional dependence on Li composition (step 2). The apparent diffusivity and tracer diffusivity of Li at a given material composition can be determined analytically based on the Li profiles (step 3). Finite element modeling validates the experimental output and evaluates Li transport under concurrent chemical and mechanical driving forces (step 4).

3.2 Experimental methods

3.2.1 Sample preparation

An amorphous silicon thin film (fabrication described in Section 2) was used in this work. It consists of stacked layers from top to bottom of: 500 nm Si, 300 nm Cu, 50 nm Ti, deposited over a 1 mm thick silica substrate. A commercial Li metal ribbon (99.9% purity, Sigma-Aldrich) was used to conduct chemical lithiation of the Si film.

3.2.2 Nanoindentation

Instrumented nanoindentation (Keysight G200) installed in an argon-filled glovebox (mBraun Labstar) is used to perform two sets of tests: (i) elastic modulus and hardness measurements and (ii) topography profiling. For (i), a Berkovich tip penetrates the sample with an indentation strain rate of 0.05 s^{-1}, until the indentation depth of 250 nm is reached. After a 10 s dwell time, the indenter partially withdraws, and the load is held constant for roughly 60 s to measure and correct the drift due to thermal and chemical effects [34]. The hardness and elastic modulus were determined through Equation (2.1) and Equation (2.2) using the Oliver-Pharr method as described in Section 2.3.2. The Poisson's ratio for Si is set to 0.22 [8], consistent with the Section 2.3.2.

The continuous stiffness measurement (CSM) method is again employed to measure the contact stiffness S as a function of the tip displacement from the in-phase material response to an oscillating signal superimposed on the semi-static indentation force [53]. The harmonic displacement and frequency of the superimposed signal are set to be 2 nm and 45 Hz, respectively. Same as in Section 2.3.2, the elastic modulus and hardness are extracted at an indentation depth of 80 nm to ensure a direct comparison between the two studies. For the test set (ii), the sample topography is profiled by maintaining the tip in contact with the sample through a small, constant load of 10 µN, while measuring the tip displacement as the stage moves with a velocity of 10 µm/s in the prescribed direction.

3.3 Theory of coupled diffusion and large elastoplastic deformation

This section outlines the theory of coupled diffusion and large elastoplastic deformation that we use in the finite element modeling of Li insertion in Si. It also describes the methodology that we use to derive the Li diffusivity, including the tracer diffusivity and apparent diffusivity, as a function of the Li composition based on the measured Li profiles. Due to the large specific capacity in the high-energy-density electrodes,

the kinetic processes of lithiation and delithiation are strongly coupled with the deformation non-linearity and mechanical stresses. The stresses alter the energy landscape of Li transport and place a significant effect on the charging/discharging kinetics of battery materials. Here we give a brief review of the continuum theory of coupled diffusion and large elastoplastic deformation [184] to facilitate the discussion of stress regulation on Li diffusion in computational modeling.

Kinematics of deformation

The material coordinates in the reference framework, $\mathbf{X}$, translate to the spatial coordinates in the current configuration, $\mathbf{x}$, by the displacement vector, $\mathbf{u}(\mathbf{X}, t)$:

$$\mathbf{u}(\mathbf{X}, t) = \mathbf{X} + \mathbf{u}(\mathbf{X}, t). \tag{3.1}$$

In the reference configuration, the mechanical equilibrium is enforced by

$$\nabla \cdot (\mathbf{FS}) = 0, \tag{3.2}$$

where $\nabla\cdot$ indicates the divergence in the reference configuration, $\mathbf{S}$ the second Piola-Kirchoff stress, and $\mathbf{F} = \frac{\partial \mathbf{x}}{\partial \mathbf{X}} = \nabla \mathbf{u} + \mathbf{I}$ is the deformation gradient. The deformation gradient contains elastic and inelastic contributions:

$$\mathbf{F} = \mathbf{F}_{el}\mathbf{F}_{inel}. \tag{3.3}$$

The inelastic contribution includes both the deformation by Li insertion and extraction, and deformation due to plasticity: $\mathbf{F}_{inel} = \mathbf{F}_{Li}\mathbf{F}_{pl}$. The Li induced deformation is assumed to be isotropic:

$$\mathbf{F_{Li}} = (1 + \Omega C)^{1/3}\mathbf{I}, \tag{3.4}$$

where Ω is the partial molar volume of Li in the host and C is the molar concentration in the reference configuration. Li induced inelastic volume change per unit reference volume is given by $J_{Li} = \det(\mathbf{F_{Li}}) > 0$. The plastic deformation accounts for the

shape change while keeping the volume constant, $J_{pl} = \det(\mathbf{F_{pl}}) = 1$. The overall volume change per unit of reference volume is

$$J = \det(\mathbf{F}) > 0. \tag{3.5}$$

We choose an elastic and perfectly plastic constitutive model. The second Piola-Kirchoff stress is determined by

$$\mathbf{S} = J_{inel}\mathbf{F}_{inel}^{-1}(\mathbf{C} : \epsilon_{\mathbf{el}})\mathbf{F}_{inel}{}^{-T}, \tag{3.6}$$

where ":" represents the double contraction between the fourth-order stiffness tensor $\mathbf{C}$ and the second-order elastic Green-Lagrange strain tensor,

$$\epsilon_{\mathbf{el}} = \frac{1}{2}(\mathbf{F_{el}}{}^{T}\mathbf{F_{el}} - \mathbf{I}). \tag{3.7}$$

The second Piola-Kirchoff stress $\mathbf{S}$ (reference configuration) relates to the Cauchy stress σ (current configuration) as

$$\sigma = J^{-1}\mathbf{F}\mathbf{S}\mathbf{F}^{T}. \tag{3.8}$$

We use the von Mises stress yield criterion for the plastic deformation. The yield function is written as

$$F_y = \sigma_{mises} - \sigma_y = \sqrt{\frac{3}{2}\sigma_d : \sigma_d} - \sigma_y. \tag{3.9}$$

where σ_d is the deviatoric stress and σ_y is the yield stress. The plastic flow rule follows [92]:

$$\dot{\mathbf{C}}_{\mathbf{pl}}^{-\mathbf{1}} = -\frac{2\lambda}{J}\mathbf{F}^{-1}\frac{\partial F_y}{\partial \sigma}\mathbf{F}\mathbf{C}_{\mathbf{pl}}^{-1}, \tag{3.10}$$

where $\mathbf{C}_{\mathbf{pl}}^{-\mathbf{1}} = \mathbf{F}_{\mathbf{pl}}^{-1}\mathbf{F}_{\mathbf{pl}}^{-T}$ and $\dot{\mathbf{C}}_{\mathbf{pl}}^{-\mathbf{1}} = (\dot{\mathbf{F}}_{\mathbf{pl}}^{-1}\mathbf{F}_{\mathbf{pl}}^{-T} + \mathbf{F}_{\mathbf{pl}}^{-1}\dot{\mathbf{F}}_{\mathbf{pl}}^{-T})$. The yield function F_y and the plastic multiplier λ fulfill the Kuhn-Tucker conditions:

$$\lambda \geq 0, F_y \leq 0, \lambda F_y = 0. \tag{3.11}$$

Kinetics of diffusion

In order to derive the driving forces for diffusion, it is necessary to establish the diffusion mechanism. Si diffusion is several orders of magnitude slower than that of Li [64, 156], and therefore Si is considered to be immobile. For simplicity, and following the previous studies [15, 36], we assume that Li diffusion takes place by hopping through a fixed network of available sites. In this case, the driving force for Li diffusion is the difference between the chemical potential of Li, μ_{Li}, and the chemical potential of the vacant sites, μ_V. This potential difference is called the diffusion potential and it takes the following form [75, 148]:

$$\Phi = \mu_{Li} - \mu_V = \mu_0 + RT \ln\left(\gamma \frac{\bar{C}}{1-\bar{C}}\right) - \sigma_h \Omega, \tag{3.12}$$

where μ_0 is a reference potential, R is the gas constant and T is the temperature, and γ is the activity coefficient. The hydrostatic stress is $\sigma_h = tr(\sigma)/3$, and $\bar{C}$ is the normalized Li concentration, where $\bar{C} = 1$ corresponds to the fully lithiated state (all available sites for Li are occupied) and $\bar{C} = 0$ corresponds to pure Si. It is worth noting that diffusion in an amorphous network is complex [4, 16] and other effects such as some degree of void relaxation and site nucleation could also play a role [13, 87]. Li flux in the deformed configuration is given by

$$\mathbf{j} = -\frac{cD^*}{RT} \nabla_x \Phi. \tag{3.13}$$

where c and ∇_x are the Li concentration and the gradient in the deformed configuration, respectively. $M = D^*/RT$ is the mobility, where the coefficient D^* is known as the tracer diffusivity [5] or self-diffusivity [4]. Li flux in the undeformed configuration [172] can be derived as

$$\mathbf{J} = -\frac{CD^*}{RT} \mathbf{F}^{-1}\mathbf{F}^{-T} \nabla \Phi. \tag{3.14}$$

Mass conservation is enforced by

$$\frac{\partial C}{\partial t} = -\nabla \cdot \mathbf{J}. \tag{3.15}$$

3.4 Derivation of diffusivity based on Li profiles

We calculate the diffusion coefficient of Li in lithiated Si ($Li_\xi Si$) based on the Li profiles using the Matano-Boltzmann (M-B) approach [124]. Here this approach is validated for Li diffusion under stress. In the experiments, the Li metal is placed in direct contact with the a-Si film. At a given time, the spatial Li distribution within the Si film is obtained by measuring the elastic modulus and hardness of lithiated Si and also by scanning the topography of the film. In this setup of chemical lithiation, Li diffusion is approximated as a one-dimensional problem with the concentration varying mostly along the longitudinal direction x as shown in Figure 3.1. For now, we neglect the effect of surface diffusion and assume a homogeneous distribution of Li across the film thickness. We will estimate the uncertainty brought by the surface diffusion of Li in a later section. Since the Si film is constrained by the substrate, lithiated Si expands mostly in the direction perpendicular to the substrate, and the deformation along the longitudinal direction is negligible ($x \approx X$). The shear deformation (the off-diagonal terms of $\mathbf{F}$) is also small relative to the thickness change of the film. Equation (3.15) can be recast into the one-dimensional form:

$$\begin{aligned}\frac{\partial \bar{C}}{\partial t} &= \frac{\partial}{\partial x}\left(\frac{\bar{C}D^*}{RT}\frac{\partial \Phi}{\partial x}\right) \\ &= \frac{\partial}{\partial x}\frac{D^*}{(1-\bar{C})}\left(1+\frac{(1-\bar{C})\bar{C}}{\gamma}\frac{\partial \gamma}{\partial \bar{C}}-\frac{\Omega(1-\bar{C})\bar{C}}{RT}\frac{\partial \sigma_h}{\partial \bar{C}}\right)\frac{\partial \bar{C}}{\partial x},\end{aligned} \tag{3.16}$$

where $\bar{C} = C/C_{\max}$ is the normalized concentration in the reference configuration. $C_{\max}$ is the Li concentration in fully lithiated Si, $Li_{3.75}Si$ [51]. Here we name the pre-factor to the concentration gradient in Equation (3.16) as the apparent diffusivity D_A, such that

$$\frac{\partial \bar{C}}{\partial t} = \frac{\partial}{\partial x}\left(D_A\frac{\partial \bar{C}}{\partial x}\right), \tag{3.17}$$

where

$$D_A = \frac{D^*}{(1-\bar{C})}\left(1+\frac{(1-\bar{C})\bar{C}}{\gamma}\frac{\partial \gamma}{\partial \bar{C}}-\frac{\Omega(1-\bar{C})\bar{C}}{RT}\frac{\partial \sigma_h}{\partial \bar{C}}\right). \tag{3.18}$$

For diffusion in a semi-infinite medium with a constant-concentration boundary condition and the apparent diffusivity being a sole function of the composition, the

M-B approach can be readily adopted to determine the diffusivity as a function of the material composition [10, 28, 108]. In the experiments, the Si film is sufficiently long so that lithiation does not reach the opposite end of the film. The timescale of the experiments (several days) is also sufficient to ensure the boundary of Si in direct contact with Li is at the fully lithiated state for the duration of the experiments. If the apparent diffusivity in Equation (3.18) can be expressed as a single function of composition, that is,

$$D_A = D_A(\bar{C}, \sigma_h, D^*, \gamma) = D_A(\bar{C}), \tag{3.19}$$

the Boltzmann transformation using the variable $\lambda \equiv x/t^{1/2}$ will be applicable. Considering that the system is isothermal, the material properties are history independent, and that the stress field can be uniquely determined by the Li composition (more discussions in Section 3.6.2), Equation (3.19) holds and the diffusion kinetics in the set of experiments would be indistinguishable from that of a classical Fick's law. Additional discussions on some special cases where the self-stress (diffusion-induced stress) results in a deviation from Fick's behavior can be found in the literature [76].

With the introduction of the Boltzmann variable $\lambda \equiv x/t^{1/2}$, Equation (3.17) can be written into an ordinary differential equation:

$$-\frac{\lambda}{2}\frac{d\bar{C}}{d\lambda} = \frac{d}{d\lambda}\left(D_A \frac{d\bar{C}}{d\lambda}\right). \tag{3.20}$$

In the experiment, the concentration is expected to saturate quickly and remain fixed at the boundary with the Li metal, $\bar{C}(x = 0, t > 0) = \bar{C}(\lambda = 0) = C_S$, and the film is sufficiently long that it can be assumed to be semi-infinite, $\bar{C}(x = +\infty, t > 0) = \bar{C}(\lambda = +\infty) = 0$. Integrating Equation (3.20) from $\lambda = +\infty$ to $\lambda = x/\sqrt{t}$, and knowing that $D\frac{d\bar{C}}{d\lambda} = 0$ when $\bar{C} = 0$, it gives [28, 116]:

$$D_A(\bar{C} = \bar{C}_1) = \frac{-\frac{1}{2t}\int_0^{\bar{C}_1} x\, d\bar{C}}{\left(\frac{d\bar{C}}{dx}\right)\Big|_{\bar{C}_1}} \tag{3.21}$$

While the apparent diffusivity D_A can be calculated directly from the Li profile, the tracer diffusivity D^* requires knowledge about the evolving stress field and the

material non-ideality. Following the previous work [148, 160], the activity coefficient γ is derived by assuming that the excess free energy can be modeled as a series expansion in $\bar{C}$:

$$RT\ln(\gamma) = \sum_{k=2}^{N} \Omega_k k \bar{C}^{k-1}, \tag{3.22}$$

where Ω_k are a set of self-interaction coefficients. In this work, we use the self-interaction coefficients for $Li_\xi Si$ ($0 \leq \xi \leq 3.75$) that were fit to the open-circuit potential data in first-principles modeling [15, 24]. The estimation of the hydrostatic stress within the lithiated Si will be discussed in detail in Section 3.6.2.

3.5 Finite element implementation

We use finite element modeling to simulate the concurrent diffusion and stresses in the Si thin film upon chemical lithiation and demonstrate the implications of the experimental output on the battery performance. The weak formulations of the deformation kinematics and the diffusion kinetics can be found in a previous work [168]. The specific conditions relevant to the current study will be explicitly stated. The multiphysics time-dependent solver MUMPS (Multifrontal Massively Parallel sparse direct Solver) in COMSOL is used to solve the co-evolution of the concentration and stress fields. The order and shape of the test functions for the diffusion potential $\Phi(\mathbf{X}, t)$ and displacement $u(\mathbf{X}, t)$ are quadratic Lagrange and cubic Lagrange, respectively.

3.6 Results

We adopt a nanoindentation approach to quantitatively measure the composition gradient in a material by means of its known mechanical properties. A model system consists of an a-Si film laterally in contact with a Li metal ribbon (schematic in Figure 3.1, step 1). Chemical lithiation proceeds spontaneously from the Li metal side towards the other end of the Si film. The test is conducted in an argon-filled

environment with the H_2O and O_2 levels below 0.5 ppm. Optical microscopy images on the top surface of the film show that the lithiation process is marked by a sharp color contrast, roughly in parallel to the Li|Si contact, which propagates over time. The sharp contrast corresponds to the interface between lithiated and pristine Si. The dark spots behind the Li front are blisters/defects generated by the Li sweeping through the Si film.

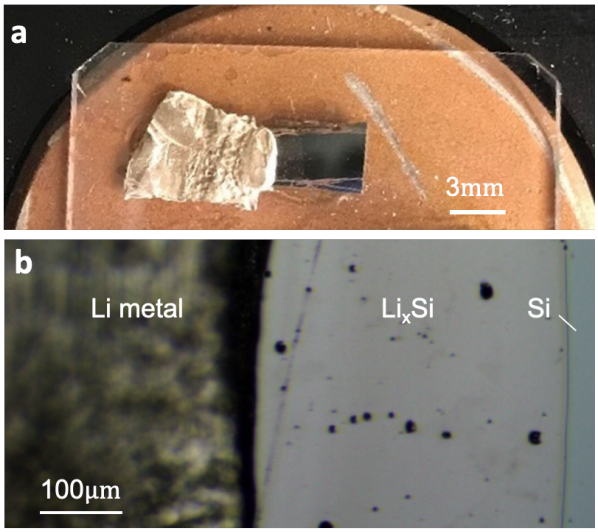

Figure 3.2. : (a) Top view of the experiment showing the Li metal in direct contact with the silicon film. (b) Close at view showing the contrast between pristine and lithiated silicon.

We track the position of the lithiation front starting from a reference position x_{ref} at $t = 30$ h, Figure 3.3(a) and 3.3(b). $t = 0$ h corresponds to the time at which the Li metal is placed in contact with the Si film. Figure 3.3(c) plots the displacement of the moving front Δx as a function of $\sqrt{t}$. The position of the lithiation front is measured at three separate locations for each given time. The dotted line shows a linear fitting of the experimental results. The constant slope between Δx and $\sqrt{t}$ is a strong indication of diffusion-limited kinetics of lithiation in the amorphous Si thin film. This result is different from the observation of previous TEM studies that the first lithiation of a-Si proceeds via a two-phase and two-step mechanism [100, 152].

Such discrepancy is likely due to the very different time scales in the experiments (i. e., seconds in TEM characterizations versus tens of days in this measurement) and also possibly caused by different experimental conditions (i. e., a large bias voltage applied in TEM experiments versus chemical lithiation without an applied voltage in the current work). Another study using AES concluded that Li reaction in a-Si at a conventional charging rate proceeds via single phase kinetics [153].

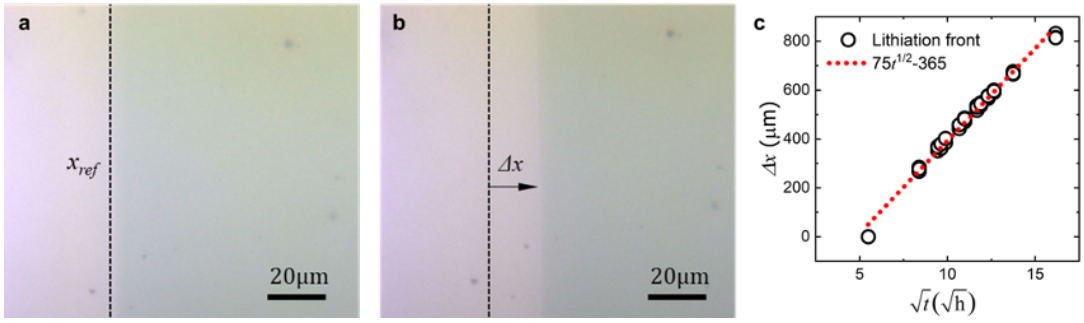

Figure 3.3. : Optical images of the moving lithiation front in an amorphous Si thin film upon Li reaction at (a) a reference time and (b) an elapsed time Δt. (c) Measurement of the moving front at three separate locations for each given time (circles) and the linear fitting (dotted line). The constant slope between Δx and $\sqrt{t}$ indicates diffusion-limited kinetics of lithiation in the amorphous Si thin film.

3.6.1 Li profiling and apparent diffusivity

We track the spatial distribution of the hardness and elastic modulus over time in the lithiated Si thin film by performing multiple arrays of indentations along the lithiation direction. Figure 3.4(a) shows an example of the elastic modulus (black squares) and hardness (red triangles) as a function of the distance from the Li source at the time $t = 150$ h. The inset plot is reproduced from our previous operando nanoindentation experiment [34] and shows the dependence of the elastic modulus and hardness on the Li concentration in Si, where $\bar{C} = 0$ corresponds to pure Si and $\bar{C} = 1$ to fully lithiated Si ($Li_{3.75}Si$). The load-displacement curves, as well as the

complete elastic modulus and hardness data as a function of the indentation depth for the nanoindentation array in Figure 3.4(a) is shown in the Figure 3.5. Combining the spatial distribution of the mechanical properties and their one-to-one relationship with the Li concentration, Li profiles in the a-Si thin film can be mapped. For instance, the elastic modulus and hardness ahead of the lithiation front (light blue regimes in Figure 3.4) are roughly 110 GPa and 10 GPa, respectively, which correspond to the properties of pristine Si. Closer to the Li metal, the elastic modulus is 50 GPa and hardness is 2 GPa, which indicates a Li composition of $\bar{C} \sim 0.75$, or $Li_{2.8}Si$. In addition, we take advantage of the volumetric expansion of Si upon Li insertion to determine the local material composition based on the known relationship between the volumetric strain and the Li content [177]. Figure 3.4(b) shows the thickness profile of the film at the time $t = 143$ h. The spike marked by cross-symbols represents a type of whisker that grows during lithiation out of the pre-existing blisters from the deposition process. These spikes are discarded in our analysis. The dashed lines in Figures 3.4(a) and 3.4(b) show the filtered and smoothed data used to compute the Li concentration.

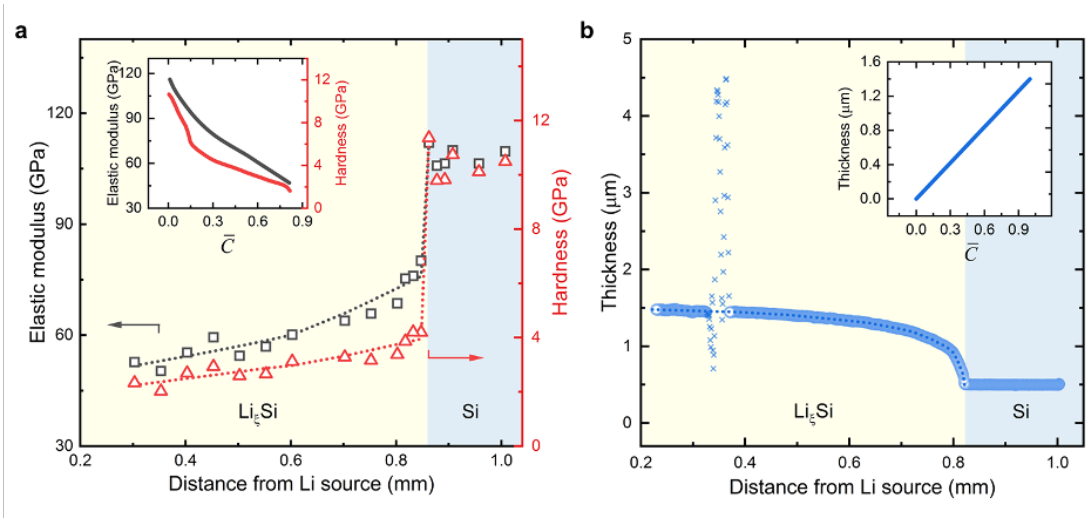

Figure 3.4. : Spatial distributions of (a) the elastic modulus and hardness, and (b) film thickness along the Li propagation direction. The insets show the elastic modulus, hardness, and film thickness as a function of the Li concentration. The inset functions convert the mechanical measurements to the Li profiles.

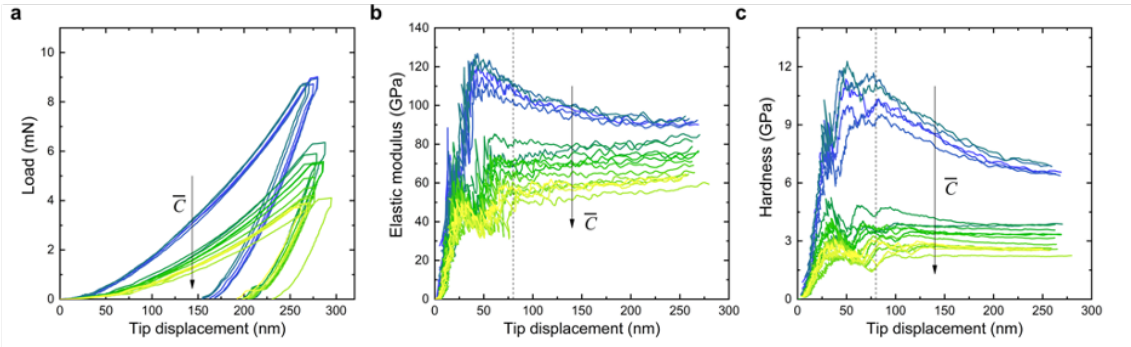

Figure 3.5. : Raw nanoindentation data corresponding to the indentation array in Figure 3.4(a). (a)-(c) shows the load-displacement curves, elastic modulus, and hardness as a function of the tip displacement, respectively. The dashed lines in (b) and (c) indicate the depth of 80 nm used for the extraction of the mechanical properties. The color gradient from blue to yellow indicates the increasing Li concentration.

Following the spatial scanning of the mechanical properties and the topology of the amorphous thin film at different times, the equivalent concentration across the lithiation propagation direction is determined using the inset functions in Fig 3.3(a) and 3.3(b), and plotted in Figure 3.6. A total of 10 test batches were conducted at different times in the course of 11 days, alternating between topography and mechanical properties measurements. For each batch, the sample was profiled at three separate positions across the width of the sample (near each edge and at the center perpendicular to the moving front direction) to verify that the results are independent of the choice of the measured location.

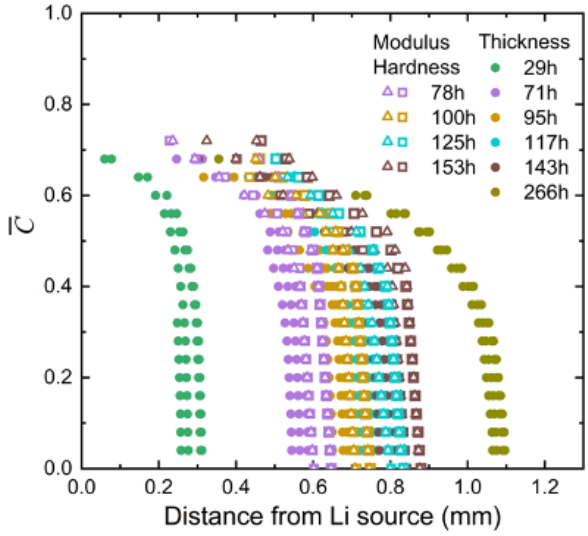

Figure 3.6. : Li concentration profiles determined from the elastic modulus measurements (empty triangles), hardness measurements (empty squares), and film thickness measurements (solid circles).

The dashed and dotted lines in Figure 3.7(a) indicate the averaged Li profiles in the two sets of experiments. The position of the moving lithiation front determined from the optical images (dashed line in Figure 3.3(c)) is reproduced in Figure 3.7(a) (continuous line) and is consistent with nanoindentation measurements. For each Li

concentration profile measured at a given time, we calculate the apparent Li diffusivity D_A using Equation (3.21). Note that D_A represents the proportionality coefficient between the gradient of Li concentration and the Li flux in Equation (3.17), and it does not differentiate the mechanical and chemical driving forces for Li diffusion. The solid grey, pink, and blue lines in Figure 3.7(b) show the median apparent diffusivities calculated from the Li profiles through the modulus, hardness, and thickness measurements, respectively, while the shadowed areas indicate the range between the 25% and 75% percentiles. The dashed line in Figure 3.7(b) shows that an exponential form $D_A = D_{\min} \exp\left(\frac{\bar{C}}{0.65} \ln\left(\frac{D_{\max}}{D_{\min}}\right)\right)$ with $D_{\max} = 1 \times (10^{-12})$ m^2/s and $D_{\min} = 1 \times (10^{-15})$ m^2/s matches well with the experimental data. This exponential form of Li diffusivity explains the steep concentration gradient observed by the optical microscope – the slow diffusion of Li in the pristine Si (as compared to lithiated Si) acts as a bottleneck for Li flux and causes the accumulation of Li at the lithiation front. Indeed, prior theoretical and experimental studies reported that Li diffusivity in amorphous Si was higher in the lithiated state than in the pristine state [26, 60, 103, 137, 156, 165]. Nevertheless, the shape and magnitude of the Li diffusivity vary widely across the literature. We will discuss the literature results in more detail in Section 3.6.2.

The colored contour plot in Figure 3.7(a) shows the concentration profile through the finite element modeling using $\frac{\partial \bar{C}}{\partial t} = \frac{\partial}{\partial X} D_A \frac{\partial \bar{C}}{\partial X}$ as the governing equation and the measured apparent diffusivity as the input parameter. This phenomenological equation does not distinguish the specific driving force for Li diffusion, instead, both the chemical and mechanical effects in the diffusion potential are embedded in the experimental value of the apparent diffusivity D_A. We note that Li concentration in the experiments is not measured all the way up to $x = 0$ to prevent collision of the tip with the Li metal; hence, the equilibrium concentration C_S at the boundary where Si is in contact with Li is not directly measured. It is possible that the equilibrium concentration at the boundary of the Li-Si contact does not reach the theoretical maximum value ($\bar{C}_S < 1$) due to the stress effect. We will show that this equilibrium concentration is approximately $\bar{C}_S \sim 0.8$ in a later section. In the finite element

modeling, we assume that the exponential form of the apparent diffusivity D_A can be extrapolated to higher concentrations. The contour plot in Figure 3.7(a) shows that the numerical result with the concentration $\bar{C}_S = 0.76$ at the boundary matches well the experimental profiles. This comparison demonstrates that the solution of a simple Fick's equation is sufficient to reproduce the experimental output reasonably well. The Fickian diffusion here does not exclude the stress effects on diffusion. If the stress significantly alters the diffusion potential, the result indicates that the hydrostatic stress depends solely on the Li concentration [76, 77]. Next, we will quantify the stress modulation on Li diffusion based on the Li profiles and the relatively simple internal stresses in the a-Si thin film.

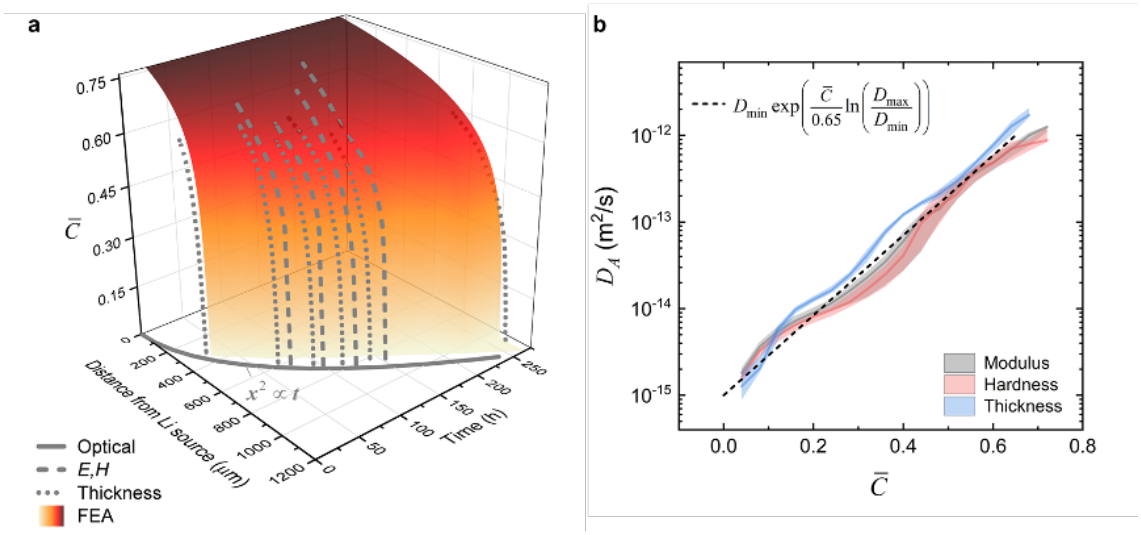

Figure 3.7. : (a) The spatiotemporal distribution of Li concentration. The grey lines show the results from the nanoindentation measurements of the elastic modulus and hardness (dashed lines), the thickness profiles (dotted line), and the optical imaging of the moving lithiation front (solid line). The contour plot shows the FEA results. (b) The apparent Li diffusivity as a function of the Li composition determined by the experimental results in (a). The experimental conditions are simulated in FEA using the exponential diffusivity function shown by the dashed line in (b). The numerical results of the Li profile are contour plotted in (a) to compare with experiments.

3.6.2 Assessment of stress effect on diffusion

Mechanical stresses alter the rate of diffusion by altering the following factors: (i) the diffusion potential , (ii) the equilibrium concentration at the boundary condition, and (iii) the activation energy barrier for diffusion [77, 122]. As discussed in Sections 3.3 and 4.1, the effect (ii) does not interfere with the diffusivity measurement as long as the time needed for the boundary concentration to reach equilibrium is considerably shorter than the duration of the experiment. It is worth noting that the effect (iii) alters Li flux even if the stress field is uniform, whereas the effect (i) impacts the Li distribution only by the presence of a stress gradient. The stress sensitivity of the activation barrier for diffusion in amorphous materials is generally small [4, 102]. More specifically, for Li diffusion in amorphous Si, two earlier studies evaluated the stress effect via ab-initio molecular dynamics [37, 119]. Both studies found that the difference of the tracer diffusivity under a homogeneous 1 GPa compressive stress versus the stress-free tracer diffusivity is less than 10%. This difference is small compared to the drastic change of the Li diffusivity with the composition (over three orders of magnitude), and therefore this effect is neglected in this work.

The tracer diffusivity D^* is an intrinsic material property, independent of the stress gradients, while the apparent diffusivity D_A is a convoluted property that includes the effects of material non-ideality and mechanical driving force. If the functions γ, σ_h and D_A are known, the tracer diffusivity, D^*, can be determined from Equation (3.18). Here we adopt the activity coefficient of lithiated a-Si from a prior study [15]. The activity coefficient γ was obtained from DFT calculations of the open-circuit potential, as discussed in Section 3.4, and it is a strong function of the Li concentration. To decouple the effects of the mechanical stress and the material non-ideality on Li diffusion, we construct a 2D plane-strain thin film model with symmetric displacement boundary conditions applied on the left and right edges of the sample, traction-free top surface, and stiff spring foundation on the bottom surface. The spring foundation allows a small degree of deformation in the x-direction ($< 0.1\,\mu m$)

which helps numerical convergence, and it is reasonable given that the Cu and Ti buffer layers below the Si film in the experiment may deform slightly. The initial concentration is zero everywhere except for the left edge where a fixed concentration boundary condition of $\bar{C} = 0.76$ is prescribed to mimic the contact with the Li metal. Li flux is determined by the equation $\mathbf{J} = -D_A \mathbf{F}^{-1}\mathbf{F}^{-T}\nabla\bar{C}$. The thickness of the model is the same as in the experiment, and the length is sufficiently large such that the lithiation front does not reach the opposite edge. Lithiation induced volumetric expansion is described by Equation (3.4) where $\Omega = 2.8/C_{\max}$ [177]. The theoretical maximum concentration $C_{\max}$ corresponds to $Li_{3.75}Si$ [24]. We use the elastic and perfectly plastic constitutive law to describe lithiated Si. The elastic modulus $E = -80\bar{C} + 120$ GPa and the yield stress $Y \cong \frac{H}{3.5} = -3.15\Theta_{Li} + 3$ GPa are adopted from the nanoindentation measurements (de Vasconcelos et al., 2017), where $\Theta_{Li} = \frac{\xi}{1+\xi}$ is the atomic fraction of Li in $Li_\xi Si$. The proportionality factor of 3.5 between the hardness and the yield stress is an approximation [144]. For metallic glasses, this factor typically ranges from 2.7 to 3.7 [181]. Figure 3.8 shows that the yield stress function Y from the nanoindentation experiments is within the range of literature values [31, 112, 120, 134, 186].

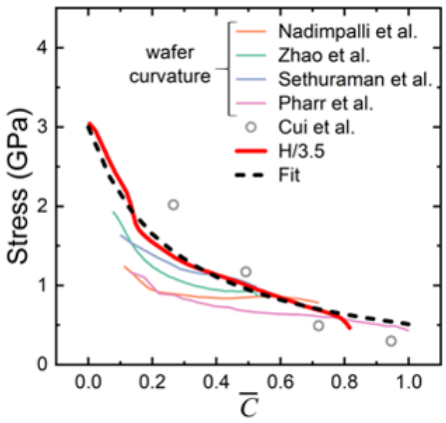

Figure 3.8. : Yield stress of lithiated Si in literature including the nanoindentation hardness measurement [34], wafer curvature measurements [112, 120, 134, 186], and DFT calculations [31].

Figure 3.9(a) plots the hydrostatic stress at the top (grey lines) and bottom (black lines) surfaces of the film at the times $t = 1$ h (dotted lines) and $t = 20$ h (solid lines). The inset shows the stress profiles within a 10 µm section near the lithiation front. At $t = 1$ h, the hydrostatic stress varies at the top and bottom surfaces and is not uniquely determined by the Li concentration. At $t = 20$ h, the hydrostatic stress in the thickness direction reaches a steady-state and the film is mostly in a state of biaxial stress. The compressive stress increases sharply at low Li concentration and then is capped by the yield strength of the film. The computational result of the hydrostatic stress in the plastic regime agrees well with the biaxial stress state $\sigma_h = -\frac{2}{3}Y$ (dashed red line in Figure 3.9(a)).

With the Li concentration, the stress field, and the thermodynamic activity coefficient determined, we are able to decouple the effects of the mechanical stress and the solution non-ideality on the apparent diffusivity. Figure 3.9(b) shows the correction factor due to the gradient of the hydrostatic stress and the gradient of the activity coefficient with respect to the Li concentration (inset equation of Figure 3.9(c)). Regarding the stress effect, because the thin film deforms mostly within the plastic regime and the yield stress decreases as the concentration increases, $\frac{dY}{d\bar{C}} < 0 \rightarrow \frac{d\sigma_h}{d\bar{C}} > 0$, Equation (3.18) shows that the hydrostatic stress in the thin film minimizes the apparent diffusivity of Li. In other words, the mechanical stress in the Si thin film hinders Li insertion as compared to a stress-free film. This effect is opposite when the thin film deforms within the elastic regime and the magnitude of the compressive stress increases with the Li composition, leading to $\frac{d\sigma_h}{d\bar{C}} < 0$, which accelerates Li insertion. The comparison of the correction factor due to the solution non-ideality and the mechanical stress in Figure 3.9(b) shows the fact that, if Si had been treated as an ideal solution, $\frac{\left(1-\bar{C}\right)\bar{C}}{\gamma}\frac{d\gamma}{d\bar{C}} = 0$, the stress term in the apparent diffusivity would lead to a negative tracer diffusivity D^* because $\frac{\left(1-\bar{C}\right)\bar{C}\Omega}{RT}\frac{d\sigma_h}{d\bar{C}}$ is larger than 1 in the concentration range of $\bar{C} = 0.1 \sim 0.4$. This scenario violates the Onsager's symmetry law which is necessary to ensure a positive generation of entropy (Balluffi et al., 2005). Given the dominant effect of the material non-ideality, it is crucial to consider the

stress effect on diffusion relative to the chemical driving force. This observation is in agreement with an earlier analysis (Sheldon et al., 2012) which determined that an ideal solution model for lithiated Si leads to an overestimation of the change in the equilibrium composition induced under mechanical stress.

Figure 3.9(c) is the plot of the apparent diffusivity (dashed line) and the tracer diffusivity (solid line) of Li. The data beyond $\bar{C} = 0.76$ are a mathematical extrapolation. The difference between the tracer and apparent diffusivities of about one order of magnitude is largely due to the thermodynamic activity coefficient as shown in Figure 3.9(b). Again, the apparent diffusivity is not an intrinsic material property and it depends on the stress state of the host upon Li reactions, whereas the tracer diffuvisity is intrinsic and independent of the stress gradients.

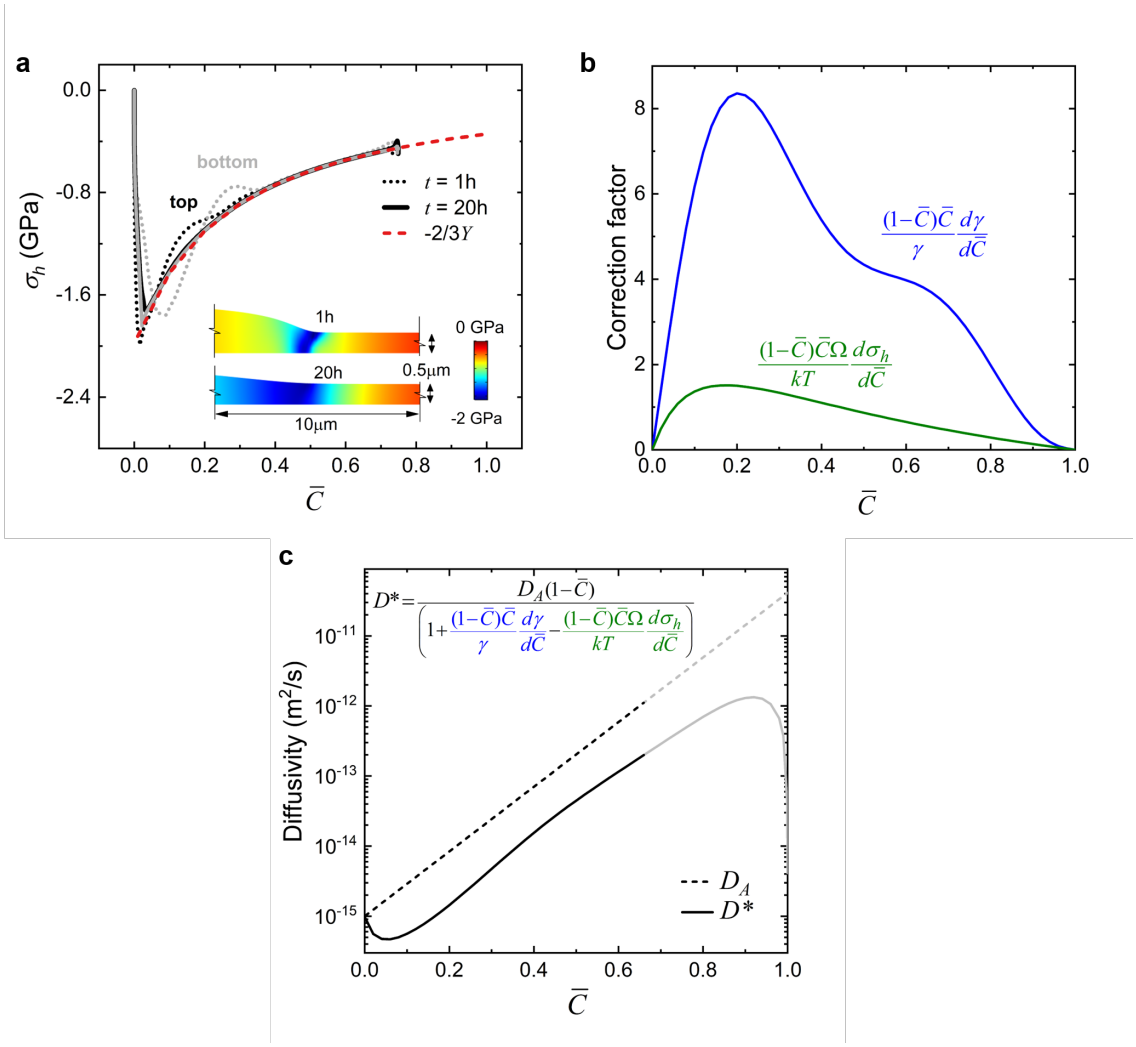

Figure 3.9. : (a) Computational results of the hydrostatic stress on the top and bottom surfaces of a Si thin film at two lithiation times $t = 1$ h and $t = 20$ h. The hydrostatic stress in the plastic regime matches well with 2/3 of the composition-dependent yield stress. (b) Contributions of the chemical (blue line) and mechanical (green line) driving forces in deriving the Li tracer diffusivity. (c) The apparent Li diffusivity and Li tracer diffusivity as a function of the Li concentration.

Figure 3.10(a) shows the resulting Li composition profile of the film after 10 min of lithiation under a constant flux boundary condition. The dashed black line corresponds to the model employing the apparent diffusivity D_A under Fick's law

($J = D_A \frac{d\bar{C}}{dx}$). This profile must overlap with that of the model using the tracer diffusivity D^* under two-way coupling where the diffusion-induced stress gradients regulate the flux via the diffusion potential, Equation 3.12 (green continuous line). This is verified in Figure 3.10(a) and confirms that simplifications in the derivation of tracer diffusivity were adequate. The same model employing one-way coupling between stress and diffusion (that is, stress term removed from diffusion potential in Equation 3.12), gives the Li composition profile in a hypothetical stress-free scenario (red continuous line, Figure 3.10(a)). Comparing the Li profiles for stress-free condition (red line) and stress-regulated condition (green line), the lithiation front is slightly ahead in the stress-free sample. This can be understood from Figure 3.10(b) for the corresponding compressive hydrostatic stress profile. On the right-hand side of the peak (elastic regime), the stress gradient propels Li forward, while the opposite happens on the left-hand side (plastic regime). The fact that the stress effect is expected to be small in this experimental setup is desirable in terms of characterizing the Li kinetics. That is, measurements are not very sensitive to the assumed constitutive relation. We will show that this is not general, and that the stress effect for a typical spherical particle in a composite electrode can be significant.

Although two-way stress-diffusion coupling is commonly considered in battery modeling studies, these predominantly assume that, for diffusion purposes, the material behaves as an ideal solution [45, 173, 168, 61, 164, 95]. Our analysis shows that this assumption has large implications on the Li kinetics and the that activity coefficient is a strong regulator of the stress effect. Given the large composition changes in electrodes, we expect that accounting for the chemical activity will be generally required for the correct implementation of stress-coupled diffusion models. Therefore, the assumption of an ideal solution should not be granted for stress-coupled models without a thorough analysis

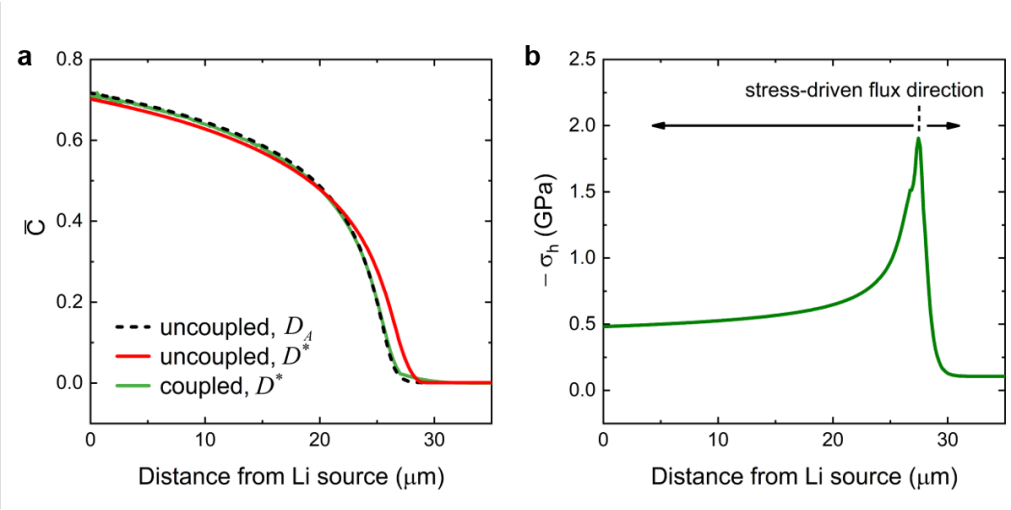

Figure 3.10. : Simulation of the Si film lithiation under a constant flux boundary condition. (a) The Li profile for the model employing the tracer diffusivity D^* and two-way stress-diffusion coupling (green continuous line) reconciles with the Fick's law behavior using the apparent diffusivity D_A (black dashed line). The comparison to a hypothetical stress-free condition (red continuous line) shows that the stress gradient slightly slows down the lithiation front. (b) The compressive hydrostatic stress profile in the film peaks at the lithiation front, driving Li flux forward in the elastic regime ahead on the front, and backward in the plastic regime behind the front.

Stress effect on the Li redistribution upon Li source removal

We design another test to further examine the intimate coupling between the stress and Li transport. In this test, after some degree lithiation, the film is isolated from the Li metal and the spontaneous redistribution of Li in the sample is monitored in the absence of the Li source. In order separate the film from the lithium metal completely, we scratch the film end-to-end across the width direction (transverse to the lithiation direction), separating the lithiated film from contacting with the Li metal. The sample surface is cleaned with a cotton swab to remove the scratch debris. We conduct the same spatial scanning of the film topography on both sides of

the scratch using nanoindentation and determine the Li profiles in the two sections. Figure 3.11(a) shows the resulting Li redistribution over the course of 67 days following the scratch. The left y-axis shows the film thickness, while the right y-axis shows the corresponding Li concentration using the linear relationship between the film volume and Li concentration. The x-axis is the distance from the edge of the scratch. The left side of the film which is still in contact with the Li metal quickly saturates, reaching the equilibrium Li concentration $\bar{C}_S \sim 0.8$ which is consistent with the computational result in Figure 3.7(a). In comparison, the Li profile in the film on the right side of the scratch (separated from the Li metal) slowly evolves. The sharp spikes in the thickness profile due to the fabricated scratch and the naturally formed whiskers are displayed in a lighter color (dashed line) and they are excluded from the data analysis. Another note is that during the cleaning some whiskers are knocked off, leaving behind holes of roughly the same diameter. Hence, it seems that the original blisters formed in the deposition process (from which the whiskers grow) are likely hollow inside. Back to the general feature of the Li profile during the self-redistribution, a clear kink forms at the original site of the moving lithiation front. This feature cannot be explained by the concentration gradient of Li which by itself would cause a self-similar Li profile over time. The kink at the lithiation front when Li starts redistributing is a characteristic of the stress-regulated Li diffusion.

To quantitatively understand the role of stress, we conduct numerical modeling of Li redistribution in the film using the stress-coupled formulation described in Section 3.3. The model geometry is equivalent to the sample geometry. The same constitutive law and material parameters in Figure 3.9 are used here for the modeling. To focus on the effect of the biaxial stress state in the thin film and eliminate the effect of deformation non-linearity, we simplify the boundary condition by applying a symmetric condition at the top and bottom surfaces of the film while allowing the in-plane expansion. This simulation condition imposes a biaxial stress state in the film and greatly improves the numerical convergence. The deformation gradient in the longitudinal direction is eliminated in the diffusion equation which mimics the constraint

by the substrate to the in-plane deformation of the film. The film is lithiated for a certain time by applying an increasing flux at one end, which is subsequently halted to simulate the scratch of the film and separation from the Li source in the experiment. The concentration redistribution following the separation is monitored. The goal of this modeling is not to replicate the long-time scale and the relatively large size in the experiments, but it is to demonstrate how the mechanical stress modulates Li transport in the thin film. Hence, the time scale in the computation is much shorter than that of the experiment.

Figure 3.11(b) shows the hydrostatic stress in the longitudinal direction of the film along which the Li front propagates, and Figure 3.11(c) shows the Li concentration profiles. The different curves denote the time evolution of the stress and concentration profiles after the removal of the influx boundary condition at $t = 0$ min. Regarding the hydrostatic stress field, two features are noteworthy. First, at any given time, for instance in the stress profile at $t = 0$ min (grey curve, Figure 3.11(b)), there is a peak in the compressive stress near the reaction front (indicated by the dashed pink circle) marking the transition between the elastic and plastic regimes. This local stress field causes major stress gradient near the lithiation front over a range of a couple of micrometers. The second factor is the time evolution of the hydrostatic stress in the initially lithiated regime (behind the lithiation front). The compressive stress in the regime near the scratch eventually switches to a tensile stress (the change is indicated by the pink arrow, Figure 3.11(b)) when the lithiation front advances. This is because the Li extraction from the originally lithiated region causes elastic unloading of the stress followed by plastic yielding of the film with a tensile biaxial stress state. The evolution of the stress field in a thin film during the lithiation and delithiation cycle was analyzed in our earlier work [185]. The simulated Li profiles in Figure 3.11(c) display the same features as observed in the experiments – the Li concentration in the lithiated region gradually decreases over time, Li slowly proceeds to the unreacted region of the film, and more importantly, a concave curvature in the Li profile forms nearby the lithiation front (indicated by the pink dashed circle). This curvature forms

because the tensile stress developed in the region undergoing delithiation raises the mechanical factor in the diffusion potential that counteracts the chemical driving force from the concentration gradient and acts against the forward Li flux. For comparison, Figure 3.11(d) shows the Li profile upon self-redistribution if the stress term is not included in the diffusion potential. Without the stress regulation, the Li distribution maintains the self-similarity in the profile and the kink observed in the experiments is absent.

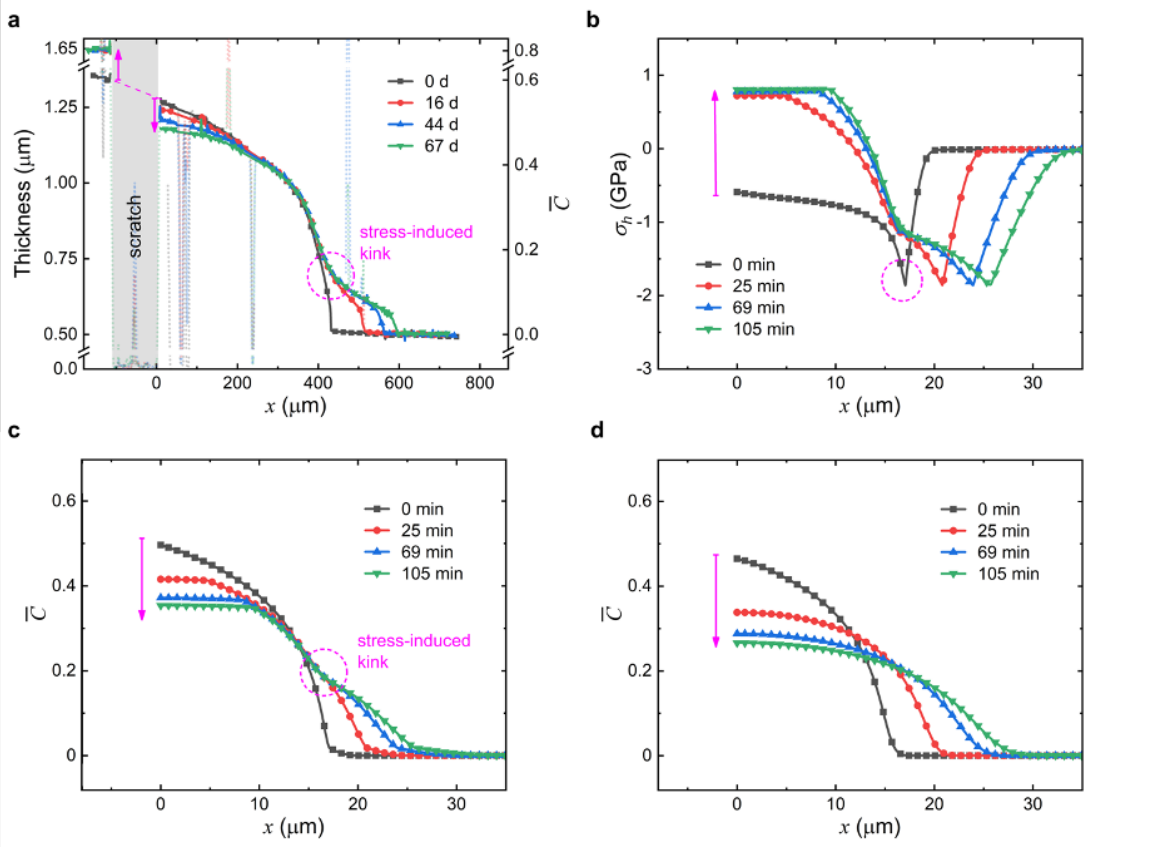

Figure 3.11. : (a) Experimental results of Li redistribution in Si in the absence of Li influx for over two months. The scratch separates a section of the Si film from the Li metal. The kink in the Li profiles is a characteristic of the stress-regulated Li diffusion. The dashed lines denote material defects in the film. (b) Simulation results of the hydrostatic stress along the Li propagation direction at different times. A drastic change of stress is incurred at the moving lithiation front. (c) and (d) show the simulation results of Li profiles with and without considering the stress effect on Li diffusion, respectively. The self-similarity of the Li profile in (d) is broken because of the Li redistribution (delithiation in the initially lithiated regime and lithiation in the pristine regime) which changes the stress profile over time in (b). The dynamics of mechanical stresses regulate Li flux and induces the kink in Li distribution.

Uncertainty of experiments due to surface diffusion

It is important to recognize the size effect on the diffusion kinetics in the experiments given that the initial film thickness is only 500 nm. The influence of preferential diffusion along a boundary was considered by L. G. Harrison (Harrison, 1961). It is expected that after a sufficiently long time the macroscopic behavior of the diffusive species will obey Fick's law. The measured diffusivity D is a combination of the diffusion coefficients of the bulk D_B and of the surface D_S, $D = fD_S+(1-f)D_B$ [4], where f is the ratio between the surface diffusion volume and the total volume. Taking the surface diffusion domain to be several interatomic spacings ($0.5 \sim 5$ Å in Si) thick [47], and knowing that the film thickness is initially 500 nm, $f = 10^{-2} \sim 10^{-3}$ for $0.5/500 < f < 5/500$. In this calculation, the measured diffusivity will be on the same order of magnitude of the bulk diffusivity if $D_S/D_B < 10^4$. For even larger ratios of D_S/D_B, the nanoindentation measurements can result in an overestimation of the bulk diffusivity. For easier visualization, Figure 3.12(a) shows the D/D_B (left y-axis) and $D/(fD_S)$ (right y-axis) as a function of D_S/D_B . The D/D_Bvalues within the upper bound $f = 0.01$ and the lower bound $f = 0.001$ are shown in the shaded areas. A previous work using density-functional-theory based molecular dynamics simulations showed that the surface diffusivity of Li is only a couple of factors higher than its bulk diffusivity in a-Si [26], which would have a close-to-zero effect in our experiment. Figure 3.12(b) gives a survey of Li diffusivity comparing the current work (black line) with existing literature reports of Li diffusivity in a-Si as a function of the Li composition. The experimental results are indicated by the red symbols [39, 136, 165, 178] and the theoretical modeling by green symbols [18, 26, 64, 109, 137, 156]. There is a vast variation among the literature reports, spanning over 8 orders of magnitude, especially among theoretical models. The variation in the experiments may be partially due to the difference of the material states/properties/defects which are dependent on the synthesis process, and partially by experimental uncertainties. For instance, the diffusivity measurements in amorphous Si using the conventional PITT versus

EIS analysis deviated significantly because of various sources of errors such as the unavoidable side reactions at the interface between the electrode and the electrolyte, ambiguity in choosing the diffusion equilibrium potential at a given material composition, the inaccurate measurement of the surface area, material degradation during electrochemical cycles and electrolyte infiltration into a cracked surface [165].

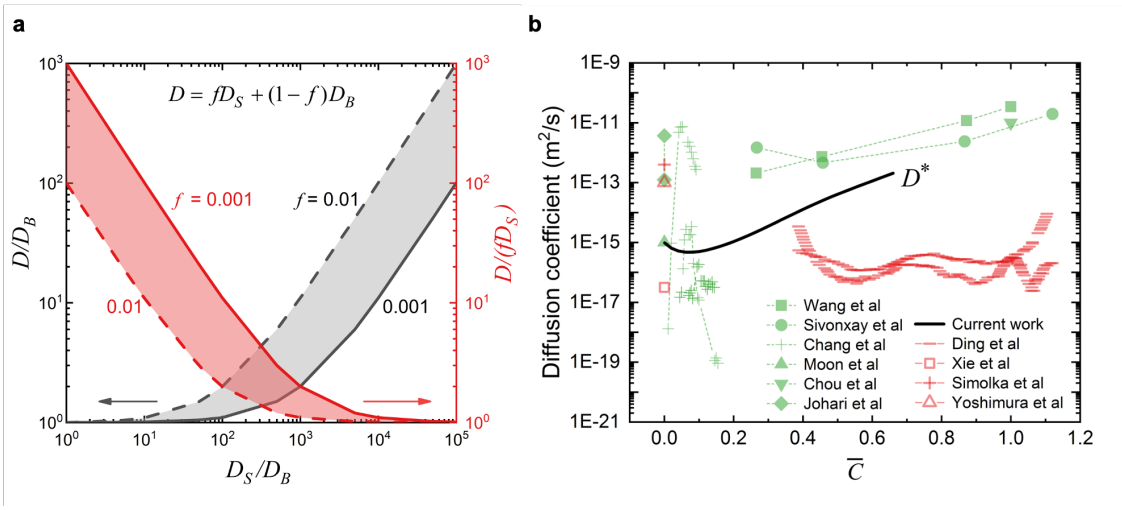

Figure 3.12. : (a) Uncertainty of the measured Li diffusivity in terms of the ratio between the surface and bulk diffusivities and the fraction of the surface-dominated diffusion. (b) Survey of the composition-dependent Li diffusivity in a-Si. The red symbols represent the experimental measurements. The green symbols are theoretical calculations. The black line denotes the current work.

3.6.3 Implication on the battery performance

The deliverable capacity, cyclic efficiency, and rate capability of Li-ion batteries is largely dictated by diffusion in the electrodes. Although it is expected that the diffusion coefficient of Li in the host is altered when the material composition evolves upon Li reactions, its implication on the battery performance is unclear. Here, a simple model of a spherical a-Si particle is used to illustrate the impact of the composition-dependent Li diffusivity on the asymmetric rate performance, Li

trapping, and asymmetric accessible capacity of Si in the lithiation and delithiation cycle.

The Li insertion and extraction are modeled using the theory of coupled diffusion and stress described earlier, and the material properties (tracer diffusivity, elastic modulus, yield stress) from the nanoindentation experiments. The first set of simulations compares the difference between the particle during lithiation versus delithiation for a constant diffusion potential applied at outer surface of the particle (potentiostatic charging). Figures 3.13(a) and 3.13(b) show the Li distribution along the radial direction at different times of Li insertion and extraction, respectively. The time scale is normalized by the characteristic diffusion time $R_0^2/D_{\min}$ and the radial position is normalized by R_0, where R_0 represents the initial radius of the particle. The dimensionless results are independent on the model size and the computation time.

Figure 3.13(a) shows that lithiation of the a-Si particle proceeds through the movement of a relatively sharp concentration gradient. In comparison, delithiation in Figure 3.13(b) shows is a smooth and more homogeneous Li profile over time. This contrast is a consequence of the diffusion coefficient increasing with Li concentration. Similar to the thin film lithiation in the experiments, the steep concentration gradient in the particle lithiation is a result of the lower diffusivity of the pure Si core acting as a bottleneck for Li flux, which leads to the Li accumulation at the lithiation front, Figure 3.13(a). During delithiation, Li diffusion is faster in the Li-rich inner core than the Li-depleted outer shell, leading to a relatively homogeneous delithiation of the bulk, Figure 3.13(b). Figure 3.14 shows the Li profiles in lithiation and delithiation of the Si particle when the stress effect on Li diffusion is not considered. The distinction in the "moving front" versus "smooth Li gradient" behaviors in lithiation versus delithiation is more apparent in this case. The distinct lithiation and delithiation behaviors in the a-Si particle corroborates the in-situ TEM observations [100] as reproduced in the inset of Figure 3.13(c).

It is also noted that the Li concentration at the outer surface of the particle ($\bar{R} = 1$) in Figure 3.13(a) is not constant because the evolving stress field is continuously altering the equilibrium composition under the constant diffusion potential. This can be better understood by Figure 3.14, which shows (a) the radial distribution of Li concentration (red line, left axis) and the hydrostatic stress (blue line y-axis) at the end of the potentiostatic charging, and the corresponding (b) diffusion (black dashed line), chemical (red line) and mechanical (blue line) potentials. The potentiostatic charging ends once the diffusion potential everywhere inside the particle is equal to the applied potential at the outer surface, $\bar{R}$=1. Figure 3.14(b) shows that, at the end of the lithiation, although the concentration is not constant across the particle, the combination of the mechanical and chemical potentials yield a constant diffusion potential across the radius.

Figure 3.13(c) demonstrates another consequence of the faster diffusion at high concentrations, which is that lithiation (black line) completes faster than delithiation (red line) in Si. In fact, during delithiation, even after 10 times longer the time required for full lithiation, there is still over 5% of "trapped" Li inside the particle. This result seems to explain the TEM observation that delithiation is considerably slower than lithiation (bottom versus top rows in the inset panel) and that volume recovery is not accomplished even after long delithiation times. Indeed, Li trapping is now a recognized problem in Si electrodes [63, 89]. Initially, the accumulated capacity loss in Si electrodes was solely attributed to fracture and solid electrolyte interphase (SEI) reconstruction effects [21]; however, recent studies have determined that the capacity loss is present even without those effects [89, 129, 189]. A recent study [189] demonstrated that the columbic efficiency of Si electrodes can be improved via isovalent isomorphism which reduces the energy barrier for diffusion and consequently reduces Li trapping. Our findings explain the underlying mechanism behind the Li trapping effect in Si electrodes.

The second set of simulations is equivalent to galvanostatic (dis)charging (i.e., constant Li flux at the particle surface). Figure 3.13(d) shows the increasing asymmetry

of the lithiation and delithiation capacities when the particle is cycled at different rates. The inset sketch illustrates the source of the asymmetry. During Li insertion, the diffusivity is higher in the Li-rich outer shell, enabling a large Li influx and mitigating the rapid saturation of the surface. In comparison, upon Li extraction, the diffusivity is lower in the Li-poor outer shell, limiting the outflux, and consequently, Li is quickly depleted at the outer surface. The phenomena of Li reactions in Si are intricate. Another interesting observation in literature is that the steep concentration gradient at the lithiation front was only clearly observed during the first cycle, while the Li distribution in the following insertion cycles appeared smoother [100, 103]. A plausible explanation for this behavior is that, since Li diffusivity increases substantially with the Li content, if Li is trapped in Si particles after the first delithiation, the lower-bound of diffusivity in the subsequent cycles would be higher than that in the initial cycle which effectively flattens the concentration profile. The prior experimental result [103] is in support of this hypothesis that Li trapping is a precursor for the change of behavior from the first to subsequent cycles. In this report, the diffusivity was found to increase with Li concentration in the first cycle, but was higher and roughly remained constant in the subsequent cycle. Another factor to consider is that the irreversible volume of Si upon Li cycles observed in experiments may be attributed to the creation of the atomic free volume during delithiation [13, 87], which could also significantly alter the transport properties.

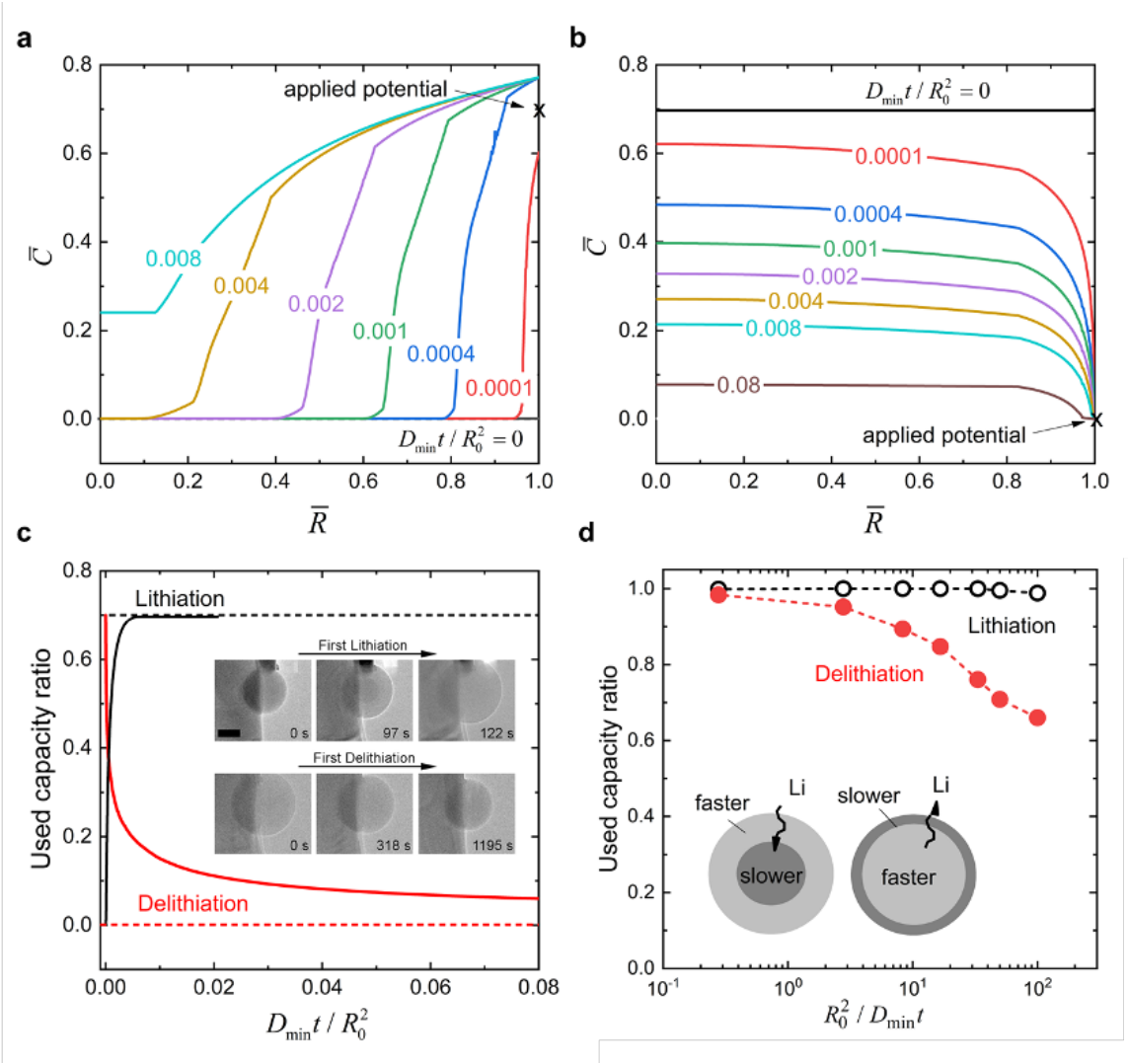

Figure 3.13. : Impact of the composition-dependent Li diffusivity on the asymmetric rate performance and accessible capacity during lithiation versus delithiation of a Si particle. (a) Propagation of a relatively sharp interface during lithiation of the amorphous Si particle. Different lines show the Li profiles at different normalized times until the completion of Li insertion. (b) Delithiation takes place with a rather smooth concentration gradient profile. (c) The accessible capacity is larger for lithiation than for delithiation of Si. Lithiation takes place at a much higher rate than delithiation. This asymmetric behavior agrees well with previous experimental observation [100] shown in the inset of (c). The modeling in (a)-(c) is performed for the particle subject to a constant chemical potential on the outer surface (potentiostatic charging). (d) The asymmetric accessible capacity of Si in lithiation and delithiation at different charging rates when the particle is subject to a constant flux boundary condition (galvanostatic charging).

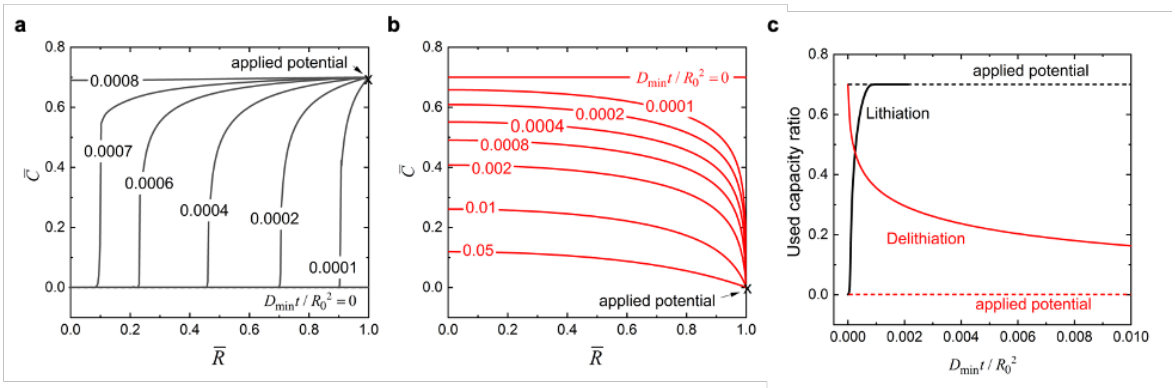

Figure 3.14. : Lithiation and delithiation of a Si particle without considering the stress effect on Li diffusion. (a) Propagation of a sharp reaction front in Si during lithiation, (b) a rather smooth Li concentration gradient during delithiation, and (c) the asymmetric charging (lithiation) and discharging (delithiation) capacities of the Si particle undergoing the potentiostatic cycle.

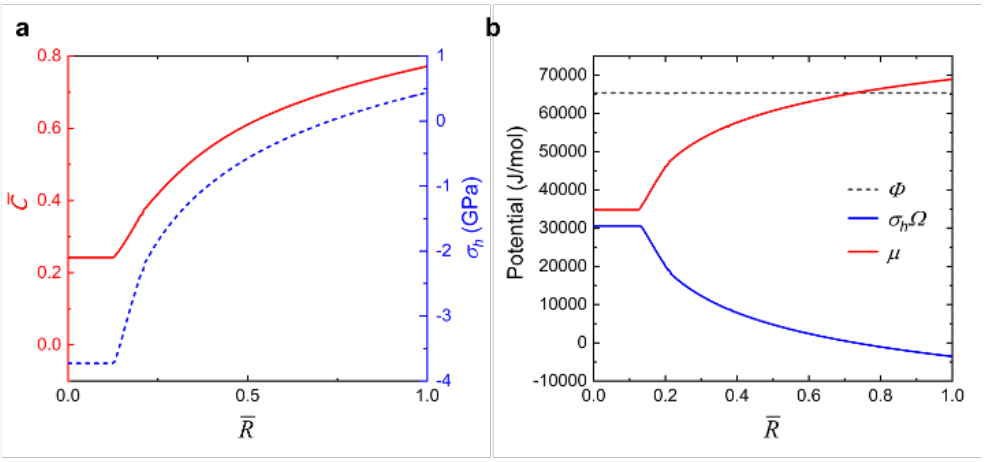

Figure 3.15. : (a) Equilibrium profiles of Li distribution and hydrostatic stress in the Si particle at the end of the potentiostatic charging. (b) Plots of the diffusion potential (dashed line) and its mechanical (blue solid line), and chemical (red dolis line) components across the radius of the Si particle.

3.7 Conclusion

Operando indentation provides an unprecedented capability to measure the real-time evolution of the mechanical properties of redox active materials during the exercise of charging and discharging. This paper demonstrates an inverse use of this experimental platform – the characterization of the Li reaction kinetics in Li-ion batteries through the mechanical determination of the compositional spatiodynamics. Nanoindentation experiments are performed to probe the local Li composition throughout the material using the functional dependence of the mechanical properties and material topography on the material composition. The experiment is conducted by instrumented nanoindentation in a controlled inert gas environment, allowing the slow process of diffusion to be probed over extended periods. Results show that Li diffusivity in a-Si increases over three orders of magnitude from the pristine state to the fully lithiated state. This highly composition-dependent diffusivity creates an asymmetry on the rate performance and accessible capacity of batteries during lithiation versus delithiation. Lithiation of a-Si is fast and proceeds via a steep concentration gradient which generates a moving lithiation front between the lithiated and pristine Si, while delithiation is slow and displays a smooth and homogeneous Li profile. The experiments are further understood by theoretical modeling using the material parameters determined by the nanoindentation experiments and the coupled theory of large deformation and diffusion. A quantitative assessment of the stress regulation on Li diffusion is a focused interest of this work. In the model system of the a-Si thin film, the mechanical driving force for Li diffusion due to the hydrostatic stress is less significant than the effect of the solution non-ideality. Models assuming an ideal solution of lithiated Si would drastically overestimate the stress effect on the Li flux and equilibrium concentration. To demonstrate the characteristic of the stress-modulated Li transport in the film, another test is designed to induce Li self-redistribution, altering the stress fields and consequently breaking the self-similarity of Li profile evolution. The simple geometry of the thin film enables the evaluation of

the mechanical bias to the chemical potential of Li in a quantitative manner. Overall, this study highlights the need for experimental tools to probe the Li concentration and measure the local and evolving material properties in the course of Li reactions. It also offers a new understanding of the lithiation kinetics in batteries from the mechanics perspective, and demonstrates the capability of operando nanoindentation in informing the material chemistry and aiding battery research beyond the mechanical measurement.

4. MECHANICAL PROPERTIES OF WET COMPOSITE ELECTRODES

This chapter is adapted from [32].

4.1 Introduction

Mechanical issues are an overwhelming problem in electrodes of intrinsically large volumetric expansion such as conversion- and insertion-type anodes [120, 42]. Limited success has been achieved to mitigate their mechanical failure upon Li reactions. For cathode materials that undergo a much less obvious volumetric strain (≈5%), structural degradation is less recognized. In recent years, experiments have shown that the state-of-the-art cathode materials such as lithium nickel manganese cobalt oxides (NMC) experience significant intergranular and intragranular failure [174, 105]. Intragranular failure normally takes place in abusive operating conditions such as high temperature and high voltage, where oxygen release and extra Li insertion amplify the internal strain within the grain. Intergranular fracture is the cause of structural disintegration of NMC secondary particles. As-synthesized NMC materials are often in the form of "meatball' secondary particles composed of an agglomerate of smaller and anisotropic primary particles. This hierarchical structure is vulnerable to intergranular fracture because the weakly bonded interface cannot sustain internal stresses developed from the anisotropic expansion of the primary particles [141, 138].

The scanning electron microscopy (SEM) images in Figure 4.1 shows the surface of a polished electrode composed of $LiNi_{0.8}Mn_{0.1}Co_{0.1}O_2$ (NMC 811) active particles, and a conductive matrix (mixture of carboxymethyl cellulose binder and carbon black) in (a) the pristine state and (b) after the first delithiation. This structural decohesion of the particles and eventual disintegration contribute to the increase of impedance of NMC cathodes [81] and loss of capacity [167] over cycles.

The mechanical behavior of the inactive materials also plays a role in the electrochemical performance of electrodes. For instance, stiff binders can help contain excessive deformation of active materials during (de)lithiation, maintaining better contact with the conductive matrix and preventing pulverized active particles from disintegrating [17, 25]. At the same time, mechanical confinement promotes higher mechanical stresses within the active materials, lowering the accessible capacity][168, 101]. In addition, stiffer binders such as the carboxymethyl cellulose in Figure 4.1, can lead to severe cracking of the conductive matrix and promote interface fracture depending on the binder/particle contact geometry [114, 62].

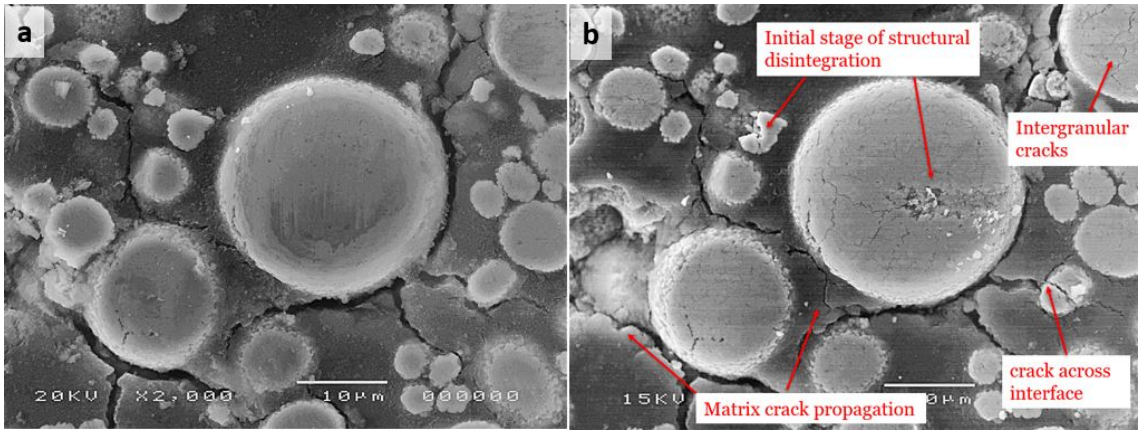

Figure 4.1. : Mechanical degradation in a NMC811 electrode after the first full delithiation.

The knowledge about the mechanical behavior of electrodes is crucial in understanding the degradation mechanism and in the design of materials of enhanced mechanical reliability. However, mechanical characterization of composite electrodes in-situ has been a great challenge. The mechanical measurements performed ex-situ and without environmental control may substantially deviate from the electrochemical conditions in real batteries. A few recent noteworthy papers reported the effect of the liquid environment. Wang et al. [155] found that the mechanical response of Si electrodes is dominated by the polyvinylidene fluoride (PVDF) binder and is

highly sensitive to the electrolyte solution. Wendt et al. [158] observed that even the customary washing of electrodes using dimethyl carbonate (DMC) solvent can significantly affect measurements because of the large amount of solvent absorbed by the PVDF binder. The studies on the macroscopic behavior of electrodes in liquid electrolyte are valuable. Nevertheless, it is worth noting that electrodes in commercial batteries are highly heterogeneous. First, the mechanical properties of the active particles, polymeric binders, and porous conductive matrix are vastly different. Second, the stress field, Li concentration, and mechanical failure are strongly dependent on the local details of the microstructure of electrodes. Hence, the global response of composite electrodes is insufficient to unravel their intricate microstructural features and to understand the evolving nature of material states and stress field upon Li reactions.

In this work, the experimental platform validated in Section 2 is used to measure the mechanical behavior of individual phases in a commercial $LiNi_{0.5}Mn_{0.3}Co_{0.2}O_2$ (NMC 532) electrode. We focus on the understanding of the mechanical properties of the constituents in dry and electrolyte wet conditions, Figure 4.2. We compare the influence of the electrolyte solution on NMC particles as well as sintered NMC pellets. For the first time, we show that the electrolyte plays an role in the fracture strength of NMC secondary particles. The increase in interfacial strength may be a result of the additional capillary force between primary particles. Furthermore, we perform experiments to investigate the influence of electrolyte soaking on the elastic modulus, hardness, and volume change of the conductive matrix with different degrees of porosity. Results offer mechanistic understanding of the complex behavior in composite electrodes and will feed the parametric input of chemomechanical models.

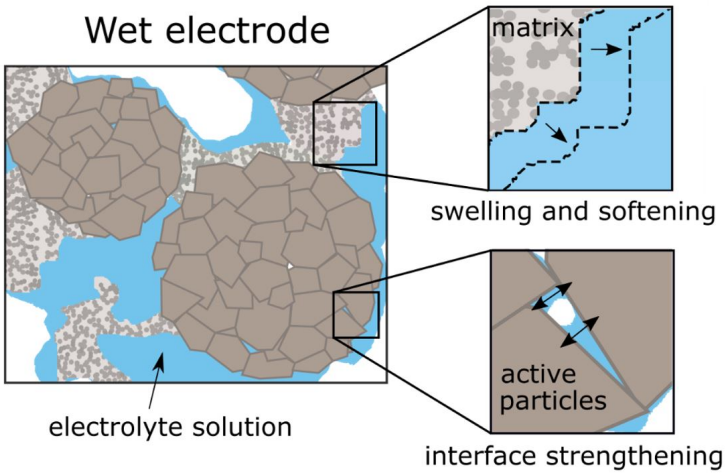

Figure 4.2. : Illustration of the effect of the liquid electrolyte on the mechanical response of the different materials in a composite electrode. Compared to the dry state, the wet polymeric matrix swells in the volume and softens, while the interfacial strength between primary NMC particles is enhanced.

4.2 Experimental methods

4.2.1 Preparation of NMC samples

NMC is prepared in two forms: as-received hierarchical particles (small grains) and sintered pellet (large grains). Commercial NMC 532 powder (MTI Co) is used in the preparation of both configurations. To allow indentation testing, a rigid matrix is necessary to hold the NMC particles in place. The matrix must remain mechanically stable in dry versus wet conditions to avoid changes in the mechanical properties of the matrix from being misinterpreted as changes of the particles. The PVDF binder used in commercial batteries is known to soften in the electrolyte and thus it is not suitable as the matrix for indentation tests on wet NMC. Hence, the inert polystyrene (PS) plastic is selected in our experiments. We perform indentation tests on the PS in dry and wet environments to confirm its stability in the electrolyte solution. In the sample preparation, the PS granules are first heated to roughly 245°C on a heat

plate. Next, the as-received NMC 532 powder is lightly pressed onto the PS surface with a glass slide and subsequently left to cool down at ambient temperature. For the NMC pellet, as-received NMC 532 powder is first ball milled into submicron primary particles. The stainless-steel container and milling balls are solely used for NMC powder and are cleaned with acetone and isopropyl alcohol before use. Then, approximately 1g of the milled powder is pressed into a die (13 mm) under an applied compressive load of 5 tons (model 4350, Carvar). The compressed pellet is sintered at 1000 245°C for 10 h with a heating rate of 10°C/min and left in the furnace until cooled. X-ray diffraction (XRD, Panalytical Empyrean Powder X-ray diffractometer) is performed using a diffractometer with Cu K-alpha radiation in a 2θ range of 10-80° at 40 mA and 45 kV. Both configurations, NMC particle in the PS matrix and sintered NMC pellet, are polished for roughly 30 min using 0.05 μm colloidal silica slurry on imperial cloth (LECO Co) and dried overnight in a vacuum oven at 80°C before nanoindentation. According to our previous measurements, this fine polishing procedure is expected to reduce the NMC surface roughness to approximately 4 nm [169].

4.2.2 Preparation of PVDF binders

PVDF powder (HSV900, MTI Co, molecular weight of 600,000) is dissolved in N-Methyl-2-pyrrolidone (NMP) solvent to form a solution containing 6 wt % PVDF. A portion of the mixture is poured into a glass container to prepare for the pure PVDF film, and the remainder of the solution is homogeneously mixed with carbon black (Super P, MTI Co) in a 50:50 weight ratio in another glass container to prepare for the CB/PVDF film. Both containers are dried in a vacuum oven at 80°C for a couple of days. The films are easily peeled off from the containers and the final thicknesses are approximately 45 μm for the PVDF film and 400 μm for the CB/PVDF film. Sample weight and dimensions, including volume expansion in the electrolyte, are probed using a micrometer (1 μm resolution) and a precision balance (0.1 mg resolution).

Measurements are repeated at least three times for each dimension and the average value is used in the estimation of the density and porosity. The resulting densities of the PVDF and CB/PVDF films are 1.43 g/cm^3 and 0.80 g/cm^3, respectively. Three CB/PVDF film samples are compressed with an electric rolling press to achieve the final porosities of 50.8%, 27.5%, and 3.8%, respectively. The porosity is estimated based on the difference between measured volume and theoretical volume, as follows:

$$\varepsilon = \frac{V_m - \frac{w_m}{2}(\frac{1}{\rho_{PVDF}} + \frac{1}{\rho_{CB}})}{V_m} \tag{4.1}$$

where V_m is the measured volume of the sample, w_m is the measured weight of the sample, ρ_{PVDF} is 1.45 g/cm^3, and ρ_{CB} is 1.90 g/cm^3.

4.2.3 Nanoindentation

Nanoindentation (Keysight G200) tests are performed in an argon-filled glovebox. Samples are tested in dry and wet conditions. In wet condition, a stainless-steel coin cell case is used as a container and samples are kept in the electrolyte. All samples are allowed to soak for at least 1 h before indentation tests in 1M $LiPF_6$ in PC electrolyte. The hardness H and elastic modulus E are determined using a Berkovich indenter following the method described in Section 2.3.2. The Poisson ratio of the sample, ν, is assumed 0.3 for NMC and 0.4 for PVDF and CB/PVDF, respectively. The continuously measured contact stiffness S is derived from the in-phase material response to a superimposed oscillating signal during dynamic load (CSM). The indenter is loaded at a constant strain rate of 0.05 s^{-1}, up to the maximum indentation depth (500 nm for NMC and 2000 nm for PVDF and CB/PVDF, respectively). Grid indentations are performed on PVDF and CB/PVDF films with a spacing of 200 μm between each indent. For NMC samples, targeted indentations are conducted at the center of large NMC particles (minimum diameter of 15 μm) to minimize the boundary effects.

The fracture toughness K_c of NMC is measured by nanoindentation with a cube-corner tip. The fracture toughness is calculated following the formula derived by Marshall et al. [98] and Antis et al. [2] for a half-penny crack:

$$K_c = \alpha \frac{E}{H}^{1/2} \frac{P}{c^{3/2}} \tag{4.2}$$

where α is an empirical constant that depends on the indenter geometry (0.036 for cube-corner shape [49]), c is the crack length, and P is the critical load that generates a crack of the length c. A cube-corner indenter is used because its sharp angle (centerline-to-face angle of 35.3°) reduces the load threshold for cracking, enabling the characterization of small volumes of materials such as NMC secondary particles. However, cracks produced at low loads are small and difficult to measure by conventional microscopy techniques. A method proposed by Field et al. [43] allows the estimation of the crack length from the load-displacement curve, which eliminates the need for direct measurement. When a brittle material is indented with a sharp indenter, the load-displacement curve may exhibit sudden bursts in the tip displacement. This sudden tip penetration, so-called pop-in, is thought to be associated with the formation of half-penny cracks extending from the edges of the indenter [43]. The extra tip displacement after the pop-in, h_x, relates to the crack length, c, as follows:

$$c = \sqrt{2} h_m + \left(Q \frac{E'}{H} - \sqrt{2} \right) h_x \tag{4.3}$$

where E' is the plane strain elastic modulus, Q is an empirical constant that depends on the indenter geometry (4.55 for cube-corner [43]), h_m is the measured tip displacement, and $h_x = h_m - h_t$. The theoretical tip displacement in the absence of pop-in, h_t, is estimated by the extrapolation of the load-displacement curve before the pop-in event. E' and H are known from indentation tests with the Berkovich tip.

The intricate microstructure of NMC results in a large variation in the load-displacement curves and ambiguity in the detection of pop-in events. Thus, to avoid subjectivity of interpretation and allow efficient handling of numerous experiments, we write an algorithm to process the pop-in data, identify and discard invalid tests, and compute fracture toughness.

The first step of the algorithm is the identification of the pop-in events. Morris et al. [110] showed that pop-in events are associated with peaks in the reduced stiffness,

$$\overline{S} = \frac{S}{S_1}, \tag{4.4}$$

where S is the continuously measured contact stiffness and S_1 is the instantaneous slope of the loading curve. The inspection of Figure 4.3(a) shows that, with exception of very small tip displacements, a clear correlation exists between the peaks in $\overline{S}$ (continuous red line) and bursts in the load-displacement behavior (continuous blue line). The algorithm needs to be able to distinguish peaks from random noise in the $\overline{S}$ curve in order to correctly identify pop-in events. Considering the irregularity of the load-displacement curve at very shallow depths, which may also include a pop-in due to elasto-plastic transition [133], a minimum tip displacement h_{min} (black arrow) must be assigned as the threshold below which cracking is assumed not taking place. h_{min} =100 nm is chosen. The sensitivity of the results to this parameter is discussed in the Results and Discussion section. Having discarded the reduced stiffness data below h_{min} (continuous grey line), the reduced stiffness data for h above h_{min} (continuous red line) is used to find outliers (pop-ins). Figure 4.3(b) displays the reduced stiffness distribution for the test in Figure 4.3(a) where the 'o' symbols represent individual data points. Any observations above $Q3{+}3IQR$ or below $Q1-3IQR$ are defined as outliers, where $Q1$ is the 25th percentile and $Q3$ is the 75th percentile, and $IQR = Q3 - Q1$. A real pop-in event will always introduce a positive skewness to the distribution, while random noise leads to a symmetric deviation. Therefore, all pop-in events (outliers) are detected above the upper boundary ($Q3 + 3IQR$).

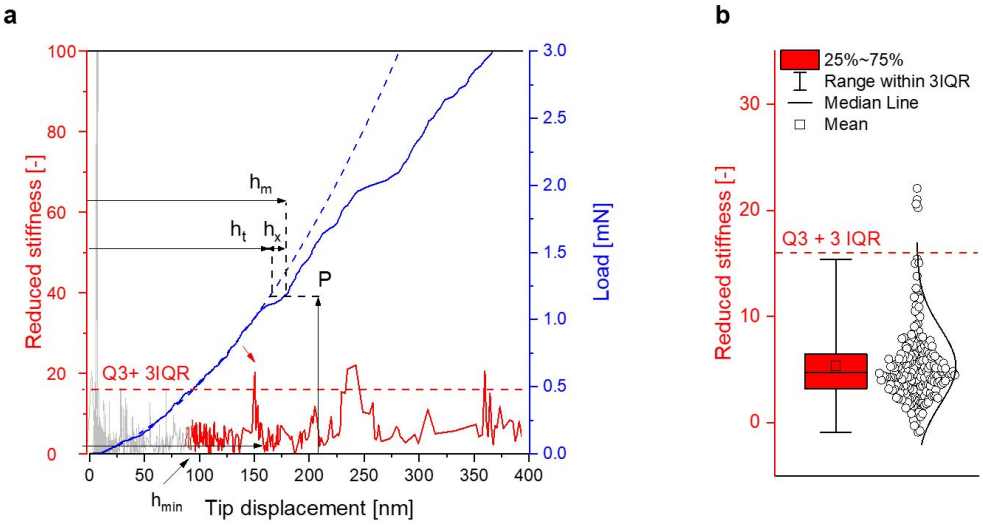

Figure 4.3. : Systematic procedure for the determination of the fracture toughness. (a) Load as a function of indentation depth and (b) corresponding reduced stiffness distribution showing the $Q3 + 3IQR$ threshold used to characterize a pop-in.

With the pop-in events identified, the load-displacement curve before the first pop-in is fitted with a quadratic polynomial function to predict the theoretical tip displacement without crack h_t (dashed blue line, Figure 4.3(a)). The crack length is estimated through Eq. 4.3 using the pop-in length h_x for the first five points after the pop in event. The validity of Eq. 4.3 in the estimation of the crack length for NMC materials was confirmed in our previous work [169]. It is worth noting that the average crack length in our experiments ($\sim$1 µm) is much smaller than the radius of the secondary particles ($\sim$10 µm), thus avoiding crack interaction with the matrix. Finally, K_c is calculated through Eq. 4.2 and the average K_c of the five points is stored. Note that load-displacements curves not are manually selected or removed by the user; only 6% of the total number of tests were automatically discarded by the following criteria: the extrapolated load-displacement curve yields a negative crack length ($h_x < 0$), or no pop-in events are detected.

The operando optical microscopy experiments revealed a new kinetic behavior of NMC electrodes: The first delithiation of pristine NMC particles proceeds through a

large and sudden concentration change in which NMC particles are individually activated in a roughly sequential manner, while the following (dis)charge sequences, at the same C-rate, happen through a gradual and simultaneous (de)lithiation of all viable particles. This appears to be the first report of this behavior to date. This chapter will discuss possible mechanisms behind this phenomenon. Various experiments were conducted to rule out hypotheses that such effect is associated with factors such as the composition of electrolyte and the matrix matrix, and the transition metal ratios. This unusual kinematic behavior persists regardless. It is possible that this slow kinetics of pristine materials leading to a sharp interface could be more general than previously thought. A similar behavior was observed in the lithiation of pristine amorphous silicon [101], and explained in Chapter 3. A better understanding of this particle activation phenomenon could have implications on the design of the ideal formation protocol, and have consequences on long-term performance.

4.3 Results

The individual mechanical properties of PVDF polymeric binder, CB/PVDF conductive matrix, and NMC particles in the 1M $LiPF_6$-PC liquid electrolyte are measured. NMC532 is investigated in the form of secondary particles (small grains) and sintered pellet (large grains). The conductive matrix is examined for different porosities and with and without carbon black filler.

4.3.1 Elastic modulus and hardness of the binder and the conductive matrix

Electrolyte uptake causes a volume strain of roughly 30% in the PVDF film (Figure 4.4(a)). This large volumetric change alters the functionality of the conductive matrix in different aspects. For instance, the increase in the binder volume represents an effective decrease in the volume ratio of the conductive filler (i.e., carbon black), and consequently causes an increase in the electrical resistance of the electrode [22, 71].

For the CB/PVDF composite, the volume expansion depends on the initial porosity. We find that the dense film expands 30% in volume as compared to 15% volume expansion for the porous film (50% porosity). Thus, the increase in the specific volume of the binder in wet condition would occupy pore spaces in the conductive matrix, which could affect the ion transport. It is interesting to note that volume expansion displays an opposite trend to the swelling ratio (weight fraction increase by electrolyte uptake) as reported in literature which increases with the porosity [27]. The thicknesses of pure PVDF and CB/PVDF films (50 and 185-420μm, respectively) were sufficiently large so that the elastic modulus and hardness are approximately constant with different indentation depths (no substrate effect). The elastic modulus of PVDF film in dry condition, 590 MPa (red bar, Figure 4.4(b)), is in good agreement with previous reports by tensile tests (400-650 MPa) [22, 90]. In the wet condition, both the elastic modulus and the hardness of the binder drop by about 50% (blue bar, Figures 4.4(b) and 4.4(c)). This deterioration in the mechanical properties is a result of binder expansion by solvent uptake which facilitates sliding and disentanglement of the polymer chains [23]. The CB filler has a significant impact on the mechanical behavior of the dry matrix - the modulus of the CB/PVDF composite (2.5-2 GPa, Figure 4.4(d)) is about four times that of pure PVDF (0.59 GPa, Figure 4.4(b)). Both modulus and hardness decrease significantly with the porosity, Figures 4.4(d) and 4.4(e), where the nominal porosity represents the initial porosity of the matrix without absorption of liquid. The effect of electrolyte soaking is particularly detrimental to the properties of the conductive matrix (CB/PVDF), resulting in a decrease of over 80 % in both modulus and hardness. In the wet state, the mechanical properties of PVDF and CB/PVDF are roughly the same, indicating that the carbon black loses most of its role in the mechanical response of the composite.

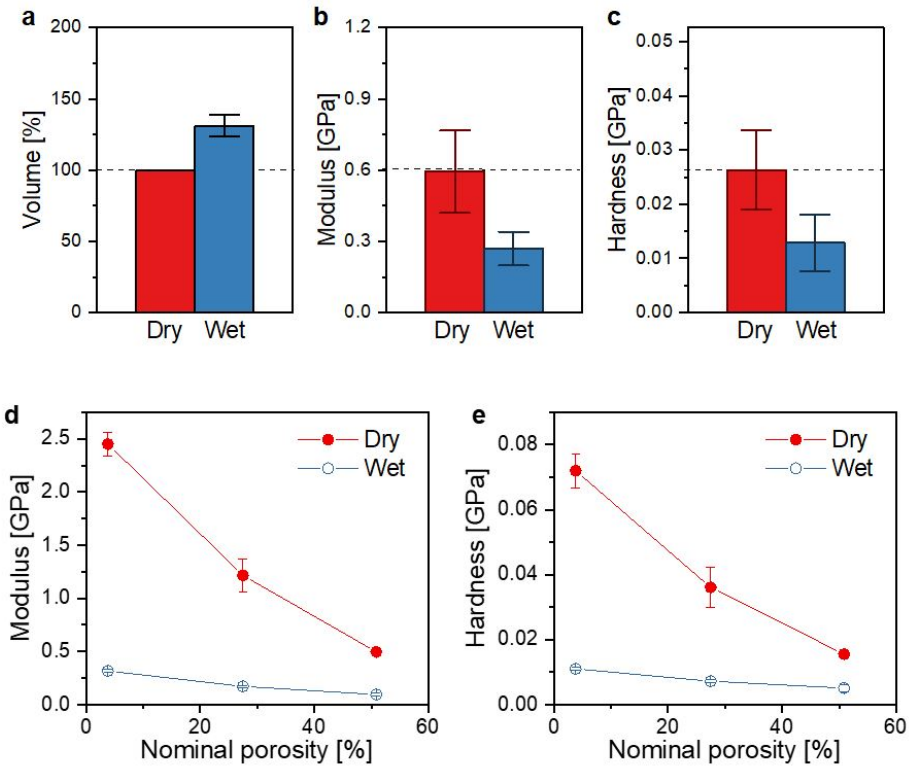

Figure 4.4. : The comparisons of (a) volume, (b) elastic modulus, and (c) hardness of the PVDF binder under dry and wet conditions. (d) Elastic modulus and (e) hardness of the CB/PVDF conductive matrix as a function of the nominal porosity. Dry measurements are shown in red and wet measurements are shown in blue. The error bars represent the standard deviation.

4.3.2 Elastic modulus, hardness, and fracture toughness of NMC secondary particles and pellets

The NMC material is evaluated in two configurations: as-received hierarchical particles (small grains) and sintered pellet (large grains). The final grain size of the pellet (3-10 μm, Figure 4.5(a)) is significantly larger than the size of the primary particles in the as-received NMC sample (0.1-1 μm, Figure 4.5(b)). The XRD profile of the NMC pellet is consistent with the reference pattern [48], confirming that the

elemental composition and crystal structure are maintained during sintering (Figure 4.5(c)).

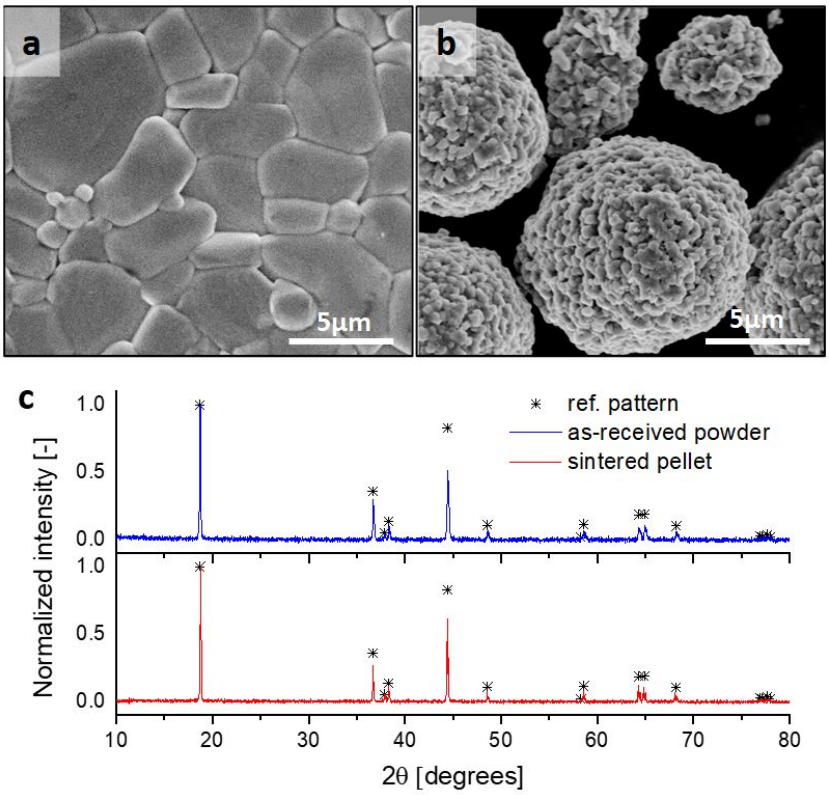

Figure 4.5. : SEM image of the NMC532 (a) sintered pellet and (b) as-received secondary particles. (c) XRD profiles in comparison with the reference pattern [48].

For the hierarchical particles, a PS matrix is used to hold the particles during indentation. Figure 4.6 confirms that the elastic modulus (3.8 GPa) and the hardness (0.25 GPa) of the PS matrix remain unchanged in the presence of the electrolyte, thus attributing the changes in the measured mechanical behavior in dry versus wet environments to the NMC particles alone. Targeted indentations are performed on the polished NMC samples.

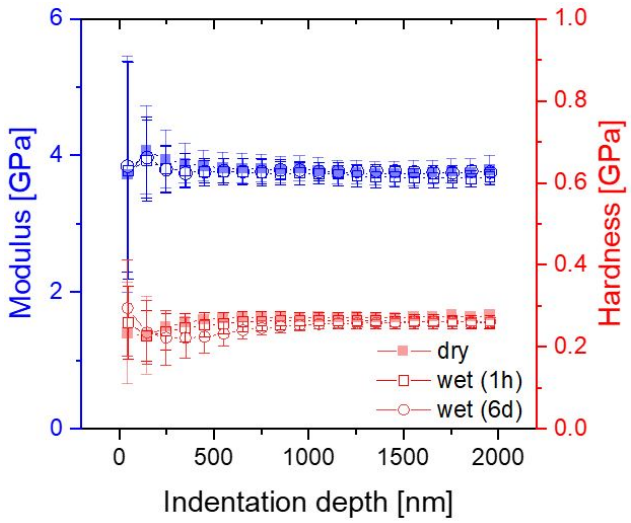

Figure 4.6. : Elastic modulus (blue) and hardness (red) of polystyrene in dry condition (filled square), submerged in 1M $LiPF_6$-PC electrolyte for 1 hour (open square), and submerged in the electrolyte for 6 days (open circle). The error bars represent the standard deviation.

The surface finish, microstructure and indentation sites are shown in Figure 4.7(a) (NMC secondary particles embedded in PS matrix) and in Figure 4.7(b) (sintered NMC pellet). The low resolution of Figure 4.7(a) is partly because of the poor electrical conductivity of the PS matrix. While both samples exhibit a certain degree of porosity, the primary particle size differs significantly. At an appropriate indentation depth, this difference allows probing the mechanical response within a single particle (sintered NMC pellet) and across particle interfaces (as-received NMC powder). The pellet experiment is approximate to the intrinsic properties of NMC in the bulk form, while the measurement of NMC secondary particles is dependent on the packing arrangement of the agglomerate, porosity, and physical interactions between the primary particles.

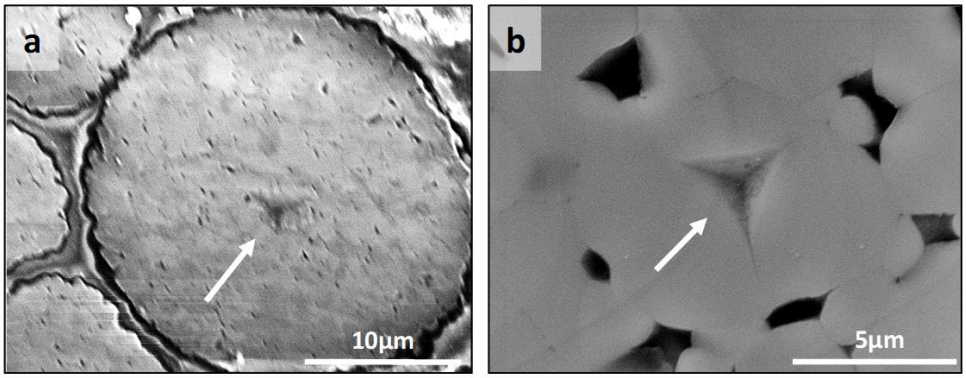

Figure 4.7. : SEM images of the polished NMC agglomerates in a polystyrene matrix (a) and sintered pellet (b). The residual impressions at the pre-selected sites are shown after removal of the indenter.

For elastic modulus and hardness measurements, a minimum of 15 indentations are performed for each configuration. The load-displacement curve and elastic modulus as a function of indentation depth are shown in Figure 4.8. The decrease in modulus with indentation depth is a consequence of two main reasons: (i) the substrate effect, and (ii) deep indentation induced material damage. In an earlier work, we showed that tests on NMC particles are independent on the matrix properties if the indentation site is away from the particle/matrix interface and if the indentation depth is chosen much less than the secondary particle radius (8-10 µm) [169]. Potential crack formation and propagation in a brittle material induced by deep indentation is another reason of the decrease of modulus [127, 41]. The dashed line in Figure 7b indicates the selected indentation depth (85 nm) to minimize material damage. This value represents the lowest indentation depth where the surface roughness is negligible while the area function calibration and surface contact detection remains accurate in our experiments.

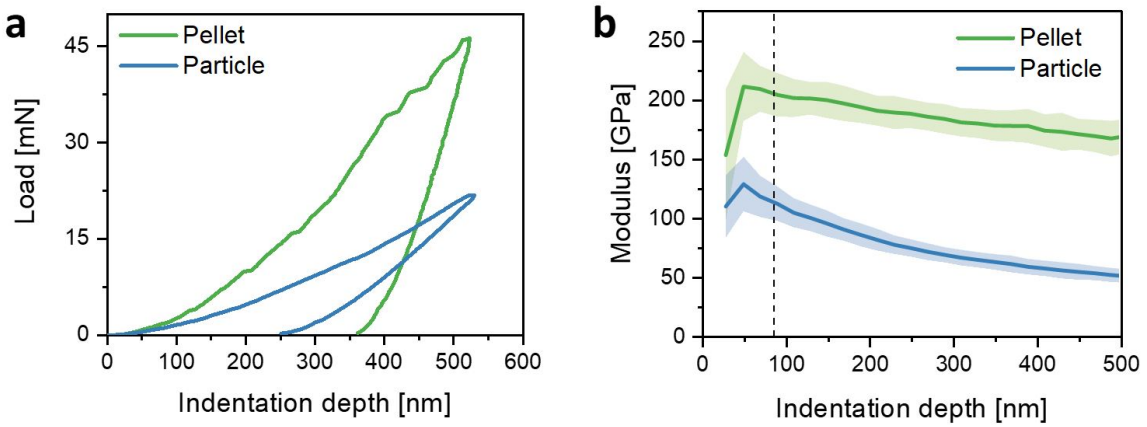

Figure 4.8. : (a) Load-displacement curves and (b) elastic modulus as a function of the indentation depth for NMC particles and pellet. The shaded areas in (b) represent the standard deviation.

Figure 4.9 shows the elastic modulus, hardness and fracture toughness of NMC sintered pellet and secondary particles (NMC agglomerates) in dry (red box) and wet (blue box) conditions. The grey circles represent individual indentations, the box indicates the 25-75% range, the white line is the median, and the average values are shown in the labels and indicated by the white squares. Regardless of the environment effect, the mechanical properties of the agglomerated secondary particles are generally lower than those of sintered pellets. This difference is attributed to the weak interfaces between the primary particles in the NMC agglomerate. Kendall et al. [67] showed that the contact between particles within an agglomerate introduces compliance to the system and results in a lower elastic modulus of the assembly. The modulus of the agglomerate is dependent on the packing ratio, the diameter of the primary particles, and the interfacial energy [67]. Thus, the synthesis procedure of NMC powder, which strongly affects the particle morphology and internal porosity [162, 78], can have significant impact on the mechanical properties of the agglomerate.

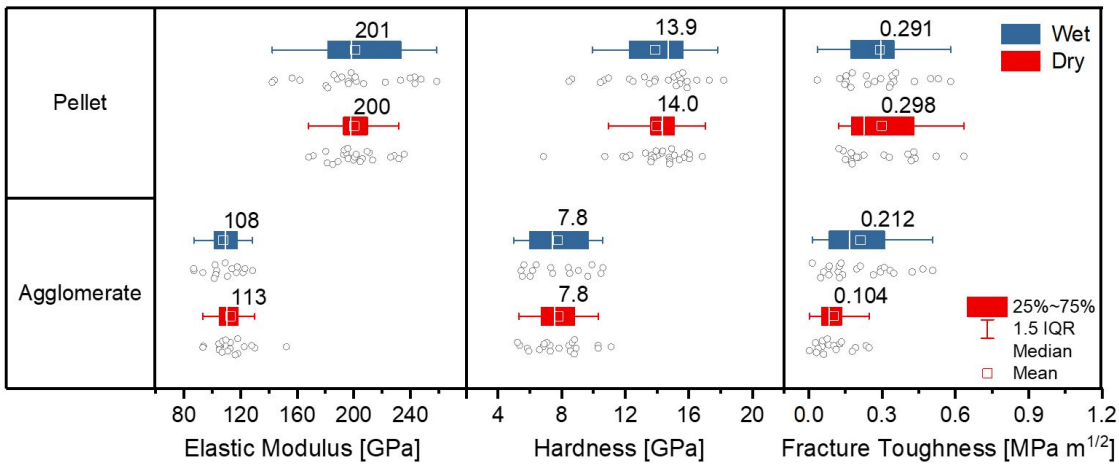

Figure 4.9. : (a) Elastic modulus, (b) hardness, and (c) fracture toughness of NMC agglomerate and sintered pellet in dry (red box) and wet (blue box) environment.

There is no obvious difference between the elastic modulus and hardness of NMC samples in dry versus wet condition. However, while the properties of sintered pellets remain mostly unchanged in the electrolyte, the average fracture toughness of the secondary particles is improved from 0.104 MPa $m^{1/2}$ in the dry condition to 0.212 MPa $m^{1/2}$ in the liquid environment. This difference is statistically significant according to the standard t-test (p-value = 0.007). It is worth noting that for the computation of the fracture toughness, we assumed that the threshold for cracking was h_{min}=100 nm. To test the sensitivity of the calculations to this parameter K_c is also compute for h_{min} =50 nm and h_{min} =150 nm, Figure 4.10. The trend is the same, however, h_{min} =100 nm results in the least number of discarded tests and at the same time, the least spread in the data. These results suggest that crack propagating along the interface of primary particles is influenced by the liquid penetration. Notice that, for the secondary particles, the variation in the data is significantly higher in the wet condition than in the dry state. This variation is not observed for the pellet measurements. The large deviation is likely a result of heterogeneity in liquid saturation rather than random noise in the experiments. It will be interesting to determine what is the physical mechanism behind the increased fracture toughness of wet NMC

agglomerates. The initial expectation was that the liquid electrolyte could act as a lubricant to the NMC agglomerate reducing the inter-particle friction and thus the interlocking forces in the secondary particles. However, the experimental results suggest the opposite effect (i.e., wetting increases the fracture resistance of the particle). To better understand this behavior, the nature of the bonding forces in granules is considered next.

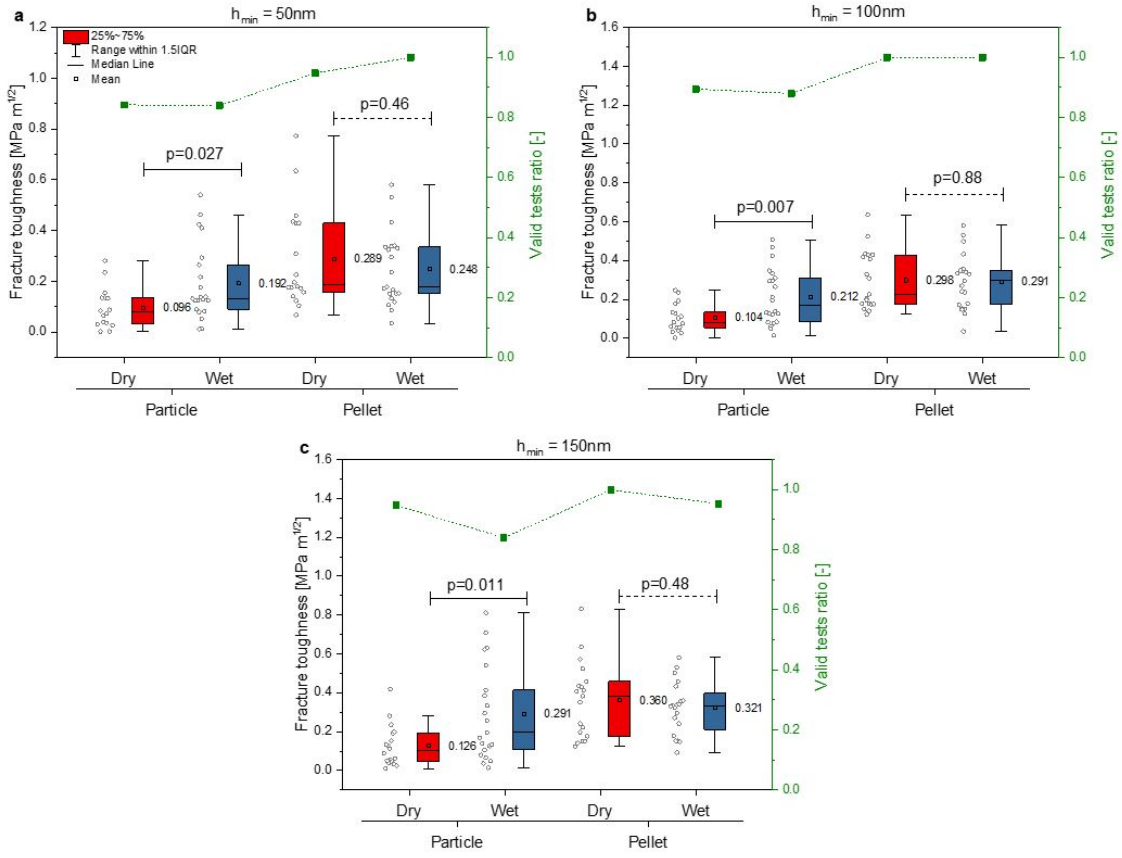

Figure 4.10. : Sensitivity of fracture toughness measurements on user-defined h_{min}. The ratio of valid (kept) number of tests to the total number of tests for each configuration is indicated by the green square symbol (right y-axis).

For granular materials, the strength of an agglomerate is generally governed by interparticle bonding rather than the strength of the individual constituent particles [130]. Rumpf and Schubert [132] considered the adhesion between single particles in-

cluding the following mechanisms: (i) bonds without material bridges (van der Waals, electrostatic, and magnetic forces), and (ii) bonds with material bridges that can be liquid or solid (binding agents, sintering, crystallizing salts). The relative importance of the bonding forces varies case by case. NMC powder is usually synthesized via the two-step process: (i) precursors are fabricated by hydroxide co-precipitation; and (ii) precursors are mixed in appropriate proportions and calcinated [162, 65]. The resulting powder consists of secondary particles in which many primary particles are aggregated, Figure 4.11(a). The characteristic sizes of primary particles, in the range of several hundred nanometers, are sufficiently small such that van der Waals forces can be significant. It is also possible that chemical bonds form along particle boundaries depending on the calcination conditions. Because of the high polydispersity and irregular particle shapes, it is impractical to obtain precise analytical predictions for the strength of the NMC agglomerates. As a first approximation, consider the Rumpf model to represent the tensile strength σ_t of agglomerates composed of spherical particles of a uniform size:

$$\sigma_t = nF = 1.1\frac{1-\varepsilon}{\varepsilon}\frac{1}{D^2}F, \tag{4.5}$$

where n is the average number of interparticle contacts per unit area of the cross-section and F is binding force. This equation is applicable for different bonding mechanisms. Compared to the dry state, the wet agglomerate experiences a negative capillary pressure which absorbs liquid electrolyte into the microchannels between primary particles, Figure 4.11(b). Capillary forces are typically stronger than van der Waals attraction but weaker than the solid bridges, and therefore can potentially impact the strength NMC agglomerates.

Let's consider the hypothesis of the additional capillary force brought by the liquid bridging, by rewriting Eq. 4.5 for capillary binding forces alone [132]:

$$\sigma_t = 6S\frac{1-\varepsilon}{\varepsilon}\frac{\gamma}{Dcos\theta}, \tag{4.6}$$

where S is the liquid saturation, ε is the void fraction, D is the surface average diameter of primary particles, γ is the surface tension, and θ is the liquid-solid contact

angle. The surface tension of the PC solution is 41.1 mN/m [135]. Assuming $\theta = 0$, a saturation value of 0.95, and void fraction of 0.028 [157], Eq. 4.6 predicts a fracture strength of ∼16 MPa for NMC primary particles bonded only by the capillary forces. From linear elastic fracture mechanics: $K_{IC} = \sigma_t\sqrt{\pi a}/Y$. Assuming a half crack length a of 1 μm and a half penny surface crack ($Y = 0.64$), the capillary forces would lead to an increase of 0.044 MPa $m^{1/2}$ in fracture toughness of NMC secondary particles in the liquid electrolyte compared to its dry state. This difference is on the similar order of magnitude as determined in experiments (median difference of 0.085 MPa m_y and average difference of 0.108 MPa $m^{1/2}$). It is worth noting that the analysis is based on an idealized model of spherical primary particles of a uniform size, while the as-synthesized NMC particles are polydisperse and of irregular shapes and previous work has shown that the Rumpf model may largely underestimate the strength of granular materials [67]. Moreover, the true saturation and contact angle may largely differ from the assumed values and the presented calculations are simply meant to inform on whether the capillary forces could be a factor in determining the interfacial strength of the agglomerated particles. Other mechanisms are also possible underpinning the liquid effect. For example, previous work showed that the native oxide SiO_x on Si anodes can react with the decomposition products of $LiPF_5$ (PF_5 or HF in trace amounts in the electrolyte) to form SiO_yF_y at the ambient temperate prior to any electrochemical cycling [114]. Hence, it is possible that, in addition to the liquid bridging, a solid surface layer could be acting as a nano-filler at the interface of primary particles and altering the interfacial strength of the secondary particles.

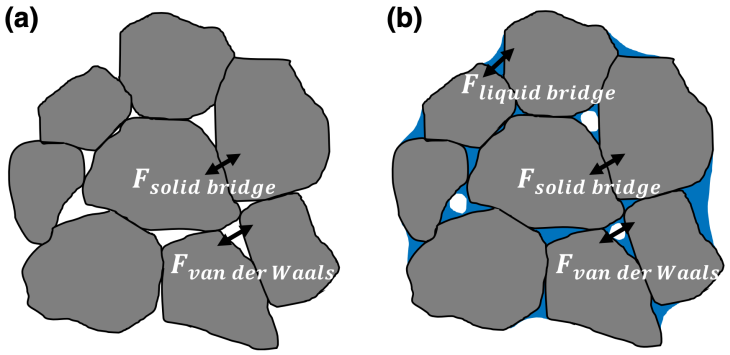

Figure 4.11. : Schematic illustration of physical interactions between the primary particles in (a) dry and (b) wet conditions.

It is worth mentioning that although Figure 4.9 shows the properties of randomly selected primary particles in the NMC pellet, it was clear from the experiments that the particles are highly anisotropic. It is well known that upon polishing a polycrystal, the individual grains appear brighter or darker depending on their orientation. Figure 4.12(a) shows optical image of the polished NMC 532 pellet. The grain colors range from a bright white to dark grey, while the black spots are pores. Figures 4.12(a) and (b) show that the elastic modulus and hardness are significantly lower in the orientation in which grains appear brighter. It is expected that the elastic modulus along the c-axis of the NMC crystal will be lower than along the basal plane due to the weak Van der Waals interactions between the layers. Therefore, it is understood that the brighter grains (lower elastic modulus) are oriented such that the basal plane is approximately parallel to the surface. Conversely, the darker grains (higher elastic modulus) have the basal plane aligned at a larger angle from the surface, which seems reasonable as such configuration intuitively should lead to a rougher polish. It would be interesting to employ a crystallographic characterization technique such as electron backscatter diffraction (EBSD) to formulate the exact relationship between the mechanical response and the crystallographic orientation.

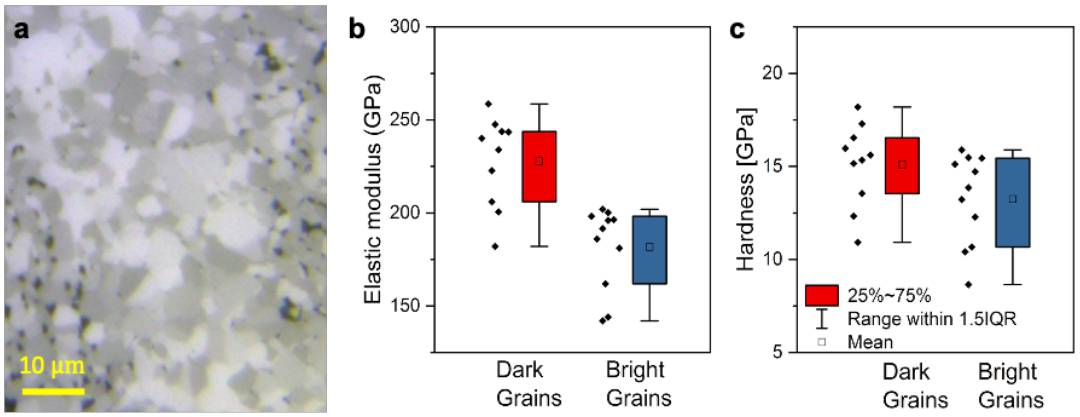

Figure 4.12. : (a) Optical image of the polished NMC532 pellet showing random grain orientations. Distribution of the (a) elastic modulus and the (b) hardness according to the grain brigthness.

4.3.3 Conclusion

In situ nanoindentation was employed to measure the mechanical properties of a PVDF polymeric binder, a CB/PVDF conductive matrix, and NMC active materials in dry and wet conditions. The NMC active material was studied in the form of as-received secondary particles (agglomerate of primary particles) and sintered pellet (large single particles). For both configurations, there is no apparent difference between the elastic modulus and hardness in dry and wet states. The fracture toughness of sintered pellets remains mostly unchanged in both conditions, while the interfacial strength of the secondary particles is largely enhanced when wetted by the electrolyte. These results suggests that crack in an NMC agglomerate propagates along the interfaces between primary particles and is influenced by the liquid saturation. A possible reason for the toughening of the agglomerate is the formation of liquid bridges due to the capillary pressure absorbing electrolyte into the microchannels and nanopores between primary particles, therefore adding an extra interparticle bonding force. The mechanical response of conductive matrix is largely dependent on the porosity and

carbon content in dry condition. When wetted by the electrolyte, the PVDF binder undergoes a volume expansion of up to 30% and a decrease in the elastic modulus and hardness of roughly 50%. The effect of electrolyte soaking is particularly detrimental to the mechanical strength of the conductive matrix (CB/PVDF), which results in a decrease of over 80% in the mechanical properties. Experimental results highlight the significance of the environment on the mechanical behavior of both active materials and conductive agents in composite electrodes.

5. LITHIUM SPATIODYNAMICS IN NMC ELECTRODES

5.1 Introduction

State-of-the-art NMC electrodes experience significant first cycle capacity loss [188]. Recent studies have shown that this loss is mostly a result of kinetic limitations and it can be largely avoided by applying long voltage hold periods [188, 66] or by discharging at high temperatures. One study found that Li distribution in NCA ($LiNi_{0.8}Co_{0.15}Al_{0.05}O_2$) has distinct lithiation versus delithitation dynamics. Other studies found that the Li diffusivity in these materials is highly dependent on the Li concentration and vary by at least a couple of orders of magnitude [150, 175, 188]. Interestingly, recent measurements on NMC particles post-charge found that the local state-of-charge (SOC) varies significantly within the particle (up to ~ 10 % variation) and across multiple particles (up ~ 30 % variation). The authors suggested that this behavior might be associated with the thermodynamic contributions of the stress fields generated from mismatched anisotropic deformations within the particles.

As previously explored in Chapter 3, the characterization of the compositional spatiodynamics of battery materials is difficult due to the low atomic weight of Li, and the complexity and small feature size of the electrode microstructure. For crystalline hosts, a popular approach to track local SOC is through the evolution of the lattice parameters from spatially resolved XRD patterns. The use of this technique has revealed a variety of interesting kinetic behaviors in batteries [88, 86]; however, it generally requires the use of large-scale synchrotron facilities, which are not readily accessible.

This work proposes a practical and inexpensive approach to explore the compositional dynamics of battery materials using operando optical microscopy. Operando optical microscopy tools have been employed in several battery studies [19]. How-

ever, literature reports on composite electrodes have been limited to compositional analysis at the electrode level [50, 142]. Here, this technique is applied at high magnification (spatial resolution $\sim 1\mu m$) via surface preparation of the electrode. This enables studying the composition spatiodynamics at the particle level through observed changes in brightness at different SOCs.

We perform continuous optical measurement of the polished surface of NMC electrodes during cycling inside a fluid cell. The experiments reveal a new kinetic behavior of NMC electrodes. The first delithiation of pristine NMC happens through localized, sudden changes in concentration, where individual particles charge seemingly randomly and asynchronously. Additional tests show that this effect is not conditional on the composition of the electrolyte, the matrix, or the transition metal ratio. This behavior is distinct from the homogeneous and gradual (de)lithiation in subsequent (dis)charge sequences. Possible mechanisms regulating this heterogeneous composition dynamics during the first delithiation are discussed.

5.2 Experimental methods

5.2.1 Sample preparation

We test three different cell configurations to assess the role of different aspects of the electrode composition and preparation process on the experimental findings. The electrode consists of as-received NMC powder (MTI Co.), carbon black (CB, Super P, MTI Co.), and a binder. We test two NMC and binder compositions: $LiNi_{0.8}Mn_{0.1}Co_{0.1}O_2$ (NMC811) and $LiNi_{0.5}Mn_{0.3}Co_{0.2}O_2$ (NMC532), and polyacrylic acid (PAA, Sigma-Aldrich) and polyvinylidene fluoride (PVDF, HSV900, MTI Co., molecular weight of 600,000). The slurry preparation process starts with the dissolution of either binder in NMP (N-methylpyrrolidone, Sigma Aldrich) and subsequent mixing of CB and one of the NMC powders using a magnetic stirrer. The slurry is then coated onto aluminum foil using a doctor blade. To remove residual moisture,

the electrode is dried in a vacuum oven at 80 C overnight. The composition of each electrode is given in Table 5.2.

Table 5.1. : Sample composition and surface preparation procedure.

Name	Composition	Surface preparation
532-PVDF-PC	90:5:5wt% NMC532/PVDF/CB	Ion polish
811-PAA-PC	84:8:8wt% NMC811/PAA/CB	Manual polish
532-PVDF-DEC	90:5:5wt% NMC532/PVDF/CB	Ion polish

We polish the electrodes to enable optical imaging of the particles. Sample 811-PAA-PC was manually polished (Ecomet polisher, Buehler) with 0.05 μm colloidal silica on an imperial cloth (LECO Co.) with isopropyl alcohol as a lubricant. Samples 532-PVDF-PC and 532-PVDF-ECDEC were both ion-polished (JEOL IB-19500CP). After the polishing process, the electrodes are again placed inside a vacuum oven at 80 C overnight.

5.2.2 Operando optical microscopy

We use two types of fluid cells with lithium metal as the negative electrode for the operando optical microscopy experiments: an open cell design (introduced in Section 2), and a new, closed cell design. The open cell (tested inside the glovebox) is only compatible with non-volatile electrolytes. We prepare a 0.75M $LiPF_6$ in 50:50 propylene carbonate (PC)/ethylene carbonate (EC) electrolyte for this cell. The addition of EC to PC decreases the viscosity while maintaining its non-volatility [38].

For this work, we develop a new closed cell design. This cell enables the use of linear carbonate-based electrolytes, which have better fluidity [166]. The assembly of the closed cell happens inside the glovebox using a 1M $LiPF_6$ in 50:50 diethyl carbonate (DEC)/ethylene carbonate (EC) electrolyte (Sigma Aldrich). Figure 5.1

shows the (a) top view, (b) cross-sectional view and (c) perspective view of the design. A pressure contact (via spring) connects the NMC working electrode (WE) and Li metal counter electrode (CE) to the external circuit via two screws.

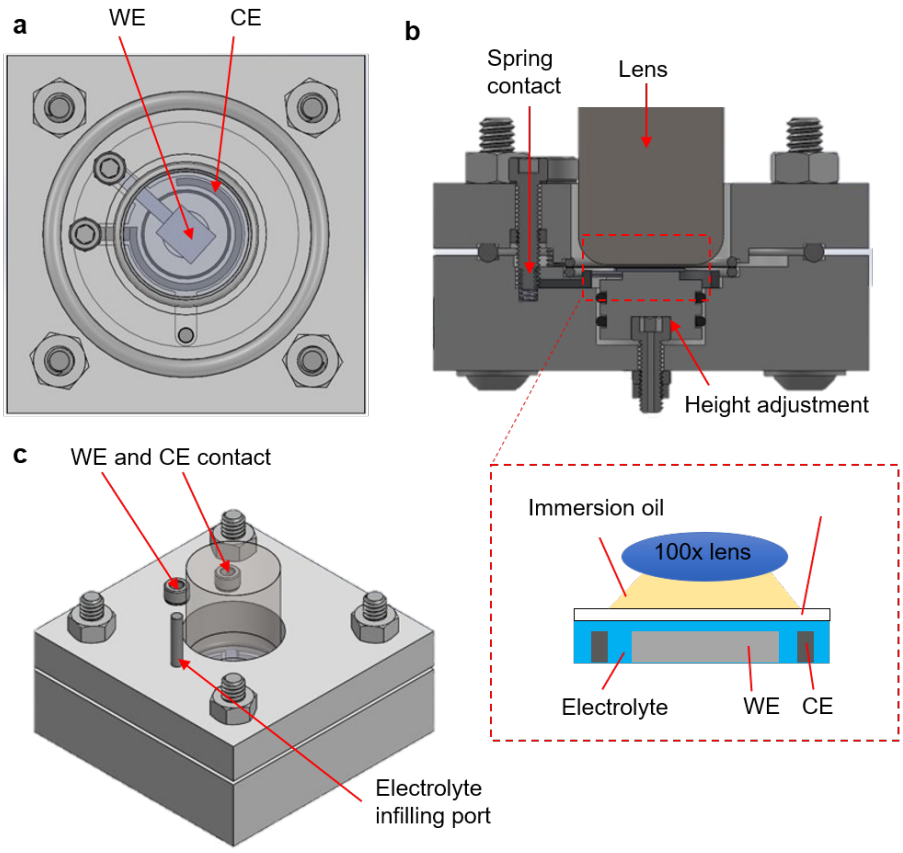

Figure 5.1. : New closed cell design for operando optical microscopy.

We use Li metal to test the sealing effectiveness of the closed cell, Figure 5.2. When exposed to air, Li metal will turn black in minutes, Figures 5.2 (a) and (b). In comparison, Li metal maintains its original shine up to 3 days inside the cell, Figures 5.2 (c) and (d).

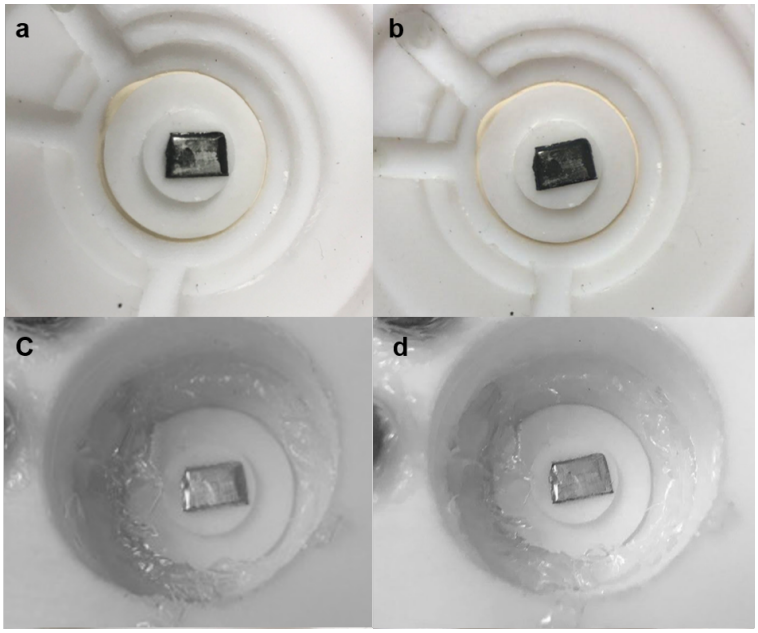

Figure 5.2. : Closed cell seal test. Photos of a Li metal ribbon after (a) 9 min and (b) 16 min of air exposure, and inside the empty (sealed) cell after (c) 16 hours and (d) 3 days outside the glovebox.

The cells are cycled at constant C-rates, followed by a hold period at the voltage cutoff, using an electrochemical station (Princeton VersaSTAT3). Table 5.2 summarizes the test configurations.

Table 5.2. : Test configuration.

Name	Electrolyte	Cell type	C-rate
532-PVDF-PC	0.75M $LiPF_6$ in PC:EC	Open cell	C/20
811-PAA-PC	0.75M $LiPF_6$ in PC:EC	Open cell	C/20
532-PVDF-DEC	1M $LiPF_6$ in EC:DEC	Closed cell	C/10

5.3 Results

This study presents an initial, qualitative assessment of the Li compositional spatiodynamics in NMC electrodes via operando optical microscopy. At high magnification, optical microscopy requires the specimen to have a smooth and flat surface in order to achieve high contrast and sharpness. Figure 5.3 compares the topography of the (a) as-fabricated and (c) manually polished NMC811/PAA/CB electrode, and (b) the ion-polished NMC532/PVDF/CB electrode. While ion-polishing preserves microscopic features of the conductive matrix intact, manual polish densifies the superficial layer of the electrode.

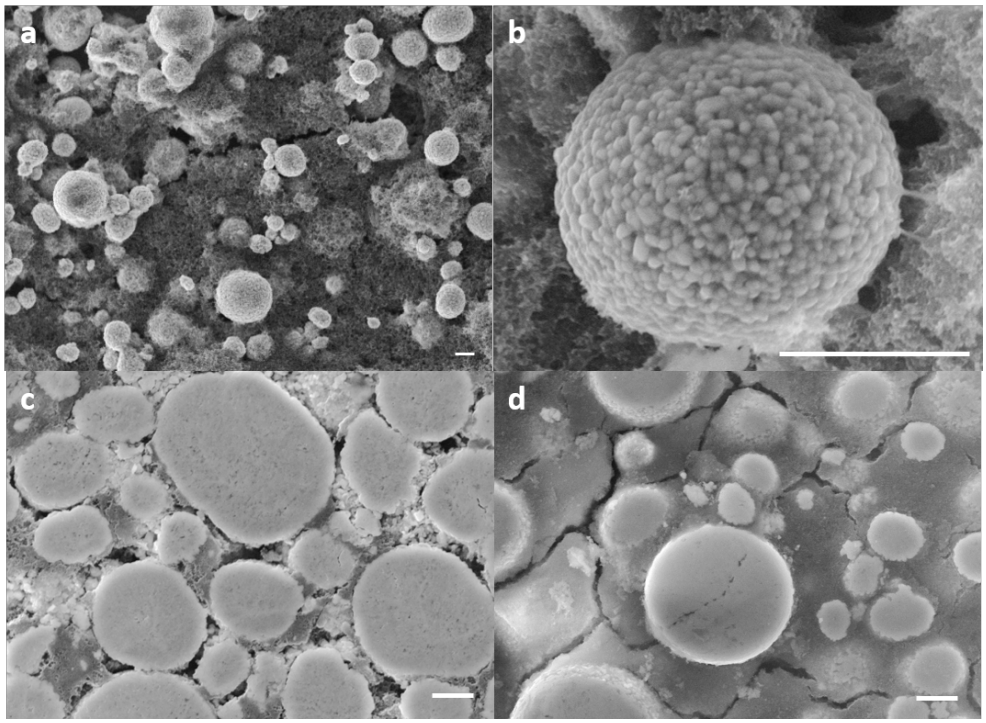

Figure 5.3. : Electrode topography before and after polishing. SEM images of samples (a,b) 811-PAA-PC as-fabricated, (c) 532-PVDF-PC post ion polish, and (d) 811-PAA-PC post manual polish. The scale bar measures 5 μm.

Figures 5.4 (a-g) shows the optical images of the top view of a pristine NMC532 electrode cycled in the PC-based electrolyte over the course of its first delithiation

(532-PVDF-PC in Table 5.2). The microscope light intensity is maintained constant throughout the test, while the focus has to be adjusted sporadically due to the change in volume of the electrode upon reactions and, consequently. The corresponding state-of-charge (SOC) of each image is indicated in the voltage curve. Comparing the pristine state (a) to the fully charged state (g), it can be inferred that there is a relation between Li composition and brightness, with brighter indicating higher local state-of-charge (i.e., lower Li concentration). Surprisingly, the composition does not change gradually and homogeneously as it would be expected for solid-solution electrodes undergoing slow charging (C/20). Instead, individual particles are "activated" seemingly randomly and asynchronously across the electrode (a-g). Interestingly, we observe the expected, synchronous charging of the particles in the subsequent discharge and charge sequences, Figures 5.5) and 5.6. Looking at the homogeneous and gradual change in brightness as a function of SOC from (a) to (b) in Figure 5.5, and throughout the second cycle (Figure 5.5, charging from (a) to (c) and discharging (d) to (g)), it can be concluded that the brightness of NMC materials is a monotonic, smooth function of the local state-of-charge, being inversely proportional to the Li concentration.

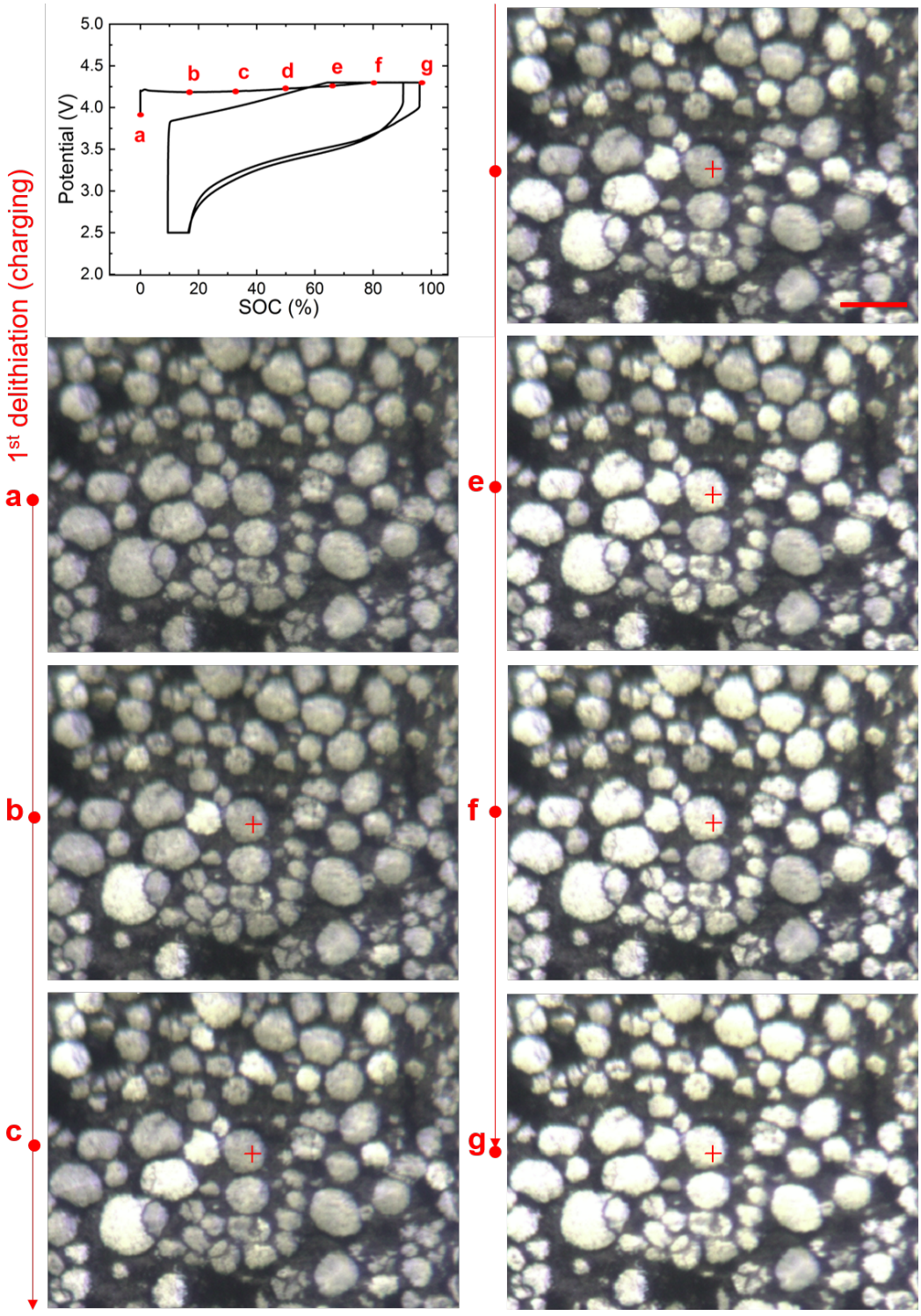

Figure 5.4. : Voltage curve and optical images of the first delithiation of NMC 532. The particles are brighter in the delithiated state (g) than in the pristine state (a). Particles change brightness suddenly and asynchronously. The red scale bar measures 20 μm.

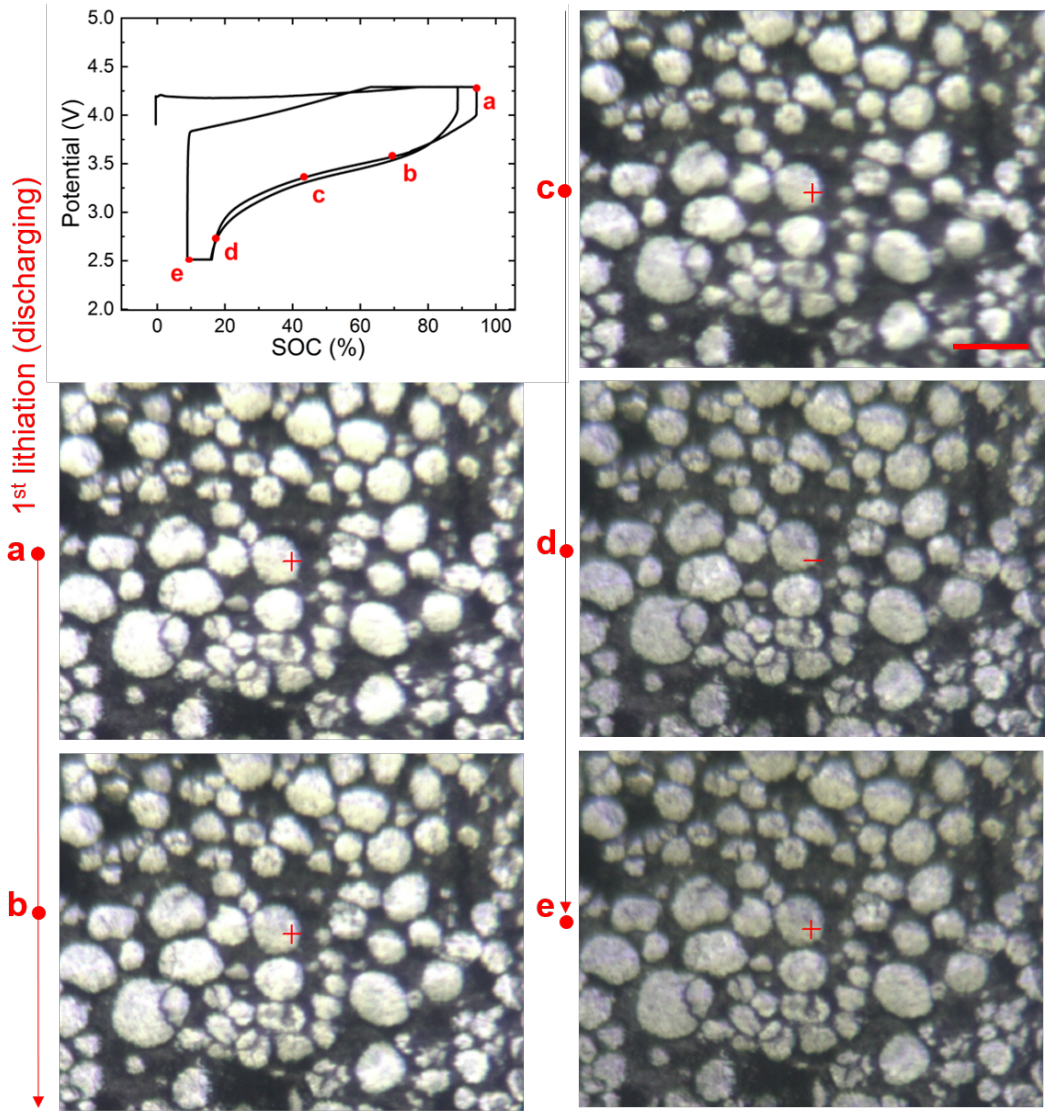

Figure 5.5. : Voltage curve and optical images of the first lithiation of NMC 532. Brightness reverses back gradually and simultaneously across all particles. The red scale bar measures 20 μm.

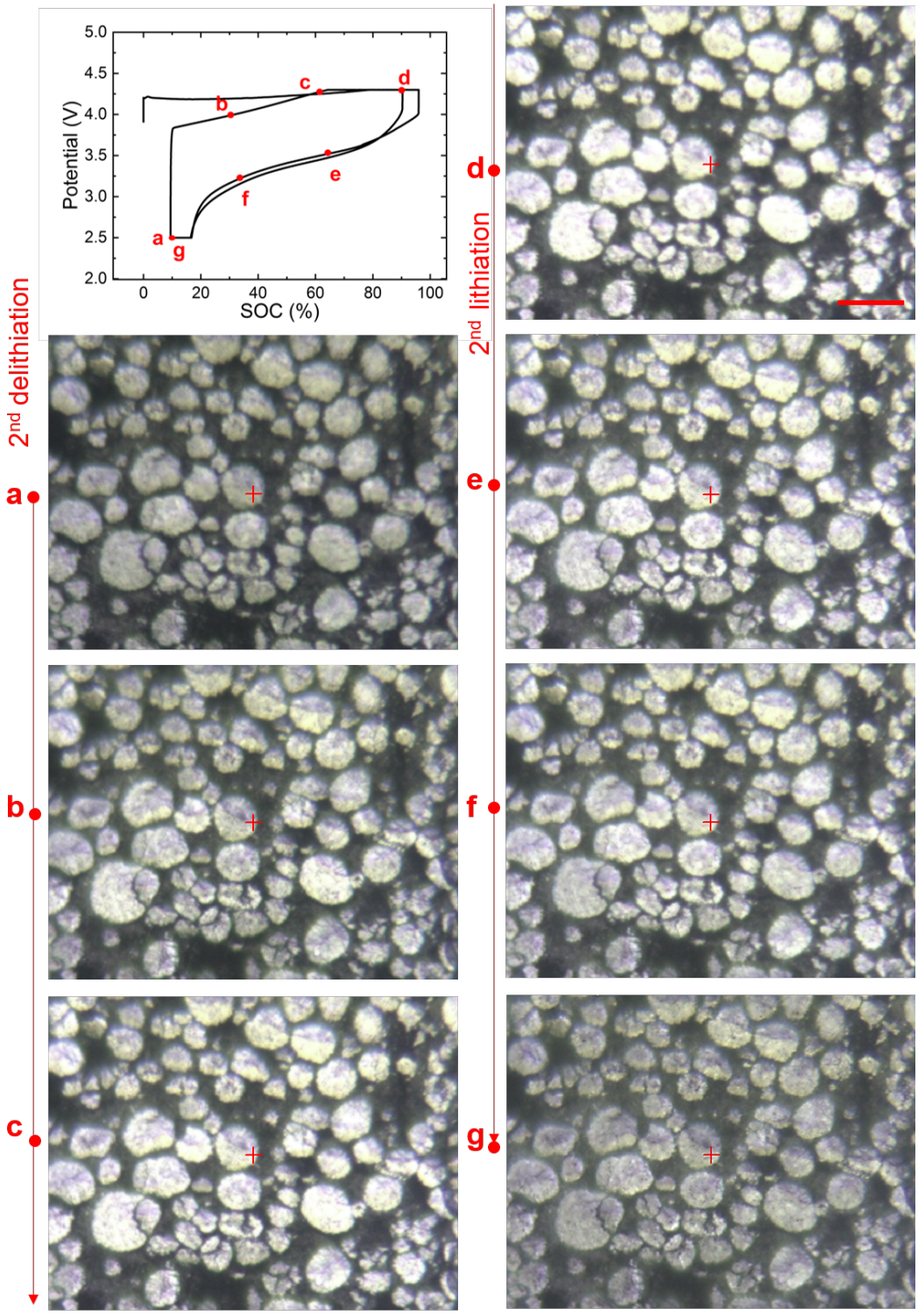

Figure 5.6. : Voltage curve and optical images of the second cycle of NMC 532. The brightness of the particles changes gradually and homogeneously.

Previous results showed that within the field of view of the optical microscope ($< 100\ \mu m$), the order in which pristine particles react during the first delithiation appears random. Figure 5.7 shows that this is also true on the electrode length scale. That is, different regions of the electrode (> 1 mm apart) exhibit the same random behavior and there is no obvious directionality in the composition dynamics.

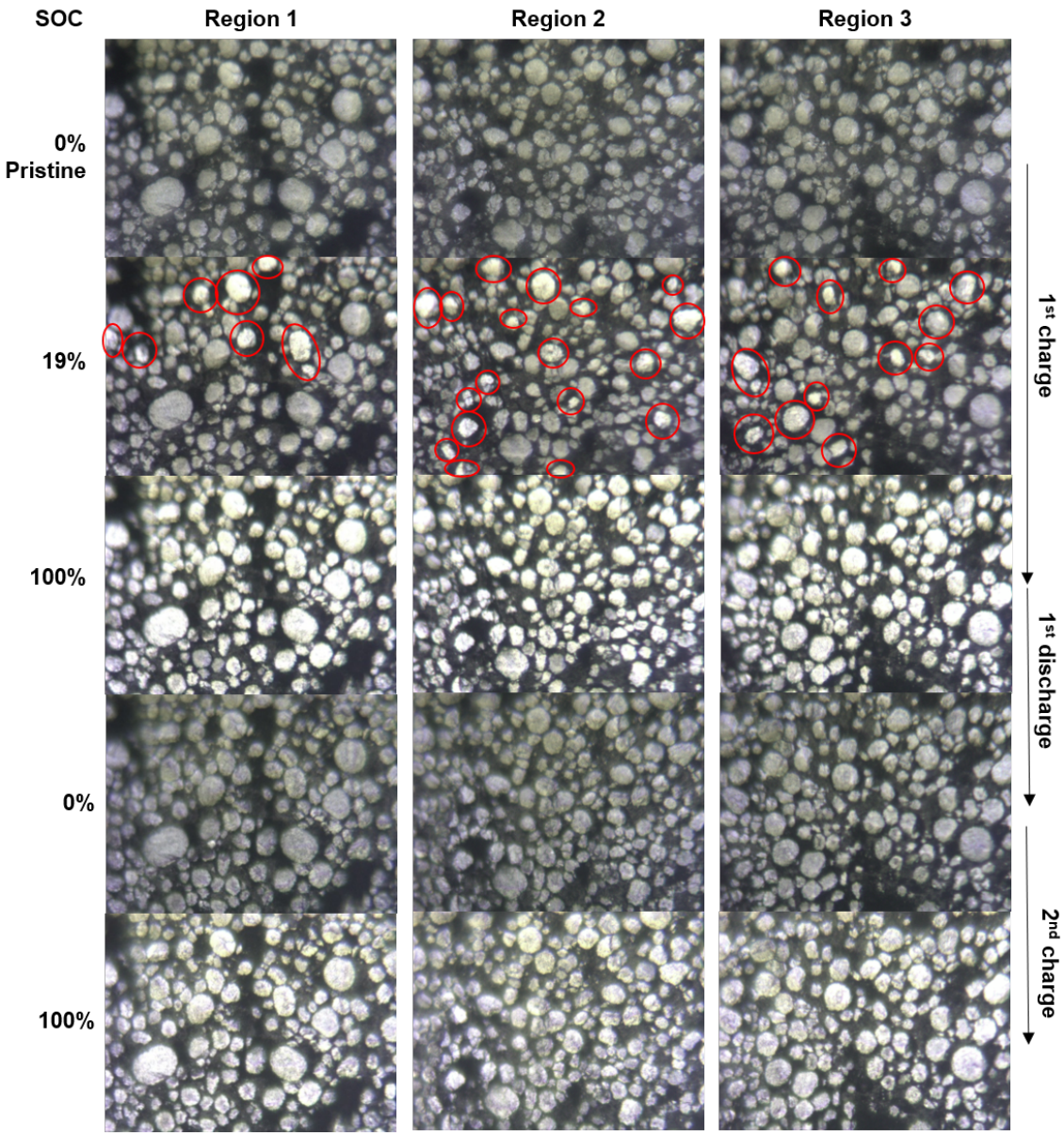

Figure 5.7. : Generality of (dis)charge kinetics across different regions of the same sample. Asynchronous first charge dynamics versus synchronous subsequent (dis)charge dynamics.

Based on the local SOC inference from the brightness, we look closer into the delithiation dynamics of pristine versus cycled NMC. Figure 5.8 top, middle, and bottom panels, show the NMC delithiation dynamics in the first, second, and third

cycles, respectively. Looking at first cycle delithiation dynamics, the optical images in the top panel shows the (a) pristine and (e) fully charged states, and (b-c) the evolution from 20% to 40% cell SOC. Note that here we refer to the fully charged and fully discharged states refer to the states after the constant potential hold of 4.3 V and 2.5 V, respectively. The electrode contains particles with pre-existing cracks (that is, the fracture is originally present in the pristine state). In the first charge of the pristine the electrode, NMC delithiation initiates at seemingly random locations within the secondary particle and across the electrode. From (b) to (c), the reaction initiates on the right-hand side of a cracked particle, and it propagates to the surrounding (connected) region of the particle (c-d). Then, delithiation initiates on the left-hand side as well (h) until eventually the entire surface of the particle appears fully charge (f). Looking now at the large cracked particle on the lower side of the image, one can see that, even though its left-hand side is already fully charged at (b), the right-hand side only reacts much later at (g). In the following cycles (middle panel and bottom panel), Li deintercalates from all surfaces approximately at the same time.

Another observation from Figure 5.8 is that the end of charge overall brightness appears to dim down over cycles (e,l,p). This is likely a result of the increase in the density of micro-cracks due to the anisotropic expansion of the primary particles that compose the secondary particles. This structural disintegration of the secondary particles has been verified previously [167].

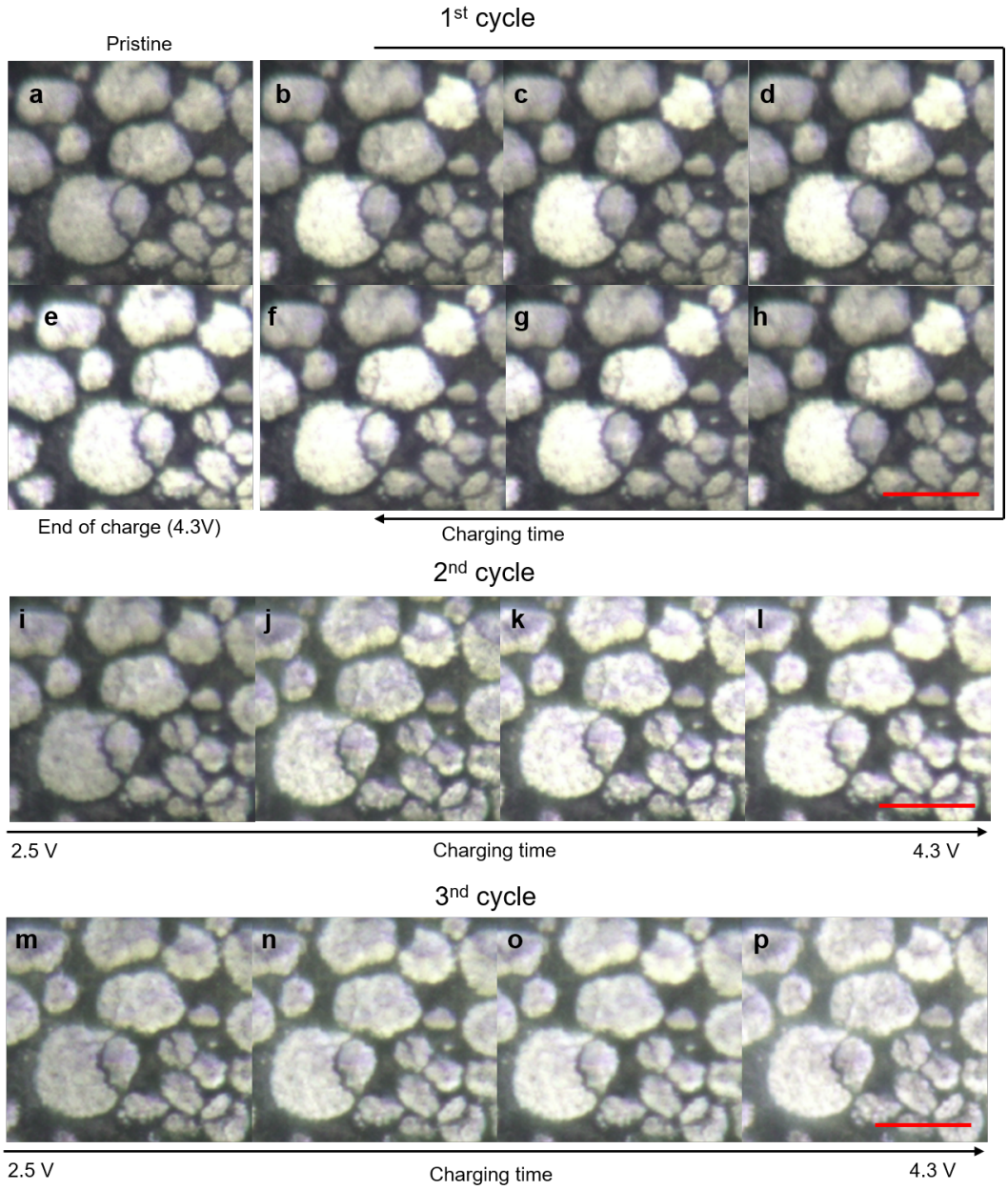

Figure 5.8. : Comparison between the delithiation kinetics in the (a) first, (b) second and (c) third cycles. In the first cycle, reaction starts locally and propagates across the connected regions the secondary particles. In the following cycles, particles charge gradually and simultaneously. The red scale bar measures 20 μm.

With the goal of better understanding the source of the aforementioned behaviors, measurements are repeated for cells with distinct compositions of transition metals (NMC 811 versus NMC 532), binders (PAA versus PVDF), and electrolyte solvent (EC/PC versus EC/DEC). These cell configurations are summarized in Tables 5.1 and 5.2.

Figure 5.9 shows that NMC811 (NMC811-PAA-PC in Table 5.2) also exhibit heterogeneous composition dynamics during the first delithiation. Particle cracking upon delithiation is more obvious in this case. For a cell SOC of $\sim$25 %, a large crack appears in the particle indicated by the red circle once it is "activated", Figure 5.9 (a) and (b). After deep delithiation (cutoff potential of 4.8 V), all particles in Figure 5.9 (c) have reacted and extensive cracking is observed throughout the electrode. Different factors may be linked with the more obvious cracking of particles in this test (NMC811-PAA-PC) as compared to the previous results in Figure 5.4 (NMC532-PVDF-PC). For instance, the extensive cracking at the end-of-charge is due to the higher cutoff voltage (4.8 V). Still, large cracks are observed even at earlier stages of the charging (Figure 5.9 (b)). This could be related to the use of the stiff PAA binder with NMC 811, compared to the soft PVDF binder with NMC 532 [94]. NMC 811 may experience larger stresses due to the matrix constraint in a stiffer binder. It would be interesting to use operando optical microscopy to study the role of the binder in the mechanical degradation of the active particles in future studies.

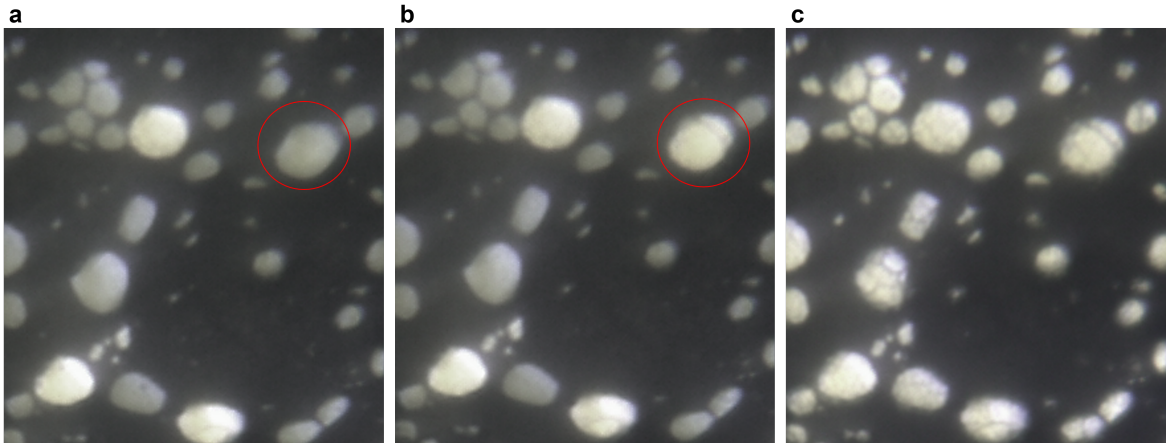

Figure 5.9. : Optical images of the first lithiation of a pristine NMC 811 electrode.

Figure 5.10 shows the optical images of the first charge of NMC 532 in a DEC-based electrolyte (532-PVDF-DEC in Table 5.2. Although the brightness contrast between charged and discharged states is not as obvious in these images compared to the previous tests (probably due to the lower settings of microscope light intensity used in this test), qualitatively, the overall kinetic behavior is consistent with previous observations using PC-based electrolyte. Figures 5.10 (a) and (b) show the pristine and partially charged states. Three particles (1, 2, 3) react first. Panel (c) shows that the evolution of the delithiation for each particle is distinct. For instance, for particle 1 (top row), the delithiation initiates at the center and propagates outwards, while for particle 3 (bottom row), it appears to initiate at the outer edge and propagates inwards.

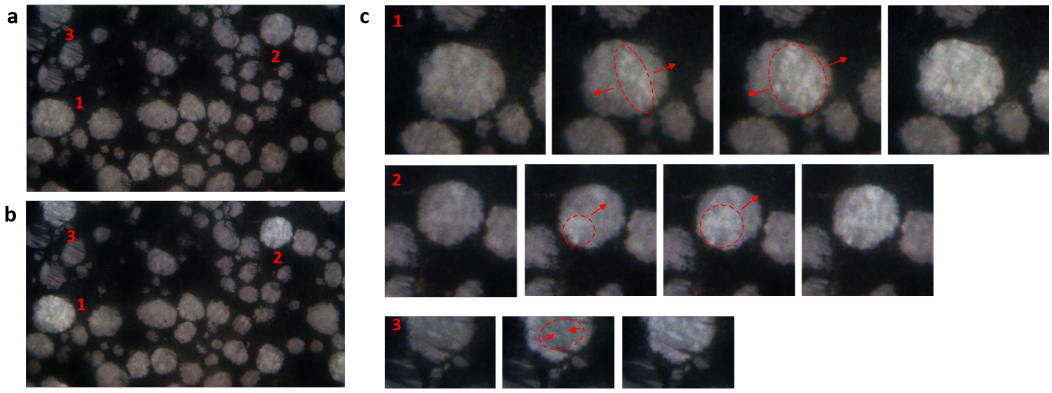

Figure 5.10. : Optical images of polished surface of a pristine NMC 811 in EC-DEC electrolyte during its first delithiation at a C-rate of C/20.

Overall, our experiments show that NMC electrodes prepared using different combinations of electrolytes, transition metals, and binders show the same unusual heterogeneous composition dynamics in its first delithiation. This is followed by a transition to normal solid-solution behavior in subsequent cycles. These observations are not fully understood yet. The most likely hypothesis is that the Li transfer resistance across the interface between NMC and the electrolyte is originally higher, and decreases after the first delithiation, such that the following Li insertion and extraction is fast. This transition could be associated with cathode-electrolyte interface (CEI) layer formation, or due to a modification of the NMC surface chemistry.

Another possibility is that such behavior is instead a consequence of extreme changes in the bulk properties of NMC. Experiments and theoretical models have shown that the diffusivity of Li in NMC in its pristine state (high Li concentration) is orders of magnitude higher than in the charged state (low Li concentration) [149, 175]. The low diffusivity of pristine NMC would hinder Li flux within the particle. This results in a drainage of the Li concentration at the surface, implicating a sudden change in brightness. The heterogeneity could come from the randomness of the primary particle orientations or some other heterogeneous aspect of the electrode microstructure. The difference between first and subsequent charging behaviors may

be associated with the capacity loss in the first cycle due to kinetic limitations [188, 66]. That is, the vacancies introduced during the first charge remain on the following cycles, leading to fast kinetics and homogeneous composition dynamics.

Complementary designed experiments and simulations are needed to uncover the mechanism behind this heterogeneous charging of pristine NMC electrodes, and its transition to a solid-solution behavior in the following cycles.

5.4 Conclusion

This works sets forth operando optical imaging to study the composition spatiodynamics of NMC electrodes. The experiments reveal that the first delithiation of pristine NMC is fundamentally different from the following (de)lithiation cycles. The first delithiation happens through localized, sudden changes of concentration and propagates through the connected regions of the active particles. At the electrode level, the first delithiation is highly heterogeneous. The following (dis)charge sequences, at the same C-rate, take the expected route and proceed through a gradual and simultaneous (de)lithiation of all viable particles. Tests using three distinct cell configurations showed that this first charge heterogeneity ensues for different compositions of the electrolyte, conductive matrix, and transition metal. Such behavior could be associated with the Li diffusivity dependency on the Li concentration in combination with the first cycle capacity loss. Another hypothesis is that this behavior is a result of some process happening at the interface between the NMC and electrolyte, which changes the charge transfer resistance upon the first reaction. This change could be related to the CEI layer formation mechanism, or a modification of the NMC surface chemistry. The results presented herein calls for further investigation on the first cycle composition dynamics of NMC materials to uncover the underlying mechanism behind the observed heterogeneity and determine its implications on the battery performance.

6. CONCLUSIONS AND OUTLOOK

This thesis investigated the chemo-mechanics of energy materials through small-scale, operando/in-situ experiments. Chapter 2 introduced a new operando indentation platform to characterize mechanical properties of active materials as a function of state-of-charge under controlled electrochemical operation. Chapter 3 presented a nanoindentation approach that enables probing spatiotemporal Li profile of electrodes during Li reactions through knowledge of the functional relationship between mechanical properties and Li composition. This work extends on the current understanding of stress-regulated diffusion and the need to account for solution non-ideality. The measurements, along with multiphysics finite element modeling, explain the long-debated lithiation kinetics of amorphous silicon, and the mechanisms behind the asymmetric charge versus discharge rate-capability, and Li trapping behavior. Chapter 4 addressed the influence of the electrolyte solution on the mechanical properties of the individual material phases in composite electrodes. Lastly, Chapter 5 exposed a previously unknown kinetic behavior of pristine NMC materials upon the first Li extraction via operando optical microscopy. Overall, the findings and experimental tools developed in this thesis will help generate insights about important processes regulating the performance and lifetime of electrochemical devices.

The contributions of this dissertation give rise to new research questions and opportunities to study chemomechanical processes in electrochemical devices, which are summarized below.

- This thesis showed that the composition dependency of the Li diffusivity results in an asymmetric charging-rate capability during lithiation versus delithiation. This characteristic has negative implications on the mechanical stability and capacity retention over cycles. A systematic analysis of this effect pairing experiments and modeling will help diagnose and treat kinetic limitations. Possible

solutions include the use of customized charging protocols and the doping of active materials.

- The pathways connecting the structural stability and electrochemical performance of batteries are complex. From the design perspective, it is essential to understand the role and cascading effect of structural instabilities in order to prioritize issues. From the operation perspective, understanding the exact, quantitative impact of mechanical degradation on the performance of batteries enables diagnostic, and taking preventive measures to protect the system from deteriorating or undergoing sudden failure. It is necessary to further the field of diagnostics with an appropriate operando understanding of fracture mechanics and degradation mechanisms.

- One interesting observation in the intermittent galvanostatic experiments in Chapter 2 was the jump in the rate of expansion immediately after the application of a fixed current (referred in this work as an electrochemical shock). This jump is unexpected and not currently understood. Literature reports on the effect of pulsed current charging on the battery performance have been somewhat contradictory, which is likely due to an incomplete understanding of the mechanisms behind the observations. The electrochemical shock observed in our experiments could be associated with the negative impact of the pulsed charging by generating larger mechanical degradation and performance deterioration. It would be valuable to understand the mechanism behind this phenomenon and its role on the battery performance.

- In Chapter 2, we found that the creep exponent of pure Si drops dramatically during the initial Li insertion and rapidly reaches a roughly constant value, behaving similarly to a step function. In addition, at the composition of roughly Li3Si, there is a slight increase in the stress exponent. From a fundamental perspective, it would be interesting to develop a mechanistic understanding of

how the Li concentration regulates the time-dependent deformation of relevant materials.

- Solid-state batteries have the potential to be safer than traditional Li-ion batteries and provide higher energy and power density, yet they suffer from added mechanical problems, which have so far prevented its commercialization. The two main issues to be overcome are the mechanical failure between the electrode and the solid electrolyte, and the concurrent cracking and Li dendrite growth through the bulk of the electrolyte. The former issue leads to a high impedance at the interface, and the latter leads to the short-circuiting of the battery. Although not being a practical solution for real applications, the most successful realizations of solid-state batteries to date have been achieved through the use of external pressure, which highlights the significance of the mechanical instabilities on the performance. There is a need for tools to study the interfacial processes in solid-state batteries through small-scale operando experiments and measure meaningful properties dictating their mechanical stability. This knowledge can be applied the design of systems of improve the chemo-mechanical reliability.

REFERENCES

REFERENCES

[1] S. B. Adler. Chemical expansivity of electrochemical ceramics. *Journal of the American Ceramic Society*, 84(9):2117–2119, 2001.

[2] G. Anstis, P. Chantikul, B. R. Lawn, and D. Marshall. A critical evaluation of indentation techniques for measuring fracture toughness: I, direct crack measurements. *Journal of the American Ceramic Society*, 64(9):533–538, 1981.

[3] N. Balke, S. Jesse, A. N. Morozovska, E. Eliseev, D. W. Chung, Y. Kim, L. Adamczyk, R. E. García, N. Dudney, and S. V. Kalinin. Nanoscale mapping of ion diffusion in a lithium-ion battery cathode. *Nature Nanotechnology*, 5(10):749–754, 2010.

[4] R. W. Balluffi, S. M. Allen, and W. C. Carter. *Kinetics of materials*. John Wiley & Sons, 2005.

[5] M. Z. Bazant. Theory of chemical kinetics and charge transfer based on nonequilibrium thermodynamics. *Accounts of Chemical Research*, 46(5):1144–1160, 5 2013.

[6] L. Y. Beaulieu, K. W. Eberman, R. L. Turner, L. J. Krause, and J. R. Dahna. Colossal reversible volume changes in lithium alloys. *Electrochemical and Solid-State Letters*, 4(9):A137, 9 2001.

[7] L. Y. Beaulieu, T. D. Hatchard, A. Bonakdarpour, M. D. Fleischauer, and J. R. Dahn. Reaction of Li with alloy thin films studied by in situ AFM. *Journal of The Electrochemical Society*, 150(11):A1457, 2003.

[8] L. A. Berla, S. W. Lee, Y. Cui, and W. D. Nix. Mechanical behavior of electrochemically lithiated silicon. *Journal of Power Sources*, 273:41–51, 2015.

[9] S. T. Boles, A. Sedlmayr, O. Kraft, and R. Mönig. In situ cycling and mechanical testing of silicon nanowire anodes for lithium-ion battery applications. *Applied Physics Letters*, 100(24):243901, 2012.

[10] L. Boltzmann. Zur Integration der Diffusionsgleichung bei variabeln Diffusionscoefficienten. *Annalen der Physik*, 289(13):959–964, 1 1894.

[11] A. Bordes, E. De Vito, D. Haon, C. Secouard, A. Montani, and P. Marcus. Investigation of lithium insertion mechanisms of a thin-film Si electrode by coupling time-of-flight secondary-ion mass spectrometry, X-ray photoelectron spectroscopy, and focused-ion-beam/SEM. *ACS applied materials & interfaces*, 7:27853–27862, 2015.

[12] A. Bower, N. A. Fleck, A. Needleman, and N. Ogbonna. Indentation of a power law creeping solid. *Proc. R. Soc. Lond. A*, 441(1911):97–124, 1993.

[13] A. F. Bower, E. Chason, P. R. Guduru, and B. W. Sheldon. A continuum model of deformation, transport and irreversible changes in atomic structure in amorphous lithium-silicon electrodes. *Acta Materialia*, 98:229–241, 2015.

[14] L. Brassart and Z. Suo. Reactive flow in solids. *Journal of the Mechanics and Physics of Solids*, 61(1):61–77, 2013.

[15] G. Bucci, S. P. Nadimpalli, V. A. Sethuraman, A. F. Bower, and P. R. Guduru. Measurement and modeling of the mechanical and electrochemical response of amorphous Si thin film electrodes during cyclic lithiation. *Journal of the Mechanics and Physics of Solids*, 62:276–294, 1 2014.

[16] R. C. Cammarata. Generalized thermodynamics of surfaces with applications to small solid systems. *Solid State Physics*, 61:1–75, 2009.

[17] P.-F. Cao, M. Naguib, Z. Du, E. Stacy, B. Li, T. Hong, K. Xing, D. N. Voylov, J. Li, D. L. Wood III, et al. Effect of binder architecture on the performance of silicon/graphite composite anodes for lithium ion batteries. *ACS applied materials & interfaces*, 10(4):3470–3478, 2018.

[18] C. Chang, X. Li, and Z. Xu. Microstructure- and concentration-dependence of lithium diffusion in the silicon anode: Kinetic Monte Carlo simulations and complex network analysis. *Applied Physics Letters*, 113(12):121904, 9 2018.

[19] B. Chen, H. Zhang, J. Xuan, G. J. Offer, and H. Wang. Seeing is Believing: In Situ/Operando Optical Microscopy for Probing Electrochemical Energy Systems. *Advanced Materials Technologies*, 5(10):2000555, 10 2020.

[20] H. S. Chen, Y. Han, L. Yang, Y. H. Bao, J. Chen, X. Li, J. Pang, W. L. Song, and D. N. Fang. A method for analyzing two-dimensional lithium ion concentration in the nano silicon films. *Applied Physics Letters*, 115(26):264102, 2019.

[21] J. Chen, X. Fan, Q. Li, H. Yang, M. R. Khoshi, Y. Xu, S. Hwang, L. Chen, X. Ji, C. Yang, H. He, C. Wang, E. Garfunkel, D. Su, O. Borodin, and C. Wang. Electrolyte design for LiF-rich solid–electrolyte interfaces to enable high-performance microsized alloy anodes for batteries. *Nature Energy*, pages 1–12, 4 2020.

[22] Z. Chen, L. Christensen, and J. Dahn. Comparison of pvdf and pvdf-tfe-p as binders for electrode materials showing large volume changes in lithium-ion batteries. *Journal of The Electrochemical Society*, 150(8):A1073–A1078, 2003.

[23] Z. Chen, L. Christensen, and J. Dahn. Mechanical and electrical properties of poly (vinylidene fluoride–tetrafluoroethylene–propylene)/super-s carbon black swelled in liquid solvent as an electrode binder for lithium-ion batteries. *Journal of applied polymer science*, 91(5):2958–2965, 2004.

[24] V. L. Chevrier and J. R. Dahn. First principles model of amorphous silicon lithiation. *Journal of The Electrochemical Society*, 156(6):A454, 2009.

[25] S. Choi, T.-w. Kwon, A. Coskun, and J. W. Choi. Highly elastic binders integrating polyrotaxanes for silicon microparticle anodes in lithium ion batteries. *Science*, 357(6348):279–283, 2017.

[26] C. Y. Chou and G. S. Hwang. Surface effects on the structure and lithium behavior in lithiated silicon: A first principles study. *Surface Science*, 612:16–23, 2013.

[27] N. Chung, Y. Kwon, and D. Kim. Thermal, mechanical, swelling, and electrochemical properties of poly (vinylidene fluoride)-co-hexafluoropropylene/poly (ethylene glycol) hybrid-type polymer electrolytes. *Journal of power sources*, 124(1):148–154, 2003.

[28] J. Crank. *The mathematics of diffusion*. Oxford university press, 1975.

[29] A. v. Cresce, S. M. Russell, D. R. Baker, K. J. Gaskell, and K. Xu. In situ and quantitative characterization of solid electrolyte interphases. *Nano letters*, 14(3):1405–1412, 2014.

[30] E. D. Cubuk and E. Kaxiras. Theory of structural transformation in lithiated amorphous silicon. *Nano letters*, 14(7):4065–4070, 2014.

[31] Z. Cui, F. Gao, Z. Cui, and J. Qu. A second nearest-neighbor embedded atom method interatomic potential for Li–Si alloys. *Journal of Power Sources*, 207:150–159, 6 2012.

[32] L. S. de Vasconcelos, N. Sharma, R. Xu, and K. Zhao. In-situ nanoindentation measurement of local mechanical behavior of a li-ion battery cathode in liquid electrolyte. *Experimental Mechanics*, 59(3):337–347, 2019.

[33] L. S. de Vasconcelos, R. Xu, J. Li, and K. Zhao. Grid indentation analysis of mechanical properties of composite electrodes in li-ion batteries. *Extreme Mechanics Letters*, 9:495–502, 2016.

[34] L. S. de Vasconcelos, R. Xu, and K. Zhao. Operando nanoindentation: a new platform to measure the mechanical properties of electrodes during electrochemical reactions. *Journal of The Electrochemical Society*, 164(14):A3840–A3847, 2017.

[35] L. S. de Vasconcelos, R. Xu, and K. Zhao. Quantitative spatiotemporal li profiling using nanoindentation. *Journal of the Mechanics and Physics of Solids*, page 104102, 2020.

[36] C. V. Di Leo, E. Rejovitzky, and L. Anand. Diffusion-deformation theory for amorphous silicon anodes: The role of plastic deformation on electrochemical performance. *International Journal of Solids and Structures*, 67-68:283–296, 8 2015.

[37] B. Ding, H. Wu, Z. Xu, X. Li, and H. Gao. Stress effects on lithiation in silicon. *Nano Energy*, 38:486–493, 8 2017.

[38] M. S. Ding and T. R. Jow. Conductivity and Viscosity of PC-DEC and PC-EC Solutions of LiPF 6. *Journal of The Electrochemical Society*, 150:620–628, 2003.

[39] N. Ding, J. Xu, Y. X. Yao, G. Wegner, X. Fang, C. H. Chen, and I. Lieberwirth. Determination of the diffusion coefficient of lithium ions in nano-Si. *Solid State Ionics*, 180(2-3):222–225, 2009.

[40] K. Durst, M. Göken, and H. Vehoff. Finite element study for nanoindentation measurements on two-phase materials. *Journal of materials research*, 19(1):85–93, 2004.

[41] T. Ebisu and S. Horibe. Analysis of the indentation size effect in brittle materials from nanoindentation load–displacement curve. *Journal of the European Ceramic Society*, 30(12):2419–2426, 2010.

[42] M. Ebner, F. Marone, M. Stampanoni, and V. Wood. Visualization and quantification of electrochemical and mechanical degradation in li ion batteries. *Science*, 342(6159):716–720, 2013.

[43] J. Field, M. Swain, and R. Dukino. Determination of fracture toughness from the extra penetration produced by indentation-induced pop-in. *Journal of materials research*, 18(6):1412–1419, 2003.

[44] D. P. Finegan, A. Vamvakeros, L. Cao, C. Tan, T. M. M Heenan, S. R. Daemi, S. D. M Jacques, A. M. Beale, M. Di Michiel, K. Smith, D. J. L Brett, P. R. Shearing, and C. Ban. Spatially resolving lithiation in silicongraphite composite electrodes via in situ high-energy X-ray diffraction computed tomography. *Nano Lett*, 19:3820, 2019.

[45] X. Gao, W. Lu, and J. Xu. Unlocking multiphysics design guidelines on Si/C composite nanostructures for high-energy-density and robust lithium-ion battery anode. *Nano Energy*, 81:105591, 3 2021.

[46] A. Ghannoum, R. C. Norris, K. Iyer, L. Zdravkova, A. Yu, and P. Nieva. Optical characterization of commercial lithiated graphite battery electrodes and in situ fiber optic evanescent wave spectroscopy. *ACS Applied Materials and Interfaces*, 8(29):18763–18769, 2016.

[47] H. Ghassemi, M. Au, N. Chen, P. A. Heiden, and R. S. Yassar. In situ electrochemical lithiation/delithiation observation of individual amorphous Si nanorods. *ACS Nano*, 5(10):7805–7811, 2011.

[48] Y.-J. Gu, Q.-G. Zhang, Y.-B. Chen, H.-Q. Liu, J.-X. Ding, Y.-M. Wang, H.-F. Wang, L. Chen, M. Wang, S.-W. Fan, et al. Reduction of the lithium and nickel site substitution in $Li_{1+x}Ni_{0.5}Co_{0.2}Mn_{0.3}O_2$ with Li excess as a cathode electrode material for li-ion batteries. *Journal of Alloys and Compounds*, 630:316–322, 2015.

[49] D. Harding, W. Oliver, and G. Pharr. Cracking during nanoindentation and its use in the measurement of fracture toughness. *MRS Online Proceedings Library Archive*, 356, 1994.

[50] S. J. Harris, A. Timmons, D. R. Baker, and C. Monroe. Direct in situ measurements of Li transport in Li-ion battery negative electrodes. *Chemical Physics Letters*, 485(4-6):265–274, 2010.

[51] T. D. Hatchard and J. R. Dahn. In Situ XRD and Electrochemical Study of the Reaction of Lithium with Amorphous Silicon. *Journal of The Electrochemical Society*, 151(6):A838, 2004.

[52] J. Hay. Introduction to instrumented indentation testing. *Experimental techniques*, 33(6):66–72, 2009.

[53] J. Hay, P. Agee, and E. Herbert. Continuous stiffness measurement during instrumented indentation testing. *Experimental Techniques*, 34(3):86–94, 2010.

[54] J. Hay and B. Crawford. Measuring substrate-independent modulus of thin films. *Journal of Materials Research*, 26(6):727–738, 2011.

[55] J. He and S. Veprek. Finite element modeling of indentation into superhard coatings. *Surface and Coatings Technology*, 163:374–379, 2003.

[56] B. Hertzberg, J. Benson, and G. Yushin. Ex-situ depth-sensing indentation measurements of electrochemically produced si–li alloy films. *Electrochemistry Communications*, 13(8):818–821, 2011.

[57] M. Hoffmann, M. Zier, S. Oswald, and J. Eckert. Challenges for lithium species identification in complementary Auger and X-ray photoelectron spectroscopy. *Journal of Power Sources*, 288:434–440, 8 2015.

[58] G. Huajian, C. Cheng-Hsin, and L. Jin. Elastic contact versus indentation modeling of multi-layered materials. *International journal of Solids and Structures*, 29(20):2471–2492, 1992.

[59] X. Huang, H. Yang, W. Liang, M. Raju, M. Terrones, V. H. Crespi, A. C. Van Duin, and S. Zhang. Lithiation induced corrosive fracture in defective carbon nanotubes. *Applied Physics Letters*, 103(15):153901, 2013.

[60] E. Huger, L. Dorrer, and H. Schmidt. Permeation, Solubility, Diffusion and Segregation of Lithium in Amorphous Silicon Layers. *Chemistry of Materials*, 30(10):3254–3264, 2018.

[61] N. Iqbal, Y. Ali, and S. Lee. Chemo-mechanical response of composite electrode systems with multiple binder connections. *Electrochimica Acta*, 364:137312, 12 2020.

[62] N. Iqbal and S. Lee. Mechanical failure analysis of graphite anode particles with pvdf binders in li-ion batteries. *Journal of The Electrochemical Society*, 165(9):A1961–A1970, 2018.

[63] B. Jerliu, E. Huger, M. Horisberger, J. Stahn, and H. Schmidt. Irreversible lithium storage during lithiation of amorphous silicon thin film electrodes studied by in-situ neutron reflectometry. *Journal of Power Sources*, 359:415–421, 2017.

[64] P. Johari, Y. Qi, and V. B. Shenoy. The mixing mechanism during lithiation of Si negative electrode in Li-ion batteries: An Ab initio molecular dynamics study. *Nano Letters*, 11(12):5494–5500, 2011.

[65] S. Jouanneau, K. Eberman, L. Krause, and J. Dahn. Synthesis, characterization, and electrochemical behavior of improved $Li[Ni_xCo_{1-2x}Mn_x]O_2$ ($0.1 \geq x \geq 0.5$). *Journal of The Electrochemical Society*, 150(12):A1637–A1642, 2003.

[66] J. Kasnatscheew, M. Evertz, B. Streipert, R. Wagner, R. Klöpsch, B. Vortmann, H. Hahn, S. Nowak, M. Amereller, A. C. Gentschev, P. Lamp, and M. Winter. The truth about the 1st cycle Coulombic efficiency of $LiNi_{1/3}Co_{1/3}Mn_{1/3}O_2$ (NCM) cathodes. *Physical Chemistry Chemical Physics*, 18(5):3956–3965, 2016.

[67] K. Kendall, N. M. Alford, and J. D. Birchall. Elasticity of particle assemblies as a measure of the surface energy of solids. *Proc. R. Soc. Lond. A*, 412(1843):269–283, 1987.

[68] S. Khosrownejad and W. Curtin. Model for charge/discharge-rate-dependent plastic flow in amorphous battery materials. *Journal of the Mechanics and Physics of Solids*, 94:167–180, 2016.

[69] S. Kim, S. J. Choi, K. Zhao, H. Yang, G. Gobbi, S. Zhang, and J. Li. Electrochemically driven mechanical energy harvesting. *Nature communications*, 7:10146, 2016.

[70] Y.-H. Kim, S.-I. Pyun, and J.-Y. Go. An investigation of intercalation-induced stresses generated during lithium transport through sol–gel derived $Li_xMn_2O_4$ film electrode using a laser beam deflection method. *Electrochimica acta*, 51(3):441–449, 2005.

[71] S. Komaba, K. Shimomura, N. Yabuuchi, T. Ozeki, H. Yui, and K. Konno. Study on polymer binders for high-capacity sio negative electrode of li-ion batteries. *The Journal of Physical Chemistry C*, 115(27):13487–13495, 2011.

[72] S. Kugler, G. Molnár, G. Petö, E. Zsoldos, L. Rosta, A. Menelle, and R. Bellissent. Neutron-diffraction study of the structure of evaporated pure amorphous silicon. *Physical Review B*, 40(11):8030, 1989.

[73] A. Kushima, J. Y. Huang, and J. Li. Quantitative fracture strength and plasticity measurements of lithiated silicon nanowires by in situ tem tensile experiments. *ACS nano*, 6(11):9425–9432, 2012.

[74] B. Laforge, L. Levan-Jodin, R. Salot, and A. Billard. Study of germanium as electrode in thin-film battery. *Journal of The Electrochemical Society*, 155(2):A181–A188, 2008.

[75] F. Larché and J. Cahn. The interactions of composition and stress in crystalline solids. *Acta Metallurgica*, 33(3):331–357, 3 1985.

[76] F. C. Larché and J. l. Cahn. The effect of self-stress on diffusion in solids. *Acta Metallurgica*, 30(10):1835–1845, 10 1982.

[77] F. C. Larché and P. W. Voorhees. Diffusion and stresses: Basic thermodynamics. *Defect and Diffusion Forum*, 129-130:31–36, 3 1996.

[78] M.-H. Lee, Y.-J. Kang, S.-T. Myung, and Y.-K. Sun. Synthetic optimization of $Li[Ni_{1/3}Co_{1/3}Mn_{1/3}]O_2$ via co-precipitation. *Electrochimica Acta*, 50(4):939–948, 2004.

[79] V. I. Levitas and H. Attariani. Anisotropic compositional expansion and chemical potential for amorphous lithiated silicon under stress tensor. *Scientific reports*, 3:1615, 2013.

[80] D. Li, Y. Wang, J. Hu, B. Lu, Y.-T. Cheng, and J. Zhang. In situ measurement of mechanical property and stress evolution in a composite silicon electrode. *Journal of Power Sources*, 366:80–85, 2017.

[81] G. Li, Z. Zhang, Z. Huang, C. Yang, Z. Zuo, and H. Zhou. Understanding the accumulated cycle capacity fade caused by the secondary particle fracture of $LiNi_{1-x-y}Co_xMn_yO_2$ cathode for lithium ion batteries. *Journal of Solid State Electrochemistry*, 21(3):673–682, 2017.

[82] J. Li, N. J. Dudney, X. Xiao, Y. T. Cheng, C. Liang, and M. W. Verbrugge. Asymmetric rate behavior of Si anodes for lithium-ion batteries: Ultrafast delithiation versus sluggish lithiation at high current densities. *Advanced Energy Materials*, 5(6):1–6, 2015.

[83] J. Li, X. Xiao, F. Yang, M. W. Verbrugge, and Y. T. Cheng. Potentiostatic intermittent titration technique for electrodes governed by diffusion and interfacial reaction. *Journal of Physical Chemistry C*, 116(1):1472–1478, 2012.

[84] J. Y. Li, Q. Xu, G. Li, Y. X. Yin, L. J. Wan, and Y. G. Guo. Research progress regarding Si-based anode materials towards practical application in high energy density Li-ion batteries. *Materials Chemistry Frontiers*, 1(9):1691–1708, 2017.

[85] X. Li and B. Bhushan. A review of nanoindentation continuous stiffness measurement technique and its applications. *Materials characterization*, 48(1):11–36, 2002.

[86] Y. Li, F. El Gabaly, T. R. Ferguson, R. B. Smith, N. C. Bartelt, J. D. Sugar, K. R. Fenton, D. A. Cogswell, A. L. Kilcoyne, T. Tyliszczak, M. Z. Bazant, and W. C. Chueh. Current-induced transition from particle-by-particle to concurrent intercalation in phase-separating battery electrodes. *Nature Materials*, 13(12):1149–1156, 2014.

[87] Y. Li, W. Mao, Q. Zhang, K. Zhang, and F. Yang. A free volume-based viscoplastic model for amorphous silicon electrode of lithium-ion battery. *Journal of The Electrochemical Society*, 167(4):040518, 2020.

[88] J. Lim, Y. Li, D. H. Alsem, H. So, S. C. Lee, P. Bai, D. A. Cogswell, X. Liu, N. Jin, Y. S. Yu, N. J. Salmon, D. A. Shapiro, M. Z. Bazant, T. Tyliszczak, and W. C. Chueh. Origin and hysteresis of lithium compositional spatiodynamics within battery primary particles. *Science*, 353(6299):566–571, 8 2016.

[89] F. Lindgren, D. Rehnlund, R. Pan, J. Pettersson, R. Younesi, C. Xu, T. Gustafsson, K. Edström, and L. Nyholm. On the capacity losses seen for optimized nano-Si composite electrodes in Li-metal half-cells. *Advanced Energy Materials*, 9(33):1901608, 2019.

[90] Z. Liu, P. Maréchal, and R. Jérôme. Blends of poly (vinylidene fluoride) with polyamide 6: interfacial adhesion, morphology and mechanical properties. *Polymer*, 39(10):1779–1785, 1998.

[91] M. Louthan Jr, G. Caskey Jr, J. Donovan, and D. Rawl Jr. Hydrogen embrittlement of metals. *Materials Science and Engineering*, 10:357–368, 1972.

[92] J. Lubliner. *Plasticity theory*. Courier Corporation, 2008.

[93] B. Lucas and W. Oliver. Indentation power-law creep of high-purity indium. *Metallurgical and Materials Transactions A*, 30(3):601–610, 1999.

[94] A. Magasinski, B. Zdyrko, I. Kovalenko, B. Hertzberg, R. Burtovyy, C. F. Huebner, T. F. Fuller, I. Luzinov, and G. Yushin. Toward efficient binders for Li-ion battery Si-based anodes: Polyacrylic acid. *ACS Applied Materials and Interfaces*, 2(11):3004–3010, 2010.

[95] R. K. Mahendran, Hirshikesh, and S. Natarajan. Stress diffusion interactions in an elastoplastic medium in the presence of geometric discontinuity. *Mechanics of Advanced Materials and Structures*, pages 1–17, 10 2020.

[96] R. Mahmudi, R. Roumina, and B. Raeisinia. Investigation of stress exponent in the power-law creep of pb–sb alloys. *Materials Science and Engineering: A*, 382(1-2):15–22, 2004.

[97] V. Maier, B. Merle, M. Göken, and K. Durst. An improved long-term nanoindentation creep testing approach for studying the local deformation processes in nanocrystalline metals at room and elevated temperatures. *Journal of Materials Research*, 28(9):1177–1188, 2013.

[98] D. Marshall, B. Lawn, and A. Evans. Elastic/plastic indentation damage in ceramics: the lateral crack system. *Journal of the American Ceramic Society*, 65(11):561–566, 1982.

[99] Q. P. McAllister, K. E. Strawhecker, C. R. Becker, and C. A. Lundgren. In situ atomic force microscopy nanoindentation of lithiated silicon nanopillars for lithium ion batteries. *Journal of Power Sources*, 257:380–387, 2014.

[100] M. T. McDowell, S. W. Lee, J. T. Harris, B. A. Korgel, C. Wang, W. D. Nix, and Y. Cui. In situ TEM of two-phase lithiation of amorphous silicon nanospheres. *Nano Letters*, 13(2):758–764, 2013.

[101] M. T. McDowell, I. Ryu, S. W. Lee, C. Wang, W. D. Nix, and Y. Cui. Studying the kinetics of crystalline silicon nanoparticle lithiation with in situ transmission electron microscopy. *Advanced Materials*, 24(45):6034–6041, 2012.

[102] H. Mehrer. The effect of pressure on diffusion. *Defect and Diffusion Forum*, 129-130:57–76, 3 1996.

[103] J. Miao and C. V. Thompson. Kinetic study of the initial lithiation of amorphous silicon thin film anodes. *Journal of The Electrochemical Society*, 165(3):A650–A656, 2018.

[104] A. Michael, C. Y. Kwok, P. Wang, O. Kazuo, and S. Varlamov. Investigation of e-beam evaporated silicon film properties for mems applications. *Journal of Microelectromechanical Systems*, 24(6):1951–1959, 2015.

[105] D. J. Miller, C. Proff, J. Wen, D. P. Abraham, and J. Bareño. Observation of microstructural evolution in li battery cathode oxide particles by in situ electron microscopy. *Advanced Energy Materials*, 3(8):1098–1103, 2013.

[106] C. Mims. The battery boost we've been waiting for is only a few years out, 3 2018.

[107] R. D. Mindlin. Continuum and lattice theories of influence of electromechanical coupling on capacitance of thin dielectric films. *International Journal of Solids and Structures*, 5(11):1197–1208, 1969.

[108] S. Mitra, J. P. Stark, and S. R. Tatti. On the use of the Boltzmann-Matano analysis to deduce concentration-dependent diffusivity. *Journal of Physics and Chemistry of Solids*, 52(2):463–465, 1991.

[109] J. Moon, B. Lee, M. Cho, and K. Cho. Ab initio and kinetic Monte Carlo simulation study of lithiation in crystalline and amorphous silicon. *Journal of Power Sources*, 272:1010–1017, 2014.

[110] D. J. Morris, S. B. Myers, and R. F. Cook. Sharp probes of varying acuity: Instrumented indentation and fracture behavior. *Journal of Materials research*, 19(1):165–175, 2004.

[111] A. Mukhopadhyay and B. W. Sheldon. Deformation and stress in electrode materials for li-ion batteries. *Progress in Materials Science*, 63:58–116, 2014.

[112] S. P. V. Nadimpalli, V. A. Sethuraman, G. Bucci, V. Srinivasan, A. F. Bower, and P. R. Guduru. On plastic deformation and fracture in Si films during electrochemical lithiation/delithiation cycling. *Journal of The Electrochemical Society*, 160(10):A1885–A1893, 2013.

[113] S. P. V. Nadimpalli, R. Tripuraneni, and V. A. Sethuraman. Real-time stress measurements in germanium thin film electrodes during electrochemical lithiation/delithiation cycling. *Journal of The Electrochemical Society*, 162(14):A2840–A2846, 2015.

[114] C. C. Nguyen, T. Yoon, D. M. Seo, P. Guduru, and B. L. Lucht. Systematic investigation of binders for silicon anodes: interactions of binder with silicon particles and electrolytes and effects of binders on solid electrolyte interphase formation. *ACS applied materials & interfaces*, 8(19):12211–12220, 2016.

[115] N. Nitta, F. Wu, J. T. Lee, and G. Yushin. Li-ion battery materials: present and future. *Materials today*, 18(5):252–264, 2015.

[116] M. Okugawa and H. Numakura. Discussion of "On the Boltzmann–Matano analysis of diffusion in a semi-infinite medium". *Metallurgical and Materials Transactions A: Physical Metallurgy and Materials Science*, 46(9):3813–3814, 9 2015.

[117] W. C. Oliver and G. M. Pharr. Measurement of hardness and elastic modulus by instrumented indentation: Advances in understanding and refinements to methodology. *Journal of materials research*, 19(1):3–20, 2004.

[118] M. R. Palacín and A. de Guibert. Why do batteries fail? *Science*, 351(6273):1253292, 2016.

[119] J. Pan, Q. Zhang, J. Li, M. J. Beck, X. Xiao, and Y.-T. Cheng. Effects of stress on lithium transport in amorphous silicon electrodes for lithium-ion batteries. *Nano Energy*, 13:192–199, 4 2015.

[120] M. Pharr, Z. Suo, and J. J. Vlassak. Measurements of the fracture energy of lithiated silicon electrodes of Li-Ion batteries. *Nano Letters*, 13(11):5570–5577, 2013.

[121] M. Pharr, Z. Suo, and J. J. Vlassak. Variation of stress with charging rate due to strain-rate sensitivity of silicon electrodes of li-ion batteries. *Journal of Power Sources*, 270:569–575, 2014.

[122] J. Philibert. Diffusion and stresses. *Defect and Diffusion Forum*, 129-130:3–8, 3 1996.

[123] P. Pietsch, M. Hess, W. Ludwig, J. Eller, and V. Wood. Combining operando synchrotron X-ray tomographic microscopy and scanning X-ray diffraction to study lithium ion batteries. *Scientific Reports*, 6(1):27994, 9 2016.

[124] D. R. Poirier and G. H. Geiger. *Transport Phenomena in Materials Processing*. Springer, 2018.

[125] S.-I. Pyun, J.-Y. Go, and T.-S. Jang. An investigation of intercalation-induced stresses generated during lithium transport through $Li_{1-\delta}CoO_2$ film electrode using a laser beam deflection method. *Electrochimica acta*, 49(25):4477–4486, 2004.

[126] M. Qu, W. H. Woodford, J. M. Maloney, W. C. Carter, Y.-M. Chiang, and K. J. Van Vliet. Nanomechanical quantification of elastic, plastic, and fracture properties of $LiCoO_2$. *Advanced Energy Materials*, 2(8):940–944, 2012.

[127] J. Quinn and G. D QUINN. Indentation brittleness of ceramics: a fresh approach. *Journal of Materials Science*, 32(16):4331–4346, 1997.

[128] E. Radvanyi, E. De Vito, W. Porcher, J. Danet, P. Desbois, J. F. Colin, and S. J. Si Larbi. Study of lithiation mechanisms in silicon electrodes by Auger Electron Spectroscopy. *Journal of Materials Chemistry A*, 1(16):4956–4965, 4 2013.

[129] D. Rehnlund, F. Lindgren, S. Böhme, T. Nordh, Y. Zou, J. Pettersson, U. Bexell, M. Boman, K. Edström, and L. Nyholm. Lithium trapping in alloy forming electrodes and current collectors for lithium based batteries. *Energy and Environmental Science*, 10(6):1350–1357, 2017.

[130] G. Reynolds, J. Fu, Y. Cheong, M. Hounslow, and A. Salman. Breakage in granulation: a review. *Chemical Engineering Science*, 60(14):3969–3992, 2005.

[131] N. Rolston, B. L. Watson, C. D. Bailie, M. D. McGehee, J. P. Bastos, R. Gehlhaar, J.-E. Kim, D. Vak, A. T. Mallajosyula, G. Gupta, et al. Mechanical integrity of solution-processed perovskite solar cells. *Extreme Mechanics Letters*, 9:353–358, 2016.

[132] H. Rumpf and H. Schubert. The behavior of agglomerates under tensile strain. *Journal of Chemical Engineering of Japan*, 7(4):294–298, 1974.

[133] T. Scholz, G. Schneider, J. Munoz-Saldana, and M. Swain. Fracture toughness from submicron derived indentation cracks. *Applied physics letters*, 84(16):3055–3057, 2004.

[134] V. A. Sethuraman, M. J. Chon, M. Shimshak, V. Srinivasan, and P. R. Guduru. In situ measurements of stress evolution in silicon thin films during electrochemical lithiation and delithiation. *Journal of Power Sources*, 195(15):5062–5066, 2010.

[135] Y. Sheng. Investigation of electrolyte wetting in lithium ion batteries: Effects of electrode pore structures and solution. *Dissertation, The University of Wisconsin-Milwaukee*, 2015.

[136] M. Simolka, C. Heim, K. A. Friedrich, and R. Hiesgen. Visualization of local ionic concentration and diffusion constants using a tailored electrochemical strain microscopy method. *Journal of The Electrochemical Society*, 166(3):A5496–A5502, 2019.

[137] E. Sivonxay, M. Aykol, and K. A. Persson. The lithiation process and Li diffusion in amorphous SiO_2 and Si from first-principles. *Electrochimica Acta*, 331:135344, 2020.

[138] B. Song, T. Sui, S. Ying, L. Li, L. Lu, and A. M. Korsunsky. Nano-structural changes in li-ion battery cathodes during cycling revealed by fib-sem serial sectioning tomography. *Journal of Materials Chemistry A*, 3(35):18171–18179, 2015.

[139] M. Stengel and N. A. Spaldin. Origin of the dielectric dead layer in nanoscale capacitors. *Nature*, 443(7112):679, 2006.

[140] C. Su, E. G. Herbert, S. Sohn, J. A. LaManna, W. C. Oliver, and G. M. Pharr. Measurement of power-law creep parameters by instrumented indentation methods. *Journal of the Mechanics and Physics of Solids*, 61(2):517–536, 2013.

[141] G. Sun, T. Sui, B. Song, H. Zheng, L. Lu, and A. M. Korsunsky. On the fragmentation of active material secondary particles in lithium ion battery cathodes induced by charge cycling. *Extreme Mechanics Letters*, 9:449–458, 2016.

[142] Y. Sun, Z. W. Seh, W. Li, H. Yao, G. Zheng, and Y. Cui. In-operando optical imaging of temporal and spatial distribution of polysulfides in lithium-sulfur batteries. *Nano Energy*, 11:579–586, 2015.

[143] N. Swaminathan, J. Qu, and Y. Sun. An electrochemomechanical theory of defects in ionic solids. i. theory. *Philosophical Magazine*, 87(11):1705–1721, 2007.

[144] D. Tabor. *The hardness of metals*. Clarendon Press, 2000.

[145] H. Takagi, M. Dao, and M. Fujiwara. Prediction of the constitutive equation for uniaxial creep of a power-law material through instrumented microindentation testing and modeling. *Materials Transactions*, 55(2):275–284, 2014.

[146] S. Tariq, K. Ammigan, P. Hurh, R. Schultz, P. Liu, and J. Shang. Li material testing - fermilab antiproton source lithium collection lens. In *Proceedings of the 2003 Particle Accelerator Conference*, volume 3, pages 1452–1454 vol.3, May 2003.

[147] R. Tripuraneni, S. Rakshit, and S. P. V. Nadimpalli. In situ measurement of the effect of stress on the chemical diffusion coefficient of Li in high-energy-density electrodes. *Journal of The Electrochemical Society*, 165(10):A2194–A2202, 7 2018.

[148] M. W. Verbrugge and B. J. Koch. Modeling lithium intercalation of single-fiber carbon microelectrodes. *Journal of The Electrochemical Society*, 143(2):600, 1996.

[149] A. Verma, K. Smith, S. Santhanagopalan, D. Abraham, K. P. Yao, and P. P. Mukherjee. Galvanostatic Intermittent Titration and Performance Based Analysis of $LiNi_{0.5}Mn_{0.3}Co_{0.2}O_2$ Cathode. *Journal of The Electrochemical Society*, 164(13):A3380–A3392, 2017.

[150] P. Verma, P. Maire, and P. Novák. A review of the features and analyses of the solid electrolyte interphase in Li-ion batteries. *Electrochimica Acta*, 55(22):6332–6341, 2010.

[151] F. Wang, J. Graetz, M. S. Moreno, C. Ma, L. Wu, V. Volkov, and Y. Zhu. Chemical distribution and bonding of lithium in intercalated graphite: Identification with optimized electron energy loss spectroscopy. *ACS Nano*, 5(2):1190–1197, 2011.

[152] J. W. Wang, Y. He, F. Fan, X. H. Liu, S. Xia, Y. Liu, C. T. Harris, H. Li, J. Y. Huang, S. X. Mao, and T. Zhu. Two-phase electrochemical lithiation in amorphous silicon. *Nano Letters*, 13(2):709–715, 2013.

[153] X. Wang, S. S. Singh, T. Ma, C. Lv, N. Chawla, and H. Jiang. Quantifying electrochemical reactions and properties of amorphous silicon in a conventional lithium-ion battery configuration. *Chemistry of Materials*, 29(14):5831–5840, 2017.

[154] Y. Wang and Y.-T. Cheng. A nanoindentation study of the viscoplastic behavior of pure lithium. *Scripta Materialia*, 130:191–195, 2017.

[155] Y. Wang, Q. Zhang, D. Li, J. Hu, J. Xu, D. Dang, X. Xiao, and Y.-T. Cheng. Mechanical property evolution of silicon composite electrodes studied by environmental nanoindentation. *Advanced Energy Materials*, 8(10):1702578, 2018.

[156] Z. Wang, Q. Su, H. Deng, and Y. Fu. Composition dependence of lithium diffusion in lithium silicide: a density functional theory study. *ChemElectroChem*, 2(9):1292–1297, 9 2015.

[157] S. Watanabe, M. Kinoshita, T. Hosokawa, K. Morigaki, and K. Nakura. Capacity fading of $LiAl_yNi_{1-x-y}Co_xO_2$ cathode for lithium-ion batteries during accelerated calendar and cycle life tests (effect of depth of discharge in charge-discharge cycling on the suppression of the micro-crack generation of $LiAl_yNi_{1-x-y}Co_xO_2$ particle). *Journal of Power Sources*, 260:50–56, 2014.

[158] C. Wendt, P. Niehoff, M. Winter, and F. M. Schappacher. Determination of the mechanical integrity of polyvinylidene difluoride in $LiNi_{1/3}Co_{1/3}Mn_{1/3}O_2$ electrodes for lithium ion batteries by use of the micro-indentation technique. *Journal of Power Sources*, 391:80–85, 2018.

[159] J. Wheeler, D. Armstrong, W. Heinz, and R. Schwaiger. High temperature nanoindentation: The state of the art and future challenges. *Current Opinion in Solid State and Materials Science*, 19(6):354–366, 2015.

[160] K. Wohl. Thermodynamic evaluation of binary and ternary liquid systems. *Transactions of the American Institute of Chemical Engineers*, 42:215–249, 1946.

[161] M. Wolf, B. M. May, and J. Cabana. Visualization of electrochemical reactions in battery materials with X-ray microscopy and mapping. *Chemistry of Materials*, 29(8):3347–3362, 2017.

[162] K. Wu, F. Wang, L. Gao, M.-R. Li, L. Xiao, L. Zhao, S. Hu, X. Wang, Z. Xu, and Q. Wu. Effect of precursor and synthesis temperature on the structural and electrochemical properties of $Li(Ni_{0.5}Co_{0.2}Mn_{0.3})O_2$. *Electrochimica Acta*, 75:393–398, 2012.

[163] Y. Wu and N. Liu. Visualizing battery reactions and processes by using in situ and in operando microscopies, 3 2018.

[164] F. Xie, H. Li, W. Zhang, and Q. Ma. A coupled model of stress, creep, and diffusion in the film/substrate system. *J. Appl. Phys*, 128:145106, 2020.

[165] J. Xie, N. Imanishi, T. Zhang, A. Hirano, Y. Takeda, and O. Yamamoto. Li-ion diffusion in amorphous Si films prepared by RF magnetron sputtering: A comparison of using liquid and polymer electrolytes. *Materials Chemistry and Physics*, 120(2-3):421–425, 2010.

[166] K. Xu. Nonaqueous Liquid Electrolytes for Lithium-Based Rechargeable Batteries Nonaqueous Liquid Electrolytes for Lithium-Based Rechargeable Batteries. *Chemical Reviews*, 104(September):4303, 2004.

[167] R. Xu, L. S. de Vasconcelos, J. Shi, J. Li, and K. Zhao. Disintegration of meatball electrodes for LiNixMnyCozO2 cathode materials. *Experimental Mechanics*, 58(4):549–559, 2018.

[168] R. Xu, L. S. de Vasconcelos, and K. Zhao. Computational analysis of chemomechanical behaviors of composite electrodes in Li-ion batteries. *Journal of Materials Research*, 31(18):2715–2727, 2016.

[169] R. Xu, H. Sun, L. S. de Vasconcelos, and K. Zhao. Mechanical and structural degradation of $LiNi_xMn_yCo_zO_2$ cathode in li-ion batteries: An experimental study. *Journal of The Electrochemical Society*, 164(13):A3333–A3341, 2017.

[170] R. Xu, Y. Yang, F. Yin, P. Liu, P. Cloetens, Y. Liu, F. Lin, and K. Zhao. Heterogeneous damage in Li-ion batteries: Experimental analysis and theoretical modeling. *Journal of the Mechanics and Physics of Solids journal homepage*, 129:160–183, 2019.

[171] R. Xu and K. Zhao. Mechanical interactions regulated kinetics and morphology of composite electrodes in Li-ion batteries. *Extreme Mechanics Letters*, 8:13–21, 2016.

[172] R. Xu and K. Zhao. Corrosive fracture of electrodes in Li-ion batteries. *Journal of the Mechanics and Physics of Solids*, 121:258–280, 12 2018.

[173] F. Z. Xuan, S. S. Shao, Z. Wang, and S. T. Tu. Coupling effects of chemical stresses and external mechanical stresses on diffusion. *Journal of Physics D: Applied Physics*, 42(1):15401, 2009.

[174] P. Yan, J. Zheng, M. Gu, J. Xiao, J.-G. Zhang, and C.-M. Wang. Intragranular cracking as a critical barrier for high-voltage usage of layer-structured cathode for lithium-ion batteries. *Nature communications*, 8:14101, 2017.

[175] S. Yang, X. Wang, X. Yang, Y. Bai, Z. Liu, H. Shu, and Q. Wei. Determination of the chemical diffusion coefficient of lithium ions in spherical Li[Ni 0.5Mn 0.3Co 0.2]O 2. *Electrochimica Acta*, 66:88–93, 4 2012.

[176] Y. Yang, R. Xu, K. Zhang, S. Lee, L. Mu, P. Liu, C. K. Waters, S. Spence, Z. Xu, C. Wei, D. J. Kautz, Q. Yuan, Y. Dong, Y. Yu, X. Xiao, H. Lee, P. Pianetta, P. Cloetens, J. Lee, K. Zhao, F. Lin, and Y. Liu. Quantification of heterogeneous degradation in Li-ion batteries. *Advanced Energy Materials*, 9(25):1900674, 7 2019.

[177] I. Yoon, D. P. Abraham, B. L. Lucht, A. F. Bower, and P. R. Guduru. In situ measurement of solid electrolyte interphase evolution on silicon anodes using atomic force microscopy. *Advanced Energy Materials*, 6(12):1600099, 2016.

[178] K. Yoshimura, J. Suzuki, K. Sekine, and T. Takamura. Measurement of the diffusion rate of Li in silicon by the use of bipolar cells. *Journal of Power Sources*, 174(2):653–657, 12 2007.

[179] W. J. Yu, C. Liu, P. X. Hou, L. Zhang, X. Y. Shan, F. Li, and H. M. Cheng. Lithiation of silicon nanoparticles confined in carbon nanotubes. *ACS Nano*, 9(5):5063–5071, 5 2015.

[180] K. Zeng and J. Zhu. Surface morphology, elastic modulus and hardness of thin film cathodes for li-ion rechargeable batteries. *Mechanics of Materials*, 91:323–332, 2015.

[181] H. W. Zhang, G. Subhash, X. N. Jing, L. J. Kecskes, and R. J. Dowding. Evaluation of hardness-yield strength relationships for bulk metallic glasses. *Philosophical Magazine Letters*, 86(5):333–345, 2006.

[182] Y. Zhang, C. Fincher, S. McProuty, and M. Pharr. In-operando imaging of polysulfide catholytes for Li–S batteries and implications for kinetics and mechanical stability. *Journal of Power Sources*, 434:226727, 9 2019.

[183] K. Zhao and Y. Cui. Understanding the role of mechanics in energy materials: a perspective. *Extreme Mechanics Letters*, 9:347–352, 2016.

[184] K. Zhao, M. Pharr, S. Cai, J. J. Vlassak, and Z. Suo. Large plastic deformation in high-capacity lithium-ion batteries caused by charge and discharge. *Journal of the American Ceramic Society*, 94(SUPPL. 1):226–235, 2011.

[185] K. Zhao, M. Pharr, J. J. Vlassak, and Z. Suoa. Inelastic hosts as electrodes for high-capacity lithium-ion batteries. *Journal of Applied Physics*, 109(1), 2011.

[186] K. Zhao, G. A. Tritsaris, M. Pharr, W. L. Wang, O. Okeke, Z. Suo, J. J. Vlassak, and E. Kaxiras. Reactive flow in silicon electrodes assisted by the insertion of lithium. *Nano Letters*, 12(8):4397–4403, 2012.

[187] J. Zheng, H. Zheng, R. Wang, L. Ben, W. Lu, L. Chen, L. Chen, and H. Li. 3d visualization of inhomogeneous multi-layered structure and young's modulus of the solid electrolyte interphase (sei) on silicon anodes for lithium ion batteries. *Physical Chemistry Chemical Physics*, 16(26):13229–13238, 2014.

[188] H. Zhou, F. Xin, B. Pei, and M. S. Whittingham. What Limits the Capacity of Layered Oxide Cathodes in Lithium Batteries?, 8 2019.

[189] B. Zhu, G. Liu, G. Lv, Y. Mu, Y. Zhao, Y. Wang, X. Li, P. Yao, Y. Deng, Y. Cui, and J. Zhu. Minimized lithium trapping by isovalent isomorphism for high initial Coulombic efficiency of silicon anodes. *Science Advances*, 5(11):eaax0651, 11 2019.